UNIVERSITÉ DE LORRAINE

NORTHEASTERN UNIVERSITYSITY

DISSERTATION

Presented at

Université de Lorraine and Northeastern University

Zongbin LI 李宗宾

To obtain the doctor's degree of

Paul-Verlaine University of Metz and Northeastern University

SPECIAL FIELD: Engineering Sciences

OPTION: Materials Science

Study on crystallographic features of Ni-Mn-Ga ferromagnetic shape memory alloys

Defended on the 9th October 2011 in front of the jury:

Y. Fautrelle	Professor	Institut National Polytechnique de Grenoble, France	Reviewer & Jury member
Z. Q. Hu	Professor Academician	Institute of Materials Research Chinese Academy of Sciences	Reviewer & Jury member
C. Esling	Professor	Paul-Verlaine University of Metz, France	Supervisor
L. Zuo	Professor	Northeastern University, China	Supervisor
Y. D. Zhang	Doctor	Paul-Verlaine University of Metz, France	Co-Supervisor
E. Beaugnon	Professor	Université Joseph Fourier, Grenoble, France	Jury member
X. Zhao	Professor	Northeastern University, China	Jury member
Z. M. Ren	Professor	Shanghai University, China	Jury member

Laboratoire d'Étude des Microstructures et de Mécanique des Matériaux, LEM3

Ile du Saulcy 57045 Metz Cedex 1

Table of contents

Abstract

Since the large magnetic-field induced strain in Ni-Mn-Ga ferromagnetic shape memory alloys was reached through the reorientation of martensite variants, the microstructural configuration and crystallographic correlation of constituent variants have strong influence on the activation of the magnetic shape memory effect. In this work, the microstructural and crystallographic features of Ni-Mn-Ga alloys were thoroughly studied.

For the 5M martensite in a $Ni_{50}Mn_{28}Ga_{22}$ alloy, the modulated superstructure information was applied for the first time to perform EBSD measurements, which enables a deeper insight into the microstructural characters. Consequently, four types of twin-related variants (A, B, C and D) were unambiguously revealed, while only two variants can be identified if using the simplified tetragonal non-modulated crystal structure for the Kikuchi pattern indexation. Based on the exact local orientations of martensite variants and crystallographic calculations, the twinning elements and the twin interface planes were fully determined. Furthermore, with no residual austenite, the most favorable orientation relationship governing martensitic transformation was revealed to be the Pitsch relation, *i.e.* $(101)_A//(1\,\bar{2}\,\bar{5})_{5M}$ and $[10\,\bar{1}]_A//[\bar{5}\,\bar{5}\,1]_{5M}$.

The auto orientation mappings on 7M martensite in a $Ni_{50}Mn_{30}Ga_{20}$ alloy were realized by using the incommensurate superstructure information, which provided an alternative means for verifying the crystal structure information. Four types of alternately distributed martensite variants (A, B, C, and D) in one martensite colony were determined to be twin-related: A and C (or B and D) possess type I twin relation, A and B (or C and D) type II twin, and A and D (or B and C) compound twin. All the twin interfaces are in coincidence with the respective twinning plane (K_1). The energetically favorable orientation relationship between the austenite and the 7M martensite was revealed to be the Pitsch relation with $(101)_A//(1\,\bar{2}\,\overline{10})_{7M}$ and $[10\,\bar{1}]_A//[\overline{10}\,\overline{10}\,1]_{7M}$. Notably, the ambiguity of the geometrically favorable orientation relationships was resolved by examining the lattice discontinuity caused by the phase transformation and the structural modulation.

In a $Ni_{54}Mn_{24}Ga_{22}$ alloy with NM martensite, four types of plates are identified locally and each plate consists of nano-scaled paired fine variants. Totally, eight orientation variants are found in one martensite colony. The paired fine variants in each plate were found to be compound twin related with the $\{112\}_{Tet}$ as the twinning plane and the $<11\,\bar{1}>_{Tet}$ the twinning direction. The inter-plate interfaces are close to $\{1\,\bar{1}\,2\}_{Tet}$ plane but with ~3° deviation, while the interfaces of two paired fine variants are in good agreement with $\{112\}_{Tet}$ twinning plane.

In a $Ni_{53}Mn_{22}Ga_{25}$ alloy with transformation temperatures around room temperature, the microstructure evolution in continuous austenite-7M-NM transformation was observed for the first time. The initially formed self-accommodated 7M martensite was characterized by a diamond-shaped morphology composed of four variants. 7M martensite was revealed to be an intermediate phase and thermodynamically metastable and it possesses an independent crystal structure rather than nanotwinned combination of NM martensite. The transformation from the 7M to the NM martensite is realized by lattice distortion following the $(001)_{7M}//(112)_{Tet}$ and $[100]_{7M}//[11\,\bar{1}]_{Tet}$ relation, which is accompanied by the thickening of the 7M plates. The role of 7M martensite in bridging the austenite to NM martensite transformation is to relieve the large lattice mismatch between austenite and NM martensite and to avoid the formation of the incoherent NM plate interfaces that represent insurmountable energy barrier.

Keywords: Ferromagnetic shape memory alloys; Ni-Mn-Ga; Microsructure; Twinning; Martensitic transformation; EBSD

Résumé

Depuis qu'une grande déformation induite par le champ magnétique dans les alliages à mémoire de forme ferromagnétiques Ni-Mn-Ga a été atteinte grâce à la réorientation des variantes de martensite, la configuration de la microstructure et la corrélation cristallographique des variantes constitutives ont une forte influence sur l'activation de l'effet de mémoire de forme magnétique. Dans ce travail, les caractéristiques microstructurales et cristallographiques des alliages Ni-Mn-Ga ont été soigneusement étudiées.

Pour la martensite 5M dans un alliage de $Ni_{50}Mn_{28}Ga_{22}$, l'information de la superstructure modulée a été appliquée pour la première fois à la réalisation de mesures EBSD, ce qui permet une compréhension plus profonde des caractères microstructuraux. En conséquence, quatre types de variantes (A, B, C et D) en relation de macle ont été clairement révélés ; en revanche, seulement deux variantes peuvent être identifiées en cas d'utilisation de la structure cristalline tétragonale simplifiée non modulée pour l'indexation des clichés de Kikuchi. Basé sur les orientations locales exactes des variantes de martensite et sur des calculs cristallographiques, les éléments de maclage et les interfaces des macles ont été entièrement déterminés. Par ailleurs, sans austénite résiduelle, la relation d'orientation la plus favorable de transformation martensitique a été révélée être la relation Pitsch, c'est-à-dire $(101)_A//(1\,\bar{2}\,\bar{5})_{5M}$ et $[10\,\bar{1}]_A//[\bar{5}\,\bar{5}\,1]_{5M}$.

Des cartes d'orientation sur la martensite 7M dans un alliage $Ni_{50}Mn_{30}Ga_{20}$ ont été réalisées automatiquement en utilisant l'information de superstructure cristalline incommensurable, qui ont fourni un moyen alternatif pour la vérification de l'information sur la structure cristalline. Quatre types de variantes de martensite (A, B, C et D) distribués alternativement dans une colonie de martensite ont été déterminés être en relation de maclage. A et C (ou B et D) est une macle de type I, A et B (ou C et D) une macle de type II, et A et D (ou B et C) une macle de type composé. Toutes les interfaces entre les variantes sont respectivement en coïncidence avec le plan de maclage (K_1). La relation d'orientation énergétiquement favorable entre l'austénite et la martensite 7M s'est révélée être la relation de Pitsch $(101)_A//(1\,\bar{2}\,\overline{10})_{7M}$ and $[10\,\bar{1}]_A//[\overline{10}\,\overline{10}\,1]_{7M}$. Notamment, l'ambiguïté de la relation d'orientation géométriquement favorable a été résolue par l'examen de la discontinuité de la maille causée par la transformation de phase et la modulation de la structure de martensite.

Dans un alliage $Ni_{54}Mn_{24}Ga_{22}$ avec la martensite non modulée (NM), quatre types de platelets sont identifiés localement et chaque platelet est constitué de variantes fines nanométriques jumelées. En tout, huit variantes d'orientation sont trouvées dans une colonie de martensite. Les variantes fines jumelées dans chaque platelet ont été trouvées être en relation de maclage composé avec $\{112\}_{Tet}$ comme plan de maclage et $<11\,\bar{1}>_{Tet}$ comme direction de maclage. Les interfaces inter- platelets sont proches de $\{1\,\bar{1}\,2\}_{Tet}$ mais avec ~ 3° de l'écart, tandis que les interfaces des deux variantes fines jumelées sont en bon accord avec le plan $\{112\}_{Tet}$, i.e. le plan de maclage.

Dans un alliage $Ni_{53}Mn_{22}Ga_{25}$ avec les températures de transformation autour de la température ambiante, l'évolution de la microstructure dans la transformation continue austénite-7M-NM a été observée pour la première fois. La martensite 7M auto-accommodée qui se forme initialement a été caractérisée par une morphologie en forme de losange composée de quatre variantes. La martensite 7M a été révélée comme étant une phase intermédiaire et thermodynamiquement métastable. La martensite 7M possède une structure cristalline indépendante plutôt que d'être la combinaison de martensite NM nanométrique en relation de macle. La transformation de la martensite 7M en celle NM est réalisée par la distorsion du réseau suite à la relation de $(001)_{7M}//(112)_{Tet}$ et $[100]_{7M}//[11\,\bar{1}]_{Tet}$, qui est accompagnée par l'épaississement des platelets de 7M. Le rôle de la martensite 7M en établissant un pont lors de la transformation martensitique de l'austénite à la martensite NM est de relaxer le grand désaccord

des mailles entre l'austénite et la martensite NM et d'éviter la formation d'interfaces incohérentes de platelets de martensite NM qui représentent une barrière énergétique infranchissable.

Mots-clés: alliages à mémoire de forme ferromagnétiques; Ni-Mn-Ga; microstructure; maclage; transformation martensitique; EBSD.

摘要

Ni-Mn-Ga 系铁磁形状记忆合金因在磁场作用下兼备输出应变大及响应速度快的特点，是近年来倍受国内外关注并竞相研发的新一代磁控形状记忆功能材料。由于Ni-Mn-Ga合金的磁感生应变通过马氏体变体的再取向实现，因而变体分布及变体间的晶体学关联强烈地影响着磁记忆效应的可获取性。在本论文的工作中，对Ni-Mn-Ga 系合金的微观组织及晶体学特征进行了深入细致的研究。

通过应用调制结构马氏体的详尽的超结构信息进行电子背散射衍射（EBSD）花样的标定，对室温下具有五层调制马氏体的$Ni_{50}Mn_{28}Ga_{22}$合金的微观组织实现了自动取向成像。结果表明在粗大的马氏体板条内部共有四种互为孪晶的马氏体变体（A, B, C, D）；若采用简化的四方结构进行标定，则只能分辨出两种变体。利用EBSD获得的正确的晶体学取向数据进行计算，确定了变体间的孪生组元及宏观界面。在不存在残余奥氏体的情况下，通过进一步的晶体学计算推导出奥氏体至五层调制马氏体转变过程最为有利的相变取向关系为Pitsch关系，既$(101)_A//(1\bar{2}\bar{5})_{5M}$和 $[10\bar{1}]_A//[\bar{5}\bar{5}1]_{5M}$。

对具有七层调制结构马氏体的$Ni_{50}Mn_{30}Ga_{20}$合金，采用了非公度的超结构信息进行EBSD自动取向成像，从而间接的验证了结构数据的正确性。结果表明，在一个马氏体变体团内部，共有4种交替分布的马氏体变体（A, B, C, D）。4种变体互为孪晶，可分为三种孪晶模式，既变体A和C（或B和D）之间具有I型孪晶关系，变体A和B（或C和D）之间具有II型孪晶关系，变体A和D（或B和C）之间具有复合孪晶关系。所有的变体间的宏观界面均与孪晶面（K_1）一致。根据实测的马氏体取向数据及晶体学计算，揭示了奥氏体与七层调制马氏体之间相变过程中最为有利的取向关系为Pitsch关系，既$(101)_A//(1\bar{2}\overline{10})_{7M}$ 和 $[10\bar{1}]_A//[\overline{10}\ \overline{10}\ 1]_{7M}$。对有利取向关系的区分充分考虑了相变过程中两相之间的晶格连续性及马氏体的结构调幅。

在具有非调制马氏体的$Ni_{54}Mn_{24}Ga_{22}$合金中，揭示了在一个变体团内部共有四种类型的粗大马氏体板条且马氏体板条内部存在成对出现的纳米尺度上的细小马氏体变体。因而，共有八种马氏体变体。同一马氏体板条内部的细小马氏体变体之间具有复合孪生关系，$\{112\}_{Tet}$为孪生面，$<11\bar{1}>_{Tet}$为孪生方向。分析了粗大马氏体板条及纳米尺度变体间的宏观界面特征。粗大马氏体板条间的宏观界面接近$\{1\bar{1}2\}_{Tet}$，约有~3°偏差，而微孪晶细小马氏体变体间的宏观界面与$\{112\}_{Tet}$孪晶面保持一致。

在马氏体转变温度在室温附近的$Ni_{53}Mn_{22}Ga_{25}$合金中，首次观察到了奥氏体-七层调制马氏体-非调制马氏体的两阶段转变的微观组织演化。七层马氏体自奥氏体内部析出过程中具有典型的自协调特征，4个互为孪晶的马氏体变体同时析出并组合成一种“金刚石”形状的变体组态，使得转变应变最小。而在七层调制马氏体至非调制马氏体的转变过程中则伴随着马氏体板条的宽化，从而使得变体间的界面数量降低，进而降低界面能。实验结果证明七层调制马氏体是一种热力学亚稳的中间相；它具有独立的晶体结构，而不应该是非调制马氏体的纳米孪生组合。在奥氏体-七层调制马氏体-非调制马氏体两阶段的转变过程中，一个奥氏体变体能够生成4个七层调制马氏体变体，而一个七层调制马氏体变体能够产生2个非调制马氏体变体，因而局部共能产生8个非调制马氏体。七层调制马氏体至非调制马氏体转变的这一过程遵循$(001)_{7M}//(112)_{Tet}$ 和 $[100]_{7M}//[11\bar{1}]_{Tet}$的取向关系，并伴随着一定的晶格畸变。七层调制马氏体这一中间产物的形成是由于奥氏体与非调制马氏体之间大的晶格畸变抑制了转变的直接进行；七层调制马氏体的出现降低了奥氏体与非调制马氏体之间的晶格畸变，使得相变得以进行，并避免了作为形核能垒的非共格界面的出现。

关键词：铁磁形状记忆合金；Ni-Mn-Ga；微观组织；孪晶；马氏体转变；电子背散射衍射

Acknowledgements

This work is financially supported by the National Natural Science Foundation of China (Grant No. 50820135101), the Ministry of Education of China (Grant Nos. 2007B35, 707017 and IRT0713), the Fundamental Research Funds for the Central Universities of China (Grant No. N090602002), the CNRS of France (PICS No. 4164) and the joint Chinese-French project OPTIMAG (N°ANR-09-BLAN-0382). I would like to give my sincere thanks to these institutions. I also gratefully acknowledge the French Embassy in Beijing for providing a grant for my study in France.

This work is completed at LEM3 (former LETAM, University of Metz, France) and the Key Laboratory for Anisotropy and Texture of Materials (Northeastern University, China). I had the honor to work with numerous colleagues in two labs and I would like to give my hearted thanks for their kind help.

I would like to sincerely thank to the reviewers, Prof. Y. Fautrelle and Prof. Z. Q. Hu, for taking time out of their busy schedules to review my dissertation and provide constructive suggestions and comments.

I would like to give my special thanks to my supervisors, Prof. Claude Esling, Dr. Yudong Zhang at University of Metz, and Prof. Liang Zuo at Northeastern University, not only for their support, ideas, guidance, and organizational help during the last three years, but also making me a better person and scientist by setting high standards and good examples.

I would also like to thank Prof. Xiang Zhao and Dr. Changshu He, for encouraging, supporting, and mentoring me during my PhD study. I would like to thank all my group members who treated me with dignity and respect.

Finally, I want to thank my parents, friends and family, especially my wife Ms. Xiaoliang Li, for their continuous support and understanding.

Chapter 1 Literature Review

1.1 General introduction

In human history, the development of science and technology has always been marked by the innovations and the evolutions in the use of materials. New advanced materials are always the stepping stones to human progress and have brought great convenience to the daily life of people. Among the numerous advanced materials, the so-called smart materials have the unique attractiveness due to their special properties to sense and respond to the environment around them in a predictable manner. They can allow their shape to be changed in different external field, like electric, magnetic or temperature field, transforming one form of energy into another. Hence, they have wide applications as actuators or sensors in various domains [1-4], such as medical, civil engineering, aerospace and marine industries. Piezoelectric ceramics, magnetostrictive materials and shape memory alloys are the main smart materials groups that have been utilized for practical applications.

Piezoelectric ceramics are the most widely used smart materials. They present two distinct abilities due to the electro-mechanical coupling [5], *i.e.* becoming electrically charged when subjected to a mechanical stress and making an expansion or contraction when voltage is applied. Piezoelectric materials have high response frequency, on the order of tens of 100 kHz, making them ideal for precise and high speed actuation. The most common piezoelectric material used in these days is lead-zirconate-titanate (PZT) [6]. Nevertheless, piezoelectric ceramics have some limitations. They tend to be brittle and the induced strain in these materials is relatively small. The best piezoelectric ceramics only exhibit a strain of about 0.19% [5].

Magnetostrictive materials such as Terfenol-D are similar to piezoelectric ceramics, but these materials respond to magnetic field rather than electric field. When a magnetic field is applied, the electron spin tries to align in the field direction

and the orbit of that electron also tends to be reoriented, which results in considerable lattice distortion, hence magnetostriction. Magnetostrictive materials can operate at high frequencies up to 10 kHz, but they also have the same drawbacks of small output strain. The leading magnetostrictive material $(Tb_{0.3}Dy_{0.7})Fe_2$, shows a field-induced strain of about 0.24%. Moreover, they are also expensive to produce and highly brittle.

Conventional shape memory alloys (SMAs) are another class of smart materials that can produce very high recoverable strains as a result of reversible martensitic transformation. The most common commercially available shape memory alloy is Ni-Ti. Ni-Ti alloys can produce strains up to 8% [2] and also can be deformed easily and biocompatible. When these shape memory alloys are cooled to martensite, the martensite phase has a multi-variant structure and, in general, almost no noticeable shape change is observed between the high-temperature and low-temperature phases owing to the small difference between the volumes of the unit cells and to the self-accommodation of martensite variants. Application of a uniaxial stress breaks this arrangement and the twin boundaries between martensite variants are activated to move. Those variants with favorable orientation with respect to the stress grow at the expense of other variants. This results in a macroscopic shape change. On heating the alloy to parent phase, the crystallographically reversible transformation causes the recovery of the original macroscopic shape. However, a major inconvenience for the practical application of the thermal-induced shape memory effect was the low working frequency (less than 1Hz) inherent to the thermal control of the effect.

Recently, a significant breakthrough in the research of shape memory alloys came about with the discovery of ferromagnetic shape memory alloys (FSMAs). The realization of large field-induced strains by the external magnetic field at high working frequencies has aroused intensive research attention to these materials [7]. So far, the reported magnetic-field-induced strain (MFIS) reached up to ~10% [8], which is an order of magnitude comparative to the conventional shape memory alloys and much higher than the strains generated in piezoelectric and magnetostrictive materials. Meanwhile, the possibility of controlling the shape change by the application of

magnetic field enables the relatively higher working frequency (KHz) than that of conventional shape memory alloys [9]. Due to these features, the ferromagnetic shape memory alloys are taken as the potential candidates for a new class of magnetic actuator materials.

The magnetic-field-induced strain effect, also termed as magnetic shape memory effect, in ferromagnetic shape memory alloys can be achieved through different mechanisms driven by external magnetic field, which includes (1) the rearrangement of ferromagnetic martensite variants by twinning and detwinning, such as Ni-Mn-Ga [10] and Fe-Pd alloys [11]; (2) the phase transition from the paramagnetic parent phase to ferromagnetic martensite, such as Fe-Mn-Ga alloys [12]; and (3) the reverse phase transition from the antiferromagnetic martensite to ferromagnetic parent phase, such as Ni(Co)-Mn-In [13] and Ni(Co)-Mn-Sn alloys [14]. Among the ferromagnetic shape memory alloys, the most significant magnetic-field-induced strain was found in Ni-Mn-Ga alloys and thus these materials have become the most attractive ones in the family of the ferromagnetic shape memory alloys. The magnetic shape memory phenomenon in Ni-Mn-Ga alloys has been demonstrated in two of the martensitic structures with the phase transformation close to the ambient temperature [8, 15].

1.2 Martensitic transformation and twin relationship between variants

Since the fundamental condition to the shape memory phenomena is the occurrence of a thermoelastic martensitic transformation, it would be useful to have a brief overview on this transformation.

Many solids undergo a solid-to-solid phase transformation. Solid state transformations are usually of two types: diffusional and displacive. Diffusional transformations take place by long range diffusion resulting from thermally activated atomic movements. The new phase is of a different chemical composition compared with that of the parent. Displacive (diffusionless) transformations, on the other hand, do not require long-range diffusion during the phase transformation. Only small atomic movements usually less than the inter-atomic distances are needed. The atoms are rearranged into a new structure in a cooperative manner, with no change of the chemical composition and their atomic arrangements.

Martensitic transformation is a kind of shear-dominant diffusionless solid-state phase transformation and occurs by nucleation and growth of the new phase from the parent phase [16]. Typically, upon cooling, the high temperature phase (austenite) with higher symmetry transforms to a low temperature phase (martensite) with lower symmetry through a first-order phase transition. There is a rigorous crystallographic connection between the lattices of the initial and final phases. The martensitic transformation is called thermoelastic, when it is thermally reversible and associated with mobile interfaces between the parent and martensitic phases with small transformation temperature hysteresis [17, 18].

In general, there are four characteristic temperatures defining the martensitic transformation process. The forward transformation start and finish temperatures from austenite to martensite are called M_s and M_f, respectively; while the inverse transformation start and finish temperatures from martensite to austenite are called A_s and A_f, respectively. Usually, the transformation temperatures differ on heating and cooling during the transformation. There is a hysteresis associated with phase

transformation. The transformation temperatures depend mainly on the alloy composition and processing history. Microstructural defects, degree of order and grain size of the parent phase can also alter the transformation temperatures by several degrees [19].

Martensitic transformation is usually accompanied by a change in the form of the transformed region which manifests itself in a characteristic relief on the surface where the martensite plate appears. Moreover, numerous physical properties show different changes with the occurrence of martensitic transformation [17]. During the transformation, a latent heat associated with the transformation is absorbed or released depending on the transformation direction. The two phases also have different resistance due to their different crystallographic structures, thus the phase transformation is associated with a change in the electrical resistivity. These changes allow for the measurement of the transformation temperatures by differential calorimetry and electrical resistivity; respectively. In addition, changes in specific volume, mechanical properties and magnetization *et al.* also allow the transformation temperatures to be determined [20, 21].

The martensite phase usually takes the form of plates and the interface separating the martensite from the parent phase is called the habit plane. A careful analysis of the surface relief reveals that any vector in the habit plane is left unrotated and undistorted during the transformation [20]. The habit plane is thus essentially "undistorted" and the shape change resulted from the martensitic transformation is an "invariant plane strain". To illustrate the transformation mechanism, in 1924, Bain proposed that the change in the structure from FCC lattice to BCC lattice could be achieved by a simple homogeneous deformation, as illustrated in Fig. 1.1 [22]. A unit cell of the BCT structure is drawn within two FCC cells. Then, the transformation to a BCC unit cell can be achieved by the compression along the z axis and the expansion along the x and y axes. This homogeneous deformation is often called the Bain distortion or Bain strain.

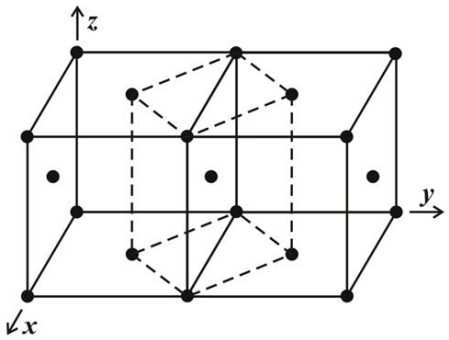

Fig. 1.1. Bain distortion (FCC to BCC) of martensite. The transformation involves the contraction of the parent phase along the *z* direction, and the expansion in *x* and *y* directions, respectively.

Although Bain distortion simply explains how the BCC unit cell can be transformed from FCC unit cells with minimum atomic movement, in fact, the Bain deformation alone would cause enormous transformation strains depending on the volume transformed and a non-invariant plane strain can be achieved. To fulfill the requirements of an invariant plane, Wechsler, Lieberman and Read [23], and Bowles and Mackenzie [24] independently developed the so called "phenomenological crystallographic theory of martensitic transformation" to explain the shape change of martensitic transformation. Although the mathematical treatment is slightly different in the two theories, they are essentially equivalent [25]. In the phenomenological theories, the shape deformation is artificially decomposed into following three components: a lattice deformation, *i.e.* Bain strain, a lattice invariant shear (slip, twinning or stacking faults), and a rigid body rotation. The pure lattice strain transforms the parent lattice into the product lattice and the combination of lattice invariant shear will, in general, leave one plane undistorted but rotated to a new position; a rigid body rotation is applied to bring back the undistorted plane into the original position. The phenomenological theories have successfully predicted crystallographic data associated with the martensitic transformation, such as the habit plane, orientation relationship, and magnitude of shape deformation *et al.*, in various alloy system, which were confirmed by experimental measurements.

Since martensitic transformation is diffusionless completed by atomic movement

in a coordinated manner, it follows that the austenite and the martensite lattices should be intimately related and lead to a reproducible orientation relationship between them. The orientation relationship can be described by specifying the parallelism between certain crystallographic planes and directions. Representative orientation relationships of martenstic transformation are given below (the subscript A represents austenite and M martensite):

Bain relation [22]: $(001)_A$ // $(001)_M$ and $[100]_A$ // $[1\,\bar{1}\,0]_M$

Kurdjumov-Sachs (K-S) relation [26]: $(111)_A$ // $(011)_M$ and $[1\,\bar{1}\,0]_A$ // $[1\,\bar{1}\,1]_M$

Nishiyama-Wassermann (N-W) relation [27, 28]: $(111)_A$ // $(011)_M$ and $[\bar{2}\,11]_A$ // $[0\,\bar{1}\,1]_M$

Greninger-Troiano (G-T) relation [29]: $(111)_A$ about 1° from $(011)_M$ and $[1\,\bar{1}\,0]_A$ about 2.5° from $[1\,\bar{1}\,1]_M$

Pitsch relation [30]: $(110)_A$ // $(1\,\bar{1}\,\bar{2})_M$ and $[1\,\bar{1}\,0]_A$ // $[\bar{1}\,1\,\bar{1}]_M$

Burgers relation (BCC to HCP) [20]: $(111)_A$ // $(0001)_M$ and $[1\,\bar{1}\,0]_A$ // $[1\,\bar{2}\,10]_M$

Orientation relationships of the two phases change from one alloy system to another, and within a given alloy system from one composition to another. Under different orientation relationships, the number of induced martensite variants is different.

As the crystal lattice of the martensite phase usually has lower symmetry than that of the parent austenite phase, elastic strains associated with the transformation accompany the nucleation and growth of the martensite. The elastic strains increase with the increasing martensite fraction. To compensate the transformation strains, different oriented variants are formed from the same parent phase. For keeping the lattice continuity, the neighboring martensite variants usually develop a twin relationship to each other. Such twins make a substantial contribution to the lattice-invariant deformation [31].

The classical definition of twinning describes that the twin and the matrix lattices are related by reflection with respect to a plane or by a rotation of 180° about an axis [32]. These two types of twin often designated as “reflection” twins and “rotation” twins. By convention [33], a twinning mode is defined by six elements: (1) K_1 - the twinning or composition plane that is the invariant (unrotated and undistorted) plane

of the simple shear; (2) η_1 - the twinning direction or the direction of shear lying in K_1; (3) K_2 - the reciprocal or conjugate twinning plane, the second undistorted but rotated plane of the simple shear; (4) η_2 - the reciprocal or conjugate twinning direction lying in K_2; (5) P - the plane of shear that is perpendicular to K_1 and K_2 and intersects K_1 and K_2 in the direction η_1 and η_2, respectively; (6) s - the magnitude of shear. The geometrical configuration of K_1, K_2, η_1, η_2 and P is shown in Fig. 1.2. According to the rationality of the Miller indices for K_1, K_2, η_1 and η_2, crystal twins are usually classified into three categories: type I twin (K_1 and η_2 are rational), type II twin (K_2 and η_1 are rational), and compound twin (K_1, K_2, η_1 and η_2 are all rational).

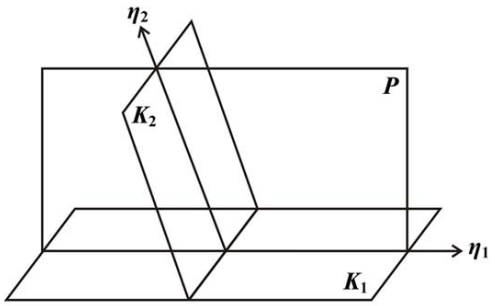

Fig.1.2 The geometrical configuration of K_1, K_2, η_1, η_2 and P.

Twins are usually formed by a homogeneous simple shear of the matrix lattice when the material is strained, in which the resulting structure is identical to that of the matrix, but differently oriented. This type of twinning is termed as deformation twinning which is an important plastic deformation mechanism in many materials. On the other hand, twin structures are often found in the products of many martensitic transformations, *i.e.* transformation twin. Transformation twin produces highly organized structures with alternative twin lamellae of fixed thickness ratios. In many martensites of shape memory alloys, the twin boundaries are highly glissile. Upon the application of a load, the twin boundaries between martensite variants are easily activated to move, thus to accommodate the induced strain, resulting in detwinning of martensite variants with the growing of some energetically favored variants at the expense of others.

1.3 Ni-Mn-Ga Ferromagnetic Shape Memory Alloys

1.3.1 Introduction

Ni-Mn-Ga ferromagnetic shape memory alloys have emerged as a promising new class of smart materials due to the large magnetic-field-induced strains. They can be driven at higher actuation frequency than conventional shape memory alloys. The Ni-Mn-Ga alloys have been already studied for more than 50 years when the initial work exhibited Ni_2MnGa alloy as one of the Heusler alloys having the formula X_2YZ [34-37]. Soltys was the first to concentrate only on the Ni-Mn-Ga alloy system [38]. In 1984, Webster *et al.* firstly investigated the martensitic transformation and magnetic order of Ni_2MnGa [21]. More systematic studies in the 1990's were carried out by Kokorin *et al.* [39, 40], and by Chernenko *et al.* [41], when Ni-Mn-Ga alloys were investigated as potential shape memory alloys. In 1996, Ulakko *et al.* firstly demonstrated a 0.19% field-induced strain in a Ni_2MnGa single crystal sample at 265 K under a magnetic field of 8kOe [7]. Since then, the research interest on magnetic shape memory alloys grew rapidly. In 2000, Murray *et al.* achieved a 6% large magnetic-field-induced strain in a non-stoichiometric Ni-Mn-Ga single crystal with a five-layered martensitie [15]. In 2002, a much larger strain close to 10% was reported by Sozinov *et al.* [8] in the single crystal of a seven-layered martensite, which is the largest magnetic field induced strain obtained in ferromagnetic shape memory alloys. Due to the high fabrication cost of single crystals, the research was also directed towards polycrystalline materials. However, the magnetic field induced strain is almost zero in fine grained alloys. Innovative routes of fabrication, such as films, textured polycrystals and foams, were designed to improve the magnetic field induced strain in polycrystalline alloys. An strain of 0.065% was reported for 0.1-1μm thick films on a 10μm thick Mo substrate [42]. By preparation of highly textured bulk alloy, Gaitzsch *et al.* [43] observed 1% field-induced strain in a polycrystalline alloy. By producing a porous material, the magnetic field induced strain of 0.12% was reported [44]. After a certain training, the magnetic field induced strain in the magnetic

shape-memory alloy foams reached 8.9% [45]. So far, numerous experimental and theoretical studies have been performed on Ni-Mn-Ga alloys, such as crystal structure, phase transformation, magnetic properties, magnetic shape memory effect, mechanical behavior, martensite stability and alloying *et al.*, and interesting phenomena have been revealed.

1.3.2 Magneto-structural transformation in Ni-Mn-Ga alloys

Ni_2MnGa alloy is one of the Heusler alloys with the occurrence of both the paramagentic-ferromagnetic and the thermoelastic martensitic transformation on cooling. The so-called Heusler alloys are highly ordered intermetallics having the common formula X_2YZ with a $L2_1$ order. On cooling from the melt state, Ni-Mn-Ga alloys firstly transform into the B2' phase at about 1100℃. Below the ordering temperature of about 750-800℃, the Heusler phase (austenite) with $L2_1$ long range order is formed. The austenite of Ni-Mn-Ga alloys has a cubic structure with space group $Fm\bar{3}m$ (No. 225) [46], where Ni atoms occupy 8c (0.25, 0.25, 0.25) Wyckoff sites, Mn and Ga atoms 4a (0, 0, 0) and 4b (0.5, 0.5, 0.5) sites, respectively [46], as shown in Fig. 1.3.

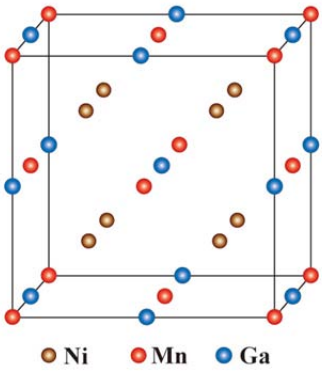

Fig.1.3 Crystal structure of Ni_2MnGa $L2_1$ cubic austenite

On cooling from high temperature, Ni-Mn-Ga alloys undergo paramagnetic-ferromagnetic transformation at the Curie point (T_C). This magnetic transition is one of the main limits when considering the service temperatures of the magnetic shape

memory effect. The T_C of the stoichiometric Ni_2MnGa was reported to be 376K [21]. The T_C of off-stoichiometric Ni-Mn-Ga alloys is less sensitive to the chemical composition [41], having a value of around 370K for a wide range of compositions.

Ni-Mn-Ga alloys are a special case of shape memory alloy and thus they exhibit thermoelastic martensitic transformation on cooling from the parent phase. In some near- stoichiometric alloys, prior to the martensitic transformation at low temperatures, premartensitic transformation occurs and the austenite transforms to micromodulated three-layered (3M) martensite [46]. The premartensitic transformation is characterized by anomalies in the elastic [47-49], thermal [47, 48], resistivity [50, 51] and magnetic properties [48, 50-52]. Inelastic neutron scattering experiments performed on stoichiometric Ni_2MnGa showed the existence of a soft [ξ ξ 0] TA_2 phonon mode over a wide temperature interval. An important observation in these measurements was that the TA_2 phonon branch at a wave vector of $\xi \approx 1/3$ incompletely condenses at the premartensitic transition temperature, which is well above the martensitic transition temperature [53, 54]. This sudden soft mode phonon freezing is the typical character of the premartensite phase and can only be observed in the premartensite phase. Weak spots (or peaks) were found using diffraction techniques by electron [47, 49], neutron [46], and x-ray [55], which can be indexed using a propagation vector of (1/3, 1/3, 0) with cubic symmetry. Based on Landau theory, first principle simulation and phenomenological model have revealed that premartensitic transformation was a kind of weak first order transformation, which is driven by magnetoelastic interaction [56, 57].

The martensitic transformation in Ni-Mn-Ga alloys may result in several martensites. The most frequently observed are five-layered modulated (5M) martensite, seven-layered modulated martensite (7M) and non-modulated martensite (NM). The kind of martensite which appears on cooling depends on the composition, but the stability of the structures seems to be always the same. 5M martensite is the most unstable one; 7M martensite is in the middle and the NM martensite is the most stable one [58]. The alloys displaying a direct transformation to NM martensite typically have martensitic transformation temperatures close or above their Curie

temperatures [59, 60].

The martensitic transformation temperatures (T_M) of Ni-Mn-Ga alloys are highly dependent on the chemical composition [41, 61, 62]. Generally, the increase of the martensitic transformation temperature can be described as a linear function with the average number of valence electrons per atom (electron concentration) *e/a*. Suppose that the number of valence electrons for Ni ($3d^8 4s^2$), Mn ($3d^5 4s^2$) and Ga ($4s^2 4p^1$) atoms are 10, 7 and 3, respectively. The *e/a* can be calculated as follows:

$$e/a = \frac{10 \times (\mathrm{Ni_{at\%}}) + 7 \times (\mathrm{Mn_{at\%}}) + 3 \times (\mathrm{Ga_{at\%}})}{\mathrm{Ni_{at\%}} + \mathrm{Mn_{at\%}} + \mathrm{Ga_{at\%}}}. \quad (1.1)$$

Chernenko *et al.* [41] carefully investigated the composition dependence of martensitic transformation temperatures of Ni-Mn-Ga alloys and concluded that (i) at a constant Mn content, Ga addition lowers T_M; (ii) Mn addition at a constant Ni content increases T_M and (iii) substitution of Ni by Mn at a constant Ga content lowers T_M. Depending on the martensitic transformation temperatures and transformation latent heat, these alloys have been conventionally classified into three groups [61]. Group I ($e/a<7.55$) is composed of alloys with transformation temperatures well below the room temperature and the Curie point. Alloys in Group II ($7.55 \leq e/a \leq 7.7$) have the transformation temperatures around room temperature and below the Curie point, while the alloys in Group III ($e/a>7$) have the transformation temperature above the Curie point.

In addition to the occurrence of martensitic transformation, there also exists a first order inter-martensitic transformation (IMT) in some alloys that transforms one type of martensite to another [63-67]. Depending on the composition and the thermal history of the alloys [63, 66], typical transformation path of inter-martensitic transformation on cooling was reported as from modulated martensite to final NM martensite, such as 5M-7M-NM or 7M-NM. Thus, NM martensite is the ground state of the alloys. The inter-martensitic transformations are usually accompanied by anomalies in the calorimetric, mechanical, magnetic and electrical resistivity both on cooling and heating process [63]. Moreover, the occurrence of inter-martensitic transformation has a certain influence on their practical applicability. In this aspect, it

means that the working range of ferromagnetic shape memory alloys could be restricted to a temperature range where inter-martensitic transformations are not observed, *i.e.* the inter-martensitic transformation may set the lower limit for the service temperature of the magnetic shape memory effect [68].

1.3.3 Crystal structure of martensite

Among the three types of martensite formed after martensitic transformation, the NM martensite has a tetragonal crystal structure with space group I4/mmm (No. 139) [69], while 5M and 7M martensites possess monoclinic superstructure subjected to periodic shuffling along the $(110)_A[1\ \bar{1}\ 0]_A$ system. Shuffling means that transformation shear occurs periodically on the $(110)_A$ plane in $[1\,\bar{1}\,0]_A$ or $[\bar{1}\,10]_A$ direction. In electron diffraction patterns, the lattice modulation is reflected by the satellite spots between two main spots. The distance between the two main reflections is divided into five parts by four satellite spots or seven parts by six satellite spots for 5M and 7M martensite; respectively [70]. Conventionally, the diffraction data is interpreted as that the superstructure is composed of five consecutive subcells for 5M martensite and seven consecutive subcells for 7M martensite.

Generally, two models were commonly used to represent layered martensitic structure. The first one is the long-period stacking order approach [71], which is a well-known method to describe the close-packed layered martensite structure and widely accepted in the studies on Ni-Al alloys and Cu-based shape memory alloys. This method is based on the uniform shear occurring on each basal plane, which is originated from the $\{110\}_A$. It is necessary to use Zhdanov notation to explicitly indicate the stacking sequence, such as $(5\,\bar{2})_2$ for sever-layered martensite. The second approach is to consider the layered structure as a modulation function superimposed onto the basic structure [72]. The deviations of atoms from their ideal positions are defined by the modulation function. The distinction between these two methods is that the long-period stacking order model assumes uniform shear between two neighboring atomic planes, which is the case only when considering the

modulation function with the zero-order harmonic coefficients [73]. In such a context, the stacking order model is the simple case of the modulation function model and it is valid only for a *commensurate* modulated structure [73]. In Ni-Mn-Ga alloys, recent investigations confirmed that the superstructure of modulated martensite can be *commensurate* or *incommensurate* [74, 75], thus, the lattice modulation model is more appropriate.

In spite of the numerous structural characterization works, the crystal structures of modulated martensites are still in dispute. Martynov *et al.* [72, 76] proposed that the structural modulation could be interpreted with a sinusoidal function applied to the (001) planes of the distorted martensite lattice. The displacement of the *j*th plane from the regular position in the shuffling direction can be expressed as:

$$\Delta_j = A\sin(2\pi j/\mathrm{L}) + B\sin(4\pi j/\mathrm{L}) + C\sin(6\pi j/\mathrm{L}) \quad (1.2)$$

where L is the modulation period; *A*, *B* and *C* are constants to achieve the best fit with the observed intensities of the main and satellite spots. For 5M martensite (L=5), *A* = -0.06, *B* = 0.002, *C* = -0.007 [72]. For 7M martensite (L=7), *A* = 0.083, *B*=-0.027, *C*=0 [76]. Ignoring the lattice modulation, Wedel *et al.* used simplified tetragonal crystal structure (*I4/mmm*) and orthorhombic crystal structure (*Fmmm*) to describe the 5M and 7M martensites [77]. By elastic neutron scattering measurement, Zheludev *et al.* [78] found that the 5M modulation of a near-stoichiometric Ni_2MnGa alloy was an *incommensurate* one, in which the modulation was along wave vectors (ξ_M, ξ_M, 0), ξ_M = 0.43. Brown *et al.* [46] performed structural refinement for the thermally induced Ni_2MnGa martensite based on powder neutron diffraction and suggested a *commensurate* seven-layered modulation with orthorhombic crystal structure (*Pnnm*). However, this structure was more likely to be an *incommensurate* 5M modulation. Righi *et al.* applied the superspace theory to fit powder X-ray diffraction patterns and demonstrated that the 5M modulation in Ni-Mn-Ga alloys can be *commensurate* or *incommensurate* [74, 79]. It was revealed that the *incommensurate* 5M modulated structure (*Pnmn*) composed of seven consecutive subcells related to the orthorhombic structure for the stoichiometric Ni_2MnGa alloy [79]; while the Mn-rich alloy has

commensurate structure with five consecutive subcells related to the monoclinic lattice basis (*I2/m*) [74]. Glavatskyy *et al.* reported the refinement results of powder neutron diffraction pattern for the 5M martensite in a non-stoichiometric alloy and also suggested the *commensurate* monoclinic superstructure but with the different space group (*P2/m*) [80]. For 7M martensite, it was reported by Righi *et al.* that the crystal structure was monoclinic (*P2/m*) and the superlattice was *incommensurate* one composed of ten subcells [75]. Recently, Kaufmann *et al.* proposed that the so-called 7M long-period structure is simply composed of nanotwinned tetragonal NM martensite lamellae with $(5\,\bar{2})_2$ stacking sequence, ruling out the existence of the independent modulated structure [81]. Further confirmation and clarification of the most appropriate crystal structure for the modulated martensites are still needed.

1.3.4 Ferromagnetism of Ni-Mn-Ga alloys

The ferromagnetism of Ni-Mn-Ga alloys is mainly from the contribution of the magnetic moment of Mn atoms. Ni atoms only carry a small magnetic moment and the magnetic moment of Ga is negligible [21]. From the magnetization measurements, Webster *et al.* [21] reported that the total magnetic moment of the cubic Heusler phase of Ni_2MnGa is $4.17\mu_B$ per formula unit. A more detailed magnetic analysis was performed by means of polarized neutron scattering measurements and $0.36\mu_B$ for Ni, $2.80\mu_B$ for Mn and $-0.06\mu_B$ for Ga at 100K at the martensite state of Ni_2MnGa were reported [46]. By means of first principles calculations, Ayuela *et al.* reported that the magnetic moments for Ni, Mn and Ga were $0.36\mu_B$, $3.43\mu_B$ and $-0.04\mu_B$, respectively, in the parent phase and $0.40\mu_B$, $3.43\mu_B$ and $-0.04\mu_B$ in the martensite of Ni_2MnGa [82]. The ferromagnetism of Ni-Mn-Ga alloys is interesting because Mn is antiferromagnetic in its pure element state. The change from the antiferromagnetic behavior of pure Mn to the ferromagnetic behavior of Ni-Mn-Ga alloys is due to the increased distance between the Mn sites in the $L2_1$ structure compared with the distance between Mn atoms in pure Mn, which changes the Mn-Mn exchange interaction from antiferromagnetic to ferromagnetic [83].

Magnetocrystalline anisotropy is an intrinsic property of a material in which the magnetization favors preferred directions (easy directions). In Ni-Mn-Ga alloys, the easy axis of magnetization of the parent phase was reported to be $<100>_A$ [84]. The easy axis of magnetization of modulated martensites, *i.e.* 5M and 7M, correspond to the shortest axis of the distorted austenite, *i.e*. *b*-axis of the superlattice. NM martensite has the easy magnetization plane that perpendicular to the *c*-axis.

Magnetocrystalline anisotropy energy, defined as the work necessary to rotate the magnetization from the easy axis to the hard axis with an applied magnetic field, is an important parameter for the achievement of giant magnetic-field-induced strain effects in Ni-Mn-Ga alloys. Magnetocrystalline anisotropy energy is usually expressed by the magnetocrystalline anisotropy constants, which can be acquired by measuring magnetization curves along different crystalline directions. It is reported that the magnetocrystalline anisotropy constant of the austenite for Ni-Mn-Ga alloys is relatively low, of the order of 10^3J/m^3, whereas the anisotropy constant of the martensite is increased by two orders of magnitude [85]. Straka *et al.* systematically studied the magnetic anisotropy of the three types of martensites [85]. At room temperature, for $Ni_{49.7}Mn_{29.1}Ga_{21.2}$ 5M martensite, the anisotropy constant is K_1=1.65×10^5 J/m^3 (K_2 is negligible); for $Ni_{50.5}Mn_{29.4}Ga_{20.1}$ 7M martensite K_1=1.7×10^5 J/m^3 and K_2 =0.9×10^5 J/m^3 referring to the hard and mid-hard axes; and for $Ni_{50.5}Mn_{30.4}Ga_{19.1}$ NM martensite K_1=-2.3×10^5 J/m^3 and K_2 =0.55×105 J/m^3. It should be noted that the magnetic anisotropy constants are temperature and composition dependent [86, 87].

1.3.5 Mechanism of magnetic field-induced strain

The macroscopic shape memory effects induced by magnetic field in Ni-Mn-Ga alloys are the results of field-induced twin variants reorientation [10]. The twin boundary motion can occur when the difference in magnetization energy ($\triangle E_{mag}$) between different martensite variants exceeds the elastic energy needed for twin boundary motion [88]:

$$\triangle E_{mag} \geq \varepsilon_0 \sigma_{tw} \quad (1.3)$$

where ε_0 is the reorientation strain and σ_{tw} is the twinning stress. If the material is magnetized to saturation perpendicularly to the easy axis of one variant and along the axis of the adjacent variant, the difference of the magnetic energy is equal to the difference of the magnetocrystalline anisotropy energy (K_u). The condition for twin boundary motion under magnetic field can be rewritten as [88]:

$$K_u/\varepsilon_0 > \sigma_{tw} + (\sigma_{ext}). \quad (1.4)$$

The term in bracket, σ_{ext}, is the external applied stress applied in the direction perpendicular to the magnetic field direction. This equation describes the usual setup of an actuator.

When an external magnetic field is applied, the variants with their magnetization vectors aligning along the applied field are more energetically favorable and they will increase the volume fraction at the expense of the other variants through the twin boundary motion, leading to the macroscopic shape change of the sample, namely magnetic field induced strain [58]. The schematic illustration of the rearrangement of the martensite variants under a magnetic field is shown in Fig. 1.4. So far, large strains up to ~6% and ~10% have been reported in 5M [15] and 7M martensite [8], while the strain induced by magnetic field in NM martensite is negligible [89].

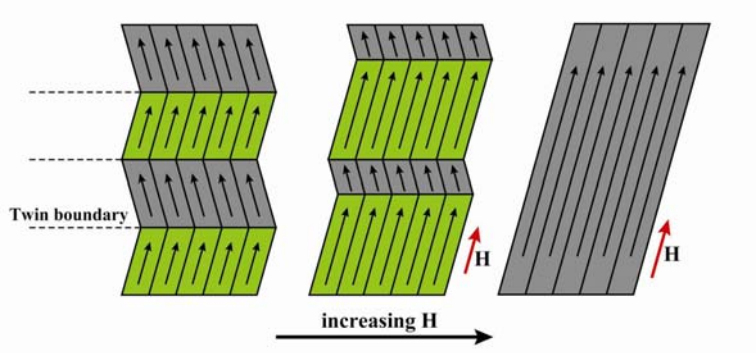

Fig 1.4 Illustration of the rearrangement of martensite variants under a magnetic field in ferromagnetic shape memory alloys (FSMAs) [58].

In general, the shape change achieved by the rearrangement of martensite variants under an applied field is not recovered when the magnetic field is switched off. To

recover the strain induced by magnetic field, one possibility is to rotate the magnetic field [90]. Another possibility is to apply a external stress perpendicular to the direction of the field [91]. Assume that in the absence of the magnetic field, the martensite is at single-variant stage and it is favored by the stress. On applying a magnetic field, if the maximum magnetic stress (K_u/ε_0) overcomes the sum of the twinning stress and the external stress, the stress-favored variant transforms to a different variant which is favored by the magnetic field, resulting in a large shape change. When the magnetic field is switched off, if the twinning stress is very low and the external stress exceeds the twinning stress, fully reversible behavior can be obtained. The condition for full reversibility of the magnetic shape memory effect can be written as [88]

$$K_u/\varepsilon_0 - \sigma_{tw} > \sigma_{ext} > \sigma_{tw} \quad (1.5)$$

This equation reflects the fact that high magnetic anisotropy (K_u) and low twinning stress (σ_{tw}) are requisites for the occurrence of magnetic shape memory. It also shows that too large external stresses will inhibit twin boundary motion.

In principal, the magentocrystalline anisotropy energy can be increased by increasing the saturation magnetization and Curie temperature (T_C). It is reported that the Curie temperature and the saturation magnetization of Ni-Mn-Ga alloys are less sensitive to the composition [41, 92]. The easiest way to increase the magnetocrystalline anisotropy energy is to choose an operating temperature (T_O) significantly lower than T_C since the magnetocrystalline anisotropy energy increases with decreasing temperature below T_C [91]. Similarly, twinning stress also increases with decreasing temperature below transformation temperatures [93]. Therefore, it is critical to understand and quantify the relationship between magentocrystalline anisotropy energy, twinning stress, operating temperature, T_C and transformation temperatures to select materials and operating temperatures for obtaining high blocking stress (the external stress level above which magnetic field induced reorientation is not possible) and magentocrystalline anisotropy energy.

In many cases, the observed the twinning stress exceeds the stress induced by magnetic field due to the interlocked variants with various orientation. The variants

can not be actuated to reorient by magnetic field. Training is necessary to reduce the variant number and the twinning stress, thus to increase the induced strain. Very effective training biases the twin microstructure and leads to the formation of a single-variant or simple two-variant crystal. The common training methods include mechanical training, thermo-mechanical or thermo-magnetic training and magneto-mechanical training. For mechanical training, the repeated mechanical deformation is performed in orthogonal directions [43]. For thermo-mechanical or thermo-magnetic training, a mechanical stress or a magnetic field is applied during the martensitic transformation [94]. Magneto-mechanical training occurs in the martensitic phase by rotating the magnetic field or repetitive mechanical deformation perpendicular to the external magnetic field [90]. Sozinov *et al.* reported a remarkable decrease in the twinning stress from about 11 MPa to about 3 MPa after three compressions of 7M martensite [95]. The continuous compressions were made in order to create a single-variant specimen, which showed about 1 MPa twinning stress and the magnetic shape memory effect with nearly 10% strain. James *et al.* reported the observation of the magnetic shape memory effect with 0.5% strain, but a much larger strain of about 4% when the specimen was previously cooled under stress through martensitic transformation (stress cooling) [94]. Straka *et al.* [96] generated a simple two variant state by repeated compressive deformation. The training lead to a decrease of the twinning stress from 3.2 MPa directly after thermo-mechanical training to 1.1 MPa in a 5M martensite sample and from 6.3 MPa to 2.9 MPa for a 7M martensite sample. Müllner *et al.* preformed cyclic experiments in a rotating magnetic field on 7M martensite [90]. The magnetic field induced strain increased from the initial 6% to 9.7%.

1.3.6 Crystallographic orientation relationship of Ni-Mn-Ga alloys

As the field-induced effect originates from the reorientation of martensite variants through a detwinning and twinning process, the microstructural configuration and crystallographic correlation of constituent martensite variants have strong

influence on the activation of the magnetic shape memory effect (output strain and dynamic response). Thus, comprehensive crystallographic knowledge on the microstructural features of martensite variants and variant boundaries is desired, from which a clear image of structure-property relation is built up and also necessary indications for further precise control and improvement of properties are presented.

So far, constant efforts have been devoted to the study of orientation relationships between martensite variants by means of X-ray diffraction (XRD) [97] and transmission electron microscopy (TEM) [98-100]. Mogylnyy *et al.* successfully determined the twinning mode in a Ni-Mn-Ga single crystal with 5M martensite by X-ray diffraction methods [97]. Han *et al.* [98, 99] investigated the orientation relationship between the martensite variants in 5M and 7M martensite by TEM. It was found that there exists a twin relationship between the variants in both 5M and 7M martensite. The twinning plane in 5M martensite is $\{1\,\bar{2}\,\bar{5}\}_{5M}$, while that in 7M martensite is $\{1\,\bar{2}\,\bar{7}\}_{7M}$. More systematic TEM investigation on twin types and twinning elements in 5M and 7M martensite were presented by Nishida *et al.* [100]. However, the XRD analysis suffers a limit on acquiring simultaneously the spatial microstructural information of the measured orientations, which prevents the identification of orientation-microstructure correlation. In contrast, the TEM analysis enables one to reveal the variant morphology and the inter-variant orientation relationships, but the exploitable area is too local. Hence, it is difficult to obtain a global orientation image of multi-variants. It has also been noted that for the *incommensurate* modulation, the number of the observed satellites plus the main reflection does not conform to the number of the subcells in the superstructure [75]. Apparently, the habitual interpretation of the structural modulation according to TEM observation is not suited for the determination of the lattice constants and hence the orientations of the martensite variants [100], and needs to be reconsidered. Moreover, due to the limitation of TEM observation, the crystallographic nature of inter-variant interfaces and their statistical distributions has also not been well addressed.

With the mature of SEM/EBSD technique, large-scale spatially resolved

orientation examination has made the correlation between microstructure and crystallographic orientation possible, which overcomes the above mentioned limitations. The merits of EBSD measurements lie on that, firstly, it provides an alternative means for verifying the crystal structure information, as the EBSD-based orientation determination requires the complete crystal structure information including the lattice constants and the atomic position of each atom in the unit cell; secondly, it enables the automatic orientation mapping of individual martensite variants, which correlates the crystal structure and orientation information with the morphologic features on an individual variant basis; thirdly, it allows an unambiguous determination of the orientation relationships of adjacent variants and the twin interface planes, and thus a full crystallographic analysis on a bulk sample with statistical reliability.

Cong *et al.* systematically investigated the twinning relationship of NM martensite in a $Ni_{53}Mn_{25}Ga_{22}$ alloy by means of SEM/EBSD [101, 102]. The twinning elements were fully determined and the inter-plate interfaces were found to be close to $\{112\}_{Tet}$ twinning plane with 2.6° deviation. In modulated martensite, some pioneer work has been done to characterize the global microstructures and variant orientations using approximate structure information [103-107]. For instance, the simplified tetragonal crystal structure was used to approximate the 5M modulated monoclinc superstructure, considering that the monoclinic angle of the modulated structure is very close to 90° and the difference between the basis vector *a* and *b* is very small. As a consequence of that, crystallographic nature was not fully disclosed. Especially, the variant number was not detected accurately. Further efforts should be made for the full disclose of the microstructural features and the crystallographic characteristics concerning the number and the shape of the martensite variants, the inter-variant orientation relationships and the twin interfaces.

One the other hand, the key factor behind the magnetic shape memory effect in Ni-Mn-Ga alloys is the martensitic transformation below a certain temperature. The microstructural configuration of martensite variants and their crystallographic

correlation results directly from the martensitic transformation that follows certain specific orientation relationships (ORs) between the parent phase and the product phase. Thus, the determination of possible phase transformation orientation relationships in Ni-Mn-Ga alloys is of practical importance for their microstructure control and theoretical interest for insight into their martensitic transformation process. However, in most of the alloys, the transformation is complete. It is difficult to obtain a mixed microstructure consisting of austenite and martensite, thus to determine the orientation relationship between the two phases. An alternative option for the determination of the transformation OR is to calculate the orientations of parent austenite from the orientations of the transformed martensite variants under an assumed OR [108], and then to identify the most favorable OR. Recently, a specific OR between austenite and NM martensite, namely the K-S relation with $(111)_A//(101)_{Tet}$ and $[1\ \bar{1}\ 0]_A//[11\ \bar{1}\ ]_{Tet}$, was predicted by Cong *et al*. based on experimental measurements and crystallographic calculations, representing a substantial advance in the study of martensitic transformation in Ni-Mn-Ga alloys [102]. Further efforts should be made on complete description of the phase transformation OR between austenite and modulated martensie.

1.4 Content of the present work

During the last twenty years, extensive investigations have been devoted to understanding the shape memory behaviors of Ni-Mn-Ga alloys. However, as Ni-Mn-Ga ferromagnetic shape memory alloys are newly emerging materials, there are still many fundamental issues that need to be further explored. Some obtained results are still in controversial due to the limitations of the characterization techniques. Electron backscatter diffraction (EBSD) measurement, as a promising tool for crystallography investigation, directly correlates the spatial crystallographic orientations with the morphological characters and allows a larger scale of measurement on the bulk sample. However, due to the complexity of structural modulation of the modulated martensite phase, there are seldom EBSD characterizations by application of superstructure information. Consequently, many crystallographic natures have not been correctly revealed.

Based on such a background, the present work was designed to perform a thorough crystallographic investigation on different kinds of martensite in Ni-Mn-Ga alloys, *i.e.* 7M, 5M and NM martensite, based on EBSD orientation and microstructural examination techniques. The superstructure information of modulated martensites was applied for the orientation determination. The main content of the present work will focus on:

(1) Precisely determine variant number, the orientation relationships of adjacent variants and the variant interface planes of 5M and 7M martensite by using the precise superstructure information for the EBSD auto-orientation mapping.

(2) Determine the most favorable orientation relationship between austenite and modulated martensites based on the experimentally acquired orientation data and crystallographic calculation.

(3) Examine the morphology and crystallographic features of NM martensite by EBSD measurements and crystallographic calculations.

(4) Study the self-accommodation mechanism of modulated martensite. Reveal

the thermodynamic stability and crystal structure nature of modulated martensite. Clarify the role of the modulated martensite in the transformation from the austenite to NM martensite.

Chapter 2 Experimental and calculation methods

2.1 Alloy preparation

Ni-Mn-Ga polycrystalline alloys with different nominal composition were dedicatedly prepared, aiming to obtain different kinds of martensite at room temperature. High purity elements Ni (99.97 wt.%), Mn (99.9 wt.%) and Ga (99.99 wt.%) were used as raw materials to prepare as-cast ingot. The alloys were melted in arc-melting furnace with water-cooled copper crucible under argon atmosphere.

The weight of each target ingot was about 70-80g. Prior to be melted, the pure raw materials were weighed by an electronic balance according to the designed nominal composition with the precision of 0.01g. To reduce the loss of Mn caused by strong evaporation during melting, the pure Mn was placed at the bottom of the crucible before melting. Each alloy was melted for four times and the electromagnetic stirring was applied during melting process for the composition homogenization. The final as-cast ingot had a button-shaped appearance, as shown in Fig 2.1a. To reduce microcracks and porosity, some ingots were remelted and then fast solidified by suction casting into a chilled copper mold with 6mm in diameter, through which a rod was obtained, as shown in Fig 2.1b.

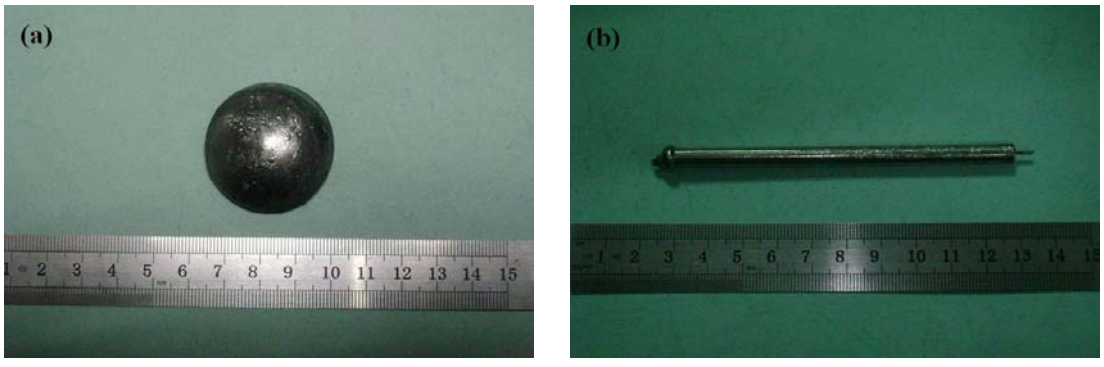

Fig 2.1 Macroscopic appearance of prepared alloys. (a) as-cast; (b) suction-cast.

To further reduce the composition inhomogeneity in the prepared alloys, the alloys were sealed in a vacuum quartz tube and then homogenized at 900°C for 24h. Finally, they were quenched in the water by breaking the quartz tube.

2.2 Sample preparation

The samples for compressive testing with dimension of Φ6mm×5mm were cut by electrical discharge wire-cutting. The small cylindrical samples were mechanically polished with SiC grinding paper.

To prepare the samples for the powder X-ray diffraction (XRD) measurement, parts of the homogenized alloys were crushed and ground into powder. To release the stress introduced by grinding, the powder was sealed in vacuum quartz tubes and annealed at 600℃ for 5 hours.

Rectangular parallelepiped bulk samples for microstructure observation and electron backscatter diffraction (EBSD) measurements were cut out of the as-cast button or suction cast rod by electrical discharge wire-cutting. For the preparation of suitable observation plane, all the samples were first mechanically polished with SiC grinding paper. Then they were electrolytically polished in a solution of 20% nitric acid in methanol at room temperature with the voltage of 12V for 30 seconds.

The samples for transition electron microscope (TEM) observation were mechanically thinned to ~100μm. Then the thin foils were electrolytically thinned in a twin-jet device at room temperature with the same solution as mentioned above.

2.3 Characterization methods

2.3.1 Optical microscopy

The microstructure observations after polishing were firstly performed with OLYMPUS BX61 optical microscope equipped with polarized light. The microstructure evolution during inverse martensitic transformation for the alloys with the martensitic transformation temperatures around room temperature was also observed with the optical microscope. The sample was firstly pre-cooled into the full martensite state and then subjected to the optical microscope observation at room temperature.

2.3.2 Mechanical property testing

The mechanical properties of the as-cast alloys and the suction-cast alloys were measured by compressive testing using a CMT5305 Electronic Universal Testing Machine. The load was applied by controlling the displacement with a compressing rate of 0.2mm/min. The sample was loaded till fractured.

2.3.3 Differential scanning calorimetry

The forward and backward martensitic phase transformation temperatures for the prepared alloys were measured by differential scanning calorimetry (DSC). A Q100 DSC device, TA Instruments, was used in the present work. During DSC experiments, two crucibles were placed next to each other. One crucible was empty functioning as a reference and the other was filled with the sample to be measured. The two crucibles were heated and cooled under the same experimental setting. The heat flux in and out of a specimen at a specific temperature was determined and recorded by comparing the sample temperature with that of the reference. The heating and cooling rates for the measurement were set to be 10℃/min under a constant flow of Argon. The martensitic transformation temperatures were determined by tangent method using the heat flux peaks in the DSC curve during heating and cooling.

2.3.4 X-ray diffraction

The crystal structures of the alloys were determined by means of X-ray diffraction (XRD). The XRD measurements were preformed in a PANalytical X'Pert Pro MPD diffractometer with a heating and cooling stage. The stress-free powder samples were used for the measurements. The XRD patterns were measured in the 2θ range of 20-120° with a step size of 0.0334° using Cu K_α radiation. The lattice parameters of the alloys were determined from the experimental XRD patterns by fitting the diffraction profiles using Powder Cell software [109].

2.3.5 Scanning electron microscopy

For detailed microstructural analyses, the field emission gun scanning electron microscope (SEM) Jeol JSM 6500 F was used. Additionally to the ability of detecting secondary electrons, the SEM is also equipped with a backscattered electron detector, an energy dispersive X-ray spectrometry (EDS, BRUKER, Germany) and an electron backscatter diffraction camera.

The morphological features were characterized by secondary electron (SEI) imaging and backscattered electron (BSE) imaging. The composition of the alloy was verified by EDS.

Electron backscatter diffraction (EBSD) was applied for the orientation acquisition. In the present work, the orientation measurements were performed in a field emission gun scanning electron microscope (Jeol JSM 6500 F) with EBSD acquisition camera and *Channel 5* software. The working voltage was set at 15KV. The detailed crystal structure information was input into the *Channel 5* software to construct the corresponding database for Kikuchi indexing. The orientation data were manually and automatically acquired. The beam control mode was applied for automatic orientation mapping. To ensure the indexation accuracy using the monoclinic superlattice for 7M and 5M martensite, the minimum number of detected bands is set to be 10 and 15, respectively. The maximum allowed MAD that represents the mean angular deviation between the calculated and the experimental

EBSD pattern was set to be 1. For the case of 5M martensite, as the monoclinic angle is very close to 90°, it is unavoidable that there exist misindexations in the orientation map. For the determination of correct crystallographic orientation and variant number, we firstly judged and acquired the orientation data manually, then replaced the misindexations in the map by the post treatment.

2.3.6 Transmission electron microscopy

TEM is capable of imaging at a significantly higher resolution than optical microscopy and SEM, which enables the research to examine fine detail of the microstructure. Here, a Philips CM 200 LaB_6 cathode TEM was used to observe the stacking faults inside the martensite plates. A Gatan MSC 792 CCD camera was used to acquire the images. The working voltage was set at 200KV.

2.4 Crystallographic calculation method

2.4.1 Coordinate transformation between orthonormal reference system and monoclinic system

By convention, individual orientations acquired by EBSD measurement are represented by a set of rotations expressed in Euler angles (φ_1, Φ, φ_2) [110] transforming the macroscopic sample coordinate system to the orthonormal crystal coordinate system. The transformation between two coordinate systems can also be represented by the following rotation matrix G and its inverse matrix:

$$G = \begin{pmatrix} \cos\varphi_1\cos\varphi_2 - \sin\varphi_1\sin\varphi_2\cos\Phi & -\cos\varphi_1\sin\varphi_2 - \sin\varphi_1\cos\varphi_2\cos\Phi & \sin\varphi_1\sin\Phi \\ \sin\varphi_1\cos\varphi_2 + \cos\varphi_1\sin\varphi_2\cos\Phi & -\sin\varphi_1\sin\varphi_2 + \cos\varphi_1\cos\varphi_2\cos\Phi & -\cos\varphi_1\sin\Phi \\ \sin\varphi_2\sin\Phi & \cos\varphi_2\sin\Phi & \cos\Phi \end{pmatrix} \tag{2.1}$$

In this study, the orthonormal crystal coordinate system is linked to the monoclinic crystal coordinate system by setting $\boldsymbol{c_M}//\boldsymbol{k}$, $\boldsymbol{b_M}//\boldsymbol{j}$ and $\boldsymbol{a_M}$ in $\boldsymbol{i}$-O-$\boldsymbol{k}$ plane, where the $\{\boldsymbol{i}, \boldsymbol{j}, \boldsymbol{k}\}$ and $\{\boldsymbol{a_M}, \boldsymbol{b_M}, \boldsymbol{c_M}\}$ are respectively the basis vectors of the orthonormal crystal system and the monoclinic crystal system, as shown in Fig. 2.2. Let (h_M, k_M, l_M) and [u_M, v_M, w_M] be the respective Miller indices of a given lattice plane and direction in the monoclinic crystal system. Their corresponding coordinates (n_1, n_2, n_3) and [u, v, w] in the orthonormal crystal system are then given by:

$$\begin{pmatrix} n_1 \\ n_2 \\ n_3 \end{pmatrix} = \begin{pmatrix} \dfrac{1}{a_M \sin\beta} & 0 & \dfrac{-\cos\beta}{c\sin\beta} \\ 0 & \dfrac{1}{b_M} & 0 \\ 0 & 0 & \dfrac{1}{c_M} \end{pmatrix} \begin{pmatrix} h_M \\ k_M \\ l_M \end{pmatrix} \tag{2.2}$$

$$\begin{pmatrix} u_1 \\ v_1 \\ w_1 \end{pmatrix} = \begin{pmatrix} a_M \sin\beta & 0 & 0 \\ 0 & b_M & 0 \\ a_M \cos\beta & 0 & c_M \end{pmatrix} \begin{pmatrix} u_M \\ v_M \\ w_M \end{pmatrix} \tag{2.3}$$

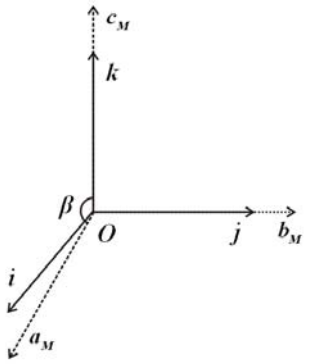

Fig.2.2 Schematic representation of the monoclinic crystal system and the orthonormal crystal system.

2.4.2 Misorientation calculation

The misorientation between two crystals (described by the orthonormal reference systems) is defined by sets of rotations from one of the symmetrically equivalent coordinate systems of one crystal to another equivalent coordinate system of the other crystal.

Let us consider two adjacent variants 1 and 2. The misorientation between them can be expressed in matrix notation [101]:

$$\Delta g = S_i^{-1} G_1^{-1} G_2 S_j \tag{2.4}$$

where Δg is the misorienation matrix; G_1 and G_2 are the rotation matrices transforming the orthonormal sample coordinate system to the orthonormal coordinate system set to the lattice basis of the respective variants; S_i and S_j are the symmetry elements; the superscript "-1" denotes the inverse of a matrix. If we denote

$$\Delta g = \begin{pmatrix} g_{11} & g_{12} & g_{13} \\ g_{21} & g_{22} & g_{23} \\ g_{31} & g_{32} & g_{33} \end{pmatrix}, \tag{2.5}$$

then, the misorientation angle ω and rotation axis **d** (d_1, d_2, d_3) can be expressed as follows:

(1) $\omega \neq 180°$and $\omega \neq 0°$

$$\omega = \arccos\left(\frac{g_{11} + g_{22} + g_{33} - 1}{2}\right) \tag{2.6}$$

$$\mathbf{d} = (d_1, d_2, d_3) = \left(\frac{g_{23} - g_{32}}{2\sin\omega}, \frac{g_{31} - g_{13}}{2\sin\omega}, \frac{g_{12} - g_{21}}{2\sin\omega}\right). \quad (2.7)$$

(2) $\omega = 180°$

$$\mathbf{d} = (d_1, d_2, d_3) = \left(\frac{g_{11} + 1}{2}, \frac{g_{22} + 1}{2}, \frac{g_{33} + 1}{2}\right)$$

$$\text{with} \begin{pmatrix} |d_m| = \max(|d_i|, i = 1,2,3) \\ d_m > 0, \text{by convention} \\ \forall\, i \neq m, \operatorname{sgn}(d_i) = \operatorname{sgn}(g_{im}) \end{pmatrix} \quad (2.8)$$

(3) $\omega = 0°$

$$\mathbf{d} = (d_1, d_2, d_3) = (1, 0, 0) \quad \text{(by convention)} \quad (2.9)$$

Chapter 3 Characterization of Ni-Mn-Ga martensites

3.1 5M martensite

For Ni-Mn-Ga ferromagnetic shape memory alloys, the crystallographic features of modulated martensite (including the number of constituent variants, the inter-variant orientation relationship and the geometrical distribution of variant interfaces) determine the attainability of the shape memory effect. In this section, a comprehensive microstructural and crystallographic investigation has been conducted on a bulk polycrystalline $Ni_{50}Mn_{28}Ga_{22}$ alloy. As a first attempt, the orientation measurements by EBSD using the precise information on the commensurate 5M modulated monoclinic superstructure (instead of the simplified non-modulated tetragonal structure) were successfully performed to identify the crystallographic orientations of martensite variants. Consequently, the morphology of the modulated martensite, the orientation relationships between adjacent variants and the twin interface planes were unambiguously determined. Based on the correct orientation data of the martensite variants acquired from EBSD measurement, the favorable orientation relationship (OR) between austenite and 5M martensite was revealed by detailed crystallographic calculation with no residual austenite.

3.1.1 Crystal structure of 5M martensite

The off-stoichiometric Mn-rich Ni-Mn-Ga polycrystalline alloy, with nominal composition of $Ni_{50}Mn_{28}Ga_{22}$ (at. %), was prepared by arc-melting. By means of energy-dispersive X-ray analysis (SEM/EDX), the composition of the alloy was verified to be $Ni_{50.1}Mn_{28.3}Ga_{21.6}$ (at. %). According to the DSC measurements, the austenite to martensite transformation started at 43.8 °C (M_s) and finished at 30.0 °C (M_f) upon cooling. The reverse transformation started at 41.1 °C (A_s) and finished at 51.3 °C (A_f) upon heating.

Fig. 3.1a shows the powder X-ray diffraction (XRD) pattern of the $Ni_{50}Mn_{28}Ga_{22}$

alloy measured at room temperature. By examining the individual diffraction peaks and their intensities over the profile, it was found that the XRD pattern is very similar to those published for the commensurate 5M modulated martensite with close composition [74, 97, 111]. The only difference is that the respective peaks recorded here deviate slightly from the reported positions. This suggests that the present alloy possesses the same crystal structure, *i.e*. a commensurate 5M modulated structure depicted with a superlattice composed of five consecutive subcells [74], but the lattice constants are slightly different. With the information of the atomic coordinates (as show in Appendix I) in the superlattice, the space group (*P2/m*; *No. 10*) and the lattice constants from the ref. [80] as the initial input, the measured XRD pattern was then fitted using the *Powder Cell* software [109]. Eventually, the lattice parameters were determined to be a_{5M} = *4.226 Å,* b_{5M} = *5.581 Å,* c_{5M} = *21.052 Å* and β = *90.3°* for the present alloy. As shown in Fig. 3.1b, the recalculated peak positions resulting from the superstructure model and the optimized lattice constants are in good agreement with the measured ones (Fig. 3.1a). In such a case, the easy magnetization axis of the 5M modulated martensite is along the *b* axis of the superlattice, *i.e.* the [010] direction.

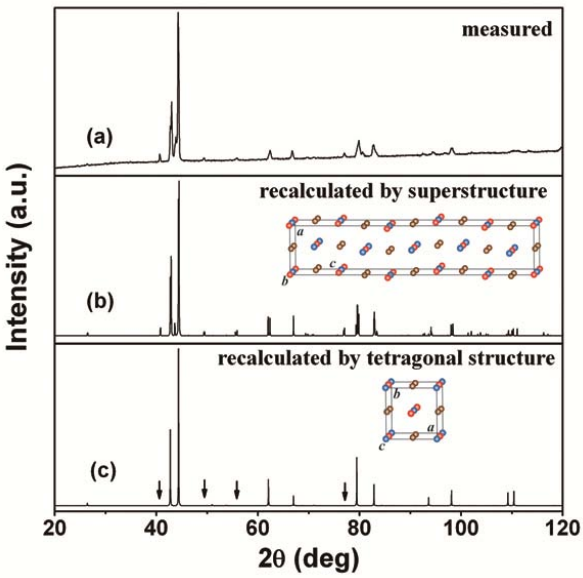

Fig.3.1 XRD patterns of $Ni_{50}Mn_{28}Ga_{22}$ alloy at room temperature: (a) measured; (b) recalculated according to the commensurate 5M superstructure; (c) recalculated according to the non-modulated tetragonal crystal structure. The insets show the unit

cell of the corresponding structures.

It is noted that, in the pioneering EBSD orientation measurements on the same kind of alloys [103-107], the 5M modulated martensite was usually approximated by a non-modulated tetragonal structure (*I4/mmm*, *No. 139*) [77] as the monoclinic angle is very close to 90° and the difference between a_{5M} and $c_{5M}/5$ is very small. Using this simplified structure (a=b=4.226Å, c=5.581Å), the XRD pattern was also recalculated in a similar way, as shown in Fig. 3.1c. It is evident that the diffraction peaks related to the monoclinic distortion, the orthorhombic distortion and the lattice modulation (arrowed positions) do disappear in the recalculated pattern. This indicates that the approximation of the 5M modulated superstructure with a non-modulated tetragonal structure may lead to an incorrect EBSD orientation identification, due to the loss of the important structure modulation information.

3.1.2 Microstructural features of 5M martensite

Fig. 3.2a shows a typical backscattered electron (BSE) image of the 5M martensite taken at room temperature. According to the gray-level contrasts in the image, the microstructural features can be characterized as alternatively distributed broad plate with 10-20 micrometers in width and separated by inter-plate boundaries. Moreover, the plates with light mean contrast consist of sub-plates and those with dark mean contrast consist of blocks. It is seen from Fig. 3.2b - the zoomed image of the marked frame in Fig. 3.2a - that the broad plates are composed of pairs of thin lamellae with the thickness in the nanometer range. In each pair, one plate is thicker than the other. The thin lamellae are bound by long and short inter-lamellar interfaces. The bending at the short inter-lamellar interfaces is accompanied with contrast change in the BSE image. The short interfaces mark the sub-plates interfaces and the block interfaces. According to the BSE contrast of nanoplates, there are always four types of martensite variants that are locally interconnected. As the martensite is a mono-phase and has a homogeneous chemical composition, the contrast changes in the BSE image should be attributed to the orientation variations. This will be clarified by the

following EBSD orientation determination.

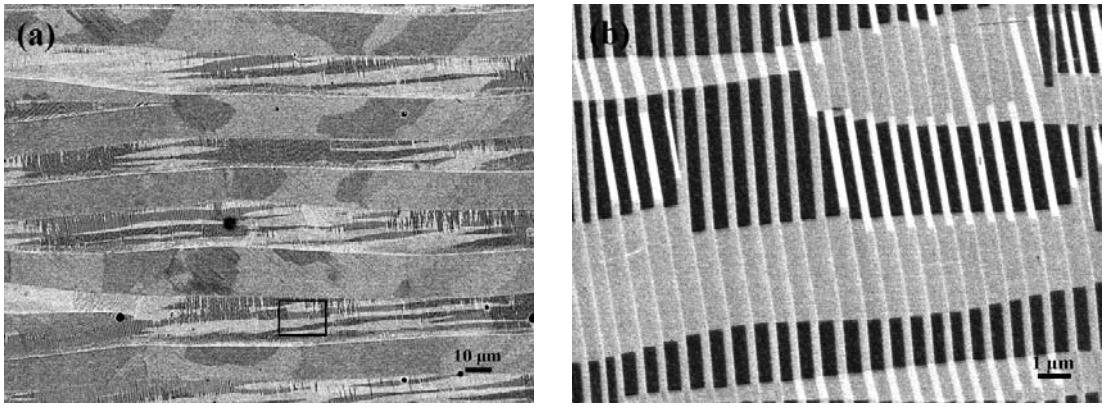

Fig.3.2 Typical BSE images of commensurate 5M martensite: (a) broad martensitic plates in an initial austenite grain; (b) fine lamellae in the marked square frame in (a).

3.1.3 Orientation identification of 5M martensite

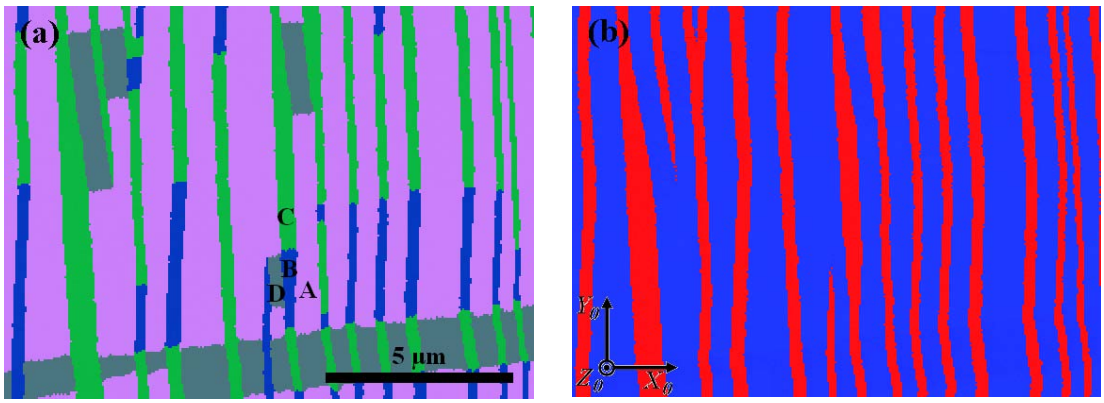

Fig.3.3 EBSD maps of fine lamellae reconstructed according to orientation identification with (a) the commensurate 5M superstructure and (b) the non-modulated tetragonal crystal structure. There are four types of variants (designated as A, B, C and D) in (a), but only two types of variants in (b). The coordinate frame (X_0 Y_0 Z_0) refers to the macroscopic sample coordinate system.

By applying the superstructure information of the commensurate 5M martensite to the Kikuchi pattern indexation, the orientation map of the fine lamellae in the broad plates was reconstructed as shown in Fig. 3.3a, where the individual fine lamellae were colored according to their orientations. For comparison, the orientation map - generated for the same region by using the non-modulated tetragonal crystal structure

(*I4/mmm*, *No. 139*) with lattice parameters *a=b=4.226Å, c=5.581Å* - is shown in Fig. 3.3b. Notably, there are four local orientation variants (hereafter martensite variants) as marked A, B, C and D in Fig 3.3a, but only 2 variants (A and C or B and D) in Fig 3.3b. This suggests that the Kikuchi pattern indexation with the simplified non-modulated tetragonal crystal structure would not allow the full identification of martensite variants when the fine lamellae are bent lengthwise.

To further demonstrate the orientation difference across the bent fine lamellae, the Kikuchi patterns (Fig. 3.4a and b) were acquired from two manually chosen positions at lamellar *1* and *2* (the right upper corner of Fig. 3.4a). It is seen that the general layouts of the two patterns are similar but the details surrounding some of the main reflection bands reveal differences. The two sets of diffraction bands - marked respectively with a thick white line plus a thin white line for one set and a black thick line for the other in Fig. 3.4a and b - interchange their positions, as a result of the orientation change from lamellar *1* to *2*. The two Kikuchi patterns were also indexed with the 5M modulated superstructure and the non-modulated tetragonal structure, as displayed in Fig. 3.4c and d, and Fig. 3.4e and f, respectively. The resultant orientations represented with a set of three Euler angles (in Bunge's notation [110]) with respect to the sample coordinate system are given at the right bottom of each indexed pattern. Note that the two patterns indexed with the modulated monoclinic superstructure represent two different orientations (Fig. 3.4c and d), whereas under the tetragonal structure, the indexation solutions of the two patterns are the same, with a very small deviation in the Euler angles (Fig. 3.4e and f) due to measurement imprecision. Indeed, the perfect fit between the measured pattern and the indexed one, as shown in Fig. 3.4c and d, confirms the validity of the commensurate 5M modulated structure information determined with the superstructure model [80]. In contrast, erroneous indexing arises in the indexation solution from non-modulated tetragonal structure. Such oversimplification of the structure modulation results in incorrect orientation identification, and consequently misinterpretation on crystallographic aspects concerning the variant number, inter-variant orientation relationships and martensitic transformation crystallography.

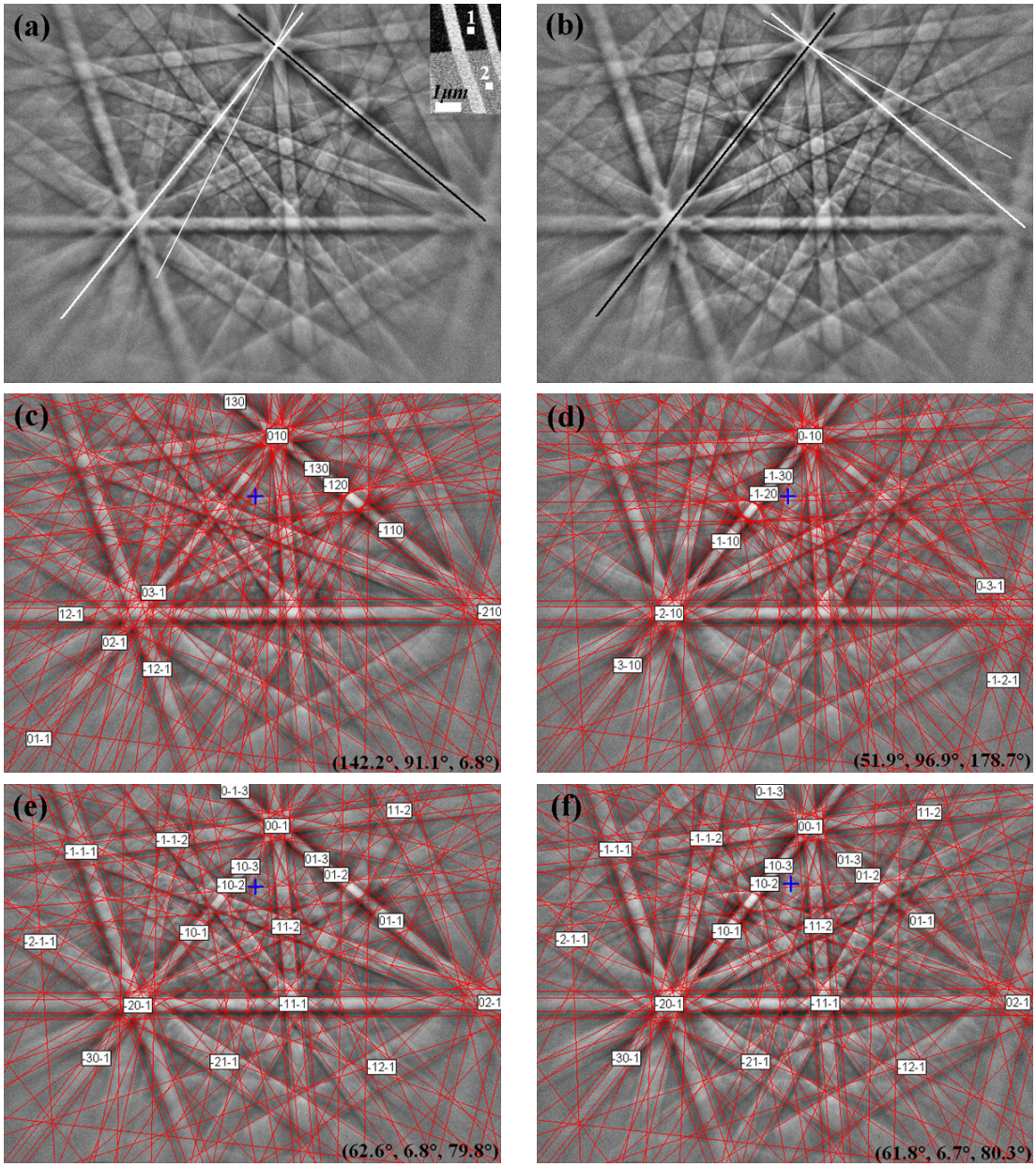

Fig.3.4 Kikuchi patterns showing the orientation difference across bended fine lamellae: (a) and (b) acquired from two measured positions marked in the inset of BSE image in Fig. 3.4 (a); (c) and (d) recalculated patterns using the commensurate 5M superstructure; (e) and (f) recalculated patterns using the non-modulated tetragonal crystal structure. A set of three Euler angles with respect to the sample coordinate system are listed in each recalculated pattern.

3.1.4 Orientation relationships between martensite variants

With the correct orientation data of the individual martensite variants determined

by EBSD measurements, the inter-variant orientation relationships can be further calculated in terms of misorientation angle/axis, *i.e.* a set of misorientation angles around the corresponding rotation axes. By taking into account possible combinations of the four types of variants A, B, C and D in Fig. 3.3a, the complete sets of misorientation angles (ω) and the corresponding rotation axes (**d**) were calculated according to Eq. (2.4) and are shown in Table 3.1.

Table 3.1 Misorientation angles (ω) and rotation axes (**d**) between variants A, B, C, and D in Fig. 3.3a. The rotation axes refer to the orthonormal crystal coordinate frame set to the monoclinic martensite lattice basis.

Variant pair	Misorientation angle ω [°]	Rotation axis, **d**		
		d_1	d_2	d_3
A:C	86.80	-0.70846	0.00241	-0.70575
	179.81	0.48490	-0.72659	-0.48676
B:D	86.79	-0.71242	-0.00221	-0.70175
	179.83	-0.48214	0.72661	0.48947
A:B	93.32	0.70870	0.00098	0.70551
	179.92	-0.51312	-0.68633	0.51543
C:D	93.09	0.70882	0.00435	0.70538
	179.64	-0.51205	-0.68778	0.51455
A:D	179.64	0.70487	-0.00098	-0.70933
	179.89	-0.70933	0.00317	-0.70487
B:C	179.88	0.70978	0.00079	0.70443
	179.91	-0.70443	-0.00102	0.70978

Owing to the monoclinic symmetry, there are two sets of distinct misorientations (angle-axis) for each variant pair. Among them, variant pairs A:C and B:D, A:B and C:D, A:D and B:C have almost identical sets of rotations. It is seen that each pair of variants possesses at least one 180° rotation, suggesting that all the variant pairs are twin related according to the classical definition of twinning [32, 112]. By further transforming the rotation axes into the monoclinic crystal basis, it demonstrates that for variant pair A:C (or B:D) the 180° rotation axis is close to the normal of the rational plane $(1\,\bar{2}\,\bar{5})_{5M}$ (with 0.39° deviation), whereas for the variant pair A:B (or C:D) the 180° rotation axis is close to the rational direction $[\bar{5}\,\bar{5}\,1]_{5M}$ (with 0.33°

deviation). As for the variant pair A:D (or B:C), two 180° rotation axes exist that are perpendicular to each other, being close to the normal of the rational plane $(105)_{5M}$ (with 0.23° deviation) and the rational direction $[\bar{5}01]_{5M}$ (with 0.15° deviation), respectively. The small deviations from the rational planes/direction with low indices may be attributed to the experimental inaccuracy caused by the EBSD measurements. Following the rationality criterion of the Miller indices of the twinning elements for different types of twin [32, 112], one could infer that variant pair A:C (or B:D) has twin relationship of type I, A:B (or C:D) of type II twin, and A:D (or B:C) of compound twin.

Table 3.2 Twinning elements of commensurate 5M modulated martensite in $Ni_{50}Mn_{28}Ga_{22}$.

	Type I (A:C and B:D)	Type II (A:B and C:D)	Compound (A:D and B:C)
K_1	$(1\ \bar{2}\ \bar{5})$	$(1.0569\ \bar{2}\ \overline{4.7155})$	(1 0 5)
K_2	$(\overline{1.0569}\ \bar{2}\ 4.7155)$	$(\bar{1}\ \bar{2}\ 5)$	$(\bar{1}\ 0\ 5)$
η_1	$[\overline{5.2504}\ \bar{5}\ 0.9499]$	$[\bar{5}\ \bar{5}\ 1]$	$[\bar{5}\ 0\ 1]$
η_2	$[5\ \bar{5}\ \bar{1}]$	$[5.2504\ \bar{5}\ \overline{0.9499}]$	[5 0 1]
P	$(1\ \overline{0.0514}\ 5.2568)$	(1 0.0514 5.2568)	(0 1 0)
s	0.1387	0.1387	0.0074

Based upon the minimum shear criterion, the complete twinning elements (K_1-the twinning plane; η_1-the twinning direction; K_2-the reciprocal or conjugate twinning plane; η_2-the reciprocal or conjugate twinning direction; P-the plane of shear; s-the amount of shear) of the above three types of twins were unambiguously determined using a general method recently developed [33] and are displayed in Table 3.2. It is seen that type I twin (rational K_1 and η_2) and type II twin (rational K_2 and η_1) have the same magnitude of shear s, but K_1 and K_2, and η_1 and η_2 are interchanged. Therefore, type I twin and type II twin can be regarded as conjugate or reciprocal to each other [32]. Among the three types of twins, compound twin (rational K_1, K_2, η_1 and η_2) possesses the smallest twinning shear. Geometrically, all these twin relationships can be equivalently expressed by a minimum misorientation between two twinned variants. This minimum misorientation may be used as a simple criterion to judge

possible twinning relationships between two variants for post EBSD orientation analysis, *i.e.* ~86° around the $[501]_{5M}$ direction for type I twin, ~94° around the normal of the $(105)_{5M}$ plane for type II twin, and ~180° around the $[\bar{5}01]_{5M}$ direction or ~180° around the normal of the $(105)_{5M}$ plane for the compound twin.

3.1.5 Characters of twin interface planes

Because magnetic-field induced strains in Ni-Mn-Ga alloys are realized by the reorientation of martensite variants through interface motion, the crystallographic nature of the interface planes is of major significance for the efficiency of the magnetic shape memory effect. Here, the twin interfaces between neighbouring variants were further analyzed using the indirect two-trace method [113]. The Miller indices of individual twin interface planes were unambiguously determined from the orientation data of adjacent variants and the trace vectors of twin interfaces in the sample coordinate system. To achieve statistical reliability, five groups of twin interface normals were calculated and the mean values are shown in Table 3.3. For above three types of twins, the calculated interface planes are in coincidence with their respective twinning planes (K_1 plane) with a slight deviation, being close to $(1\bar{2}\bar{5})_{5M}$ for type I twin, $(1.0569\ \bar{2}\ \overline{4.7155})_{5M}$ for type II twin and $(105)_{5M}$ for compound twin. Therefore, all these three types of interfaces can be considered as coherent interfaces; hence they should have the highest mobility and reversibility as compared with the general incoherent high angle boundaries in polycrystalline materials.

Table 3.3 Mean values of twin interface normals calculated by indirect two-trace method [113] and expressed in the orthonormal crystal coordinate system and their deviations from the ideal interface plane normals.

Twin type	Variant pair	Twin interface normal	Deviation from related K_1 plane
Type I	A:C	{0.497546, -0.729415, -0.46947}	1.03° from $(1\bar{2}\bar{5})$
	B:D	{-0.471084, -0.726568, 0.500179}	1.07° from $(1\bar{2}\bar{5})$
Type II	A:B	{0.507753, -0.733658, -0.451589}	0.34° from $(1.0569\ \bar{2}\ \overline{4.7155})$

Compound	C:D	{-0.518242, -0.721797, 0.458731}	0.80° from (1.0569 $\bar{2}$ $\overline{4.7155}$)
	A:D	{0.709382, -0.010644, 0.704744}	0.63° from (105)
	B:C	{0.705740, -0.005253, -0.708451}	0.34° from (105)

According to the accurate orientation identification of the martensite microstructure (Fig. 3.3a), the bended thin lamellae are revealed as martensite variants connected by compound twin interfaces. Locally, a compound twin interface intersects its neighboring type I and type II twin interfaces. This morphological feature of bent lamellae with changed orientation could result from the self-accommodation of thin lamellae during martensitic transformation to reduce the transformation strain and minimize the resistance. However, such a configuration does not favor the global reorientation of variants through twin boundary movement under an actuating magnetic field, since compound twin interface represents a kind of interface pin. Moreover, the $(105)_{5M}$ plane that contains the $[010]_{5M}$ direction (*i.e.* the *b* axis - the easy magnetization direction) is the invariant twinning plane of compound twins. As two twin-related crystals are in mirror symmetry with respect to the twinning plane $(105)_{5M}$, their *b* axes are parallel to each other. Thus, it becomes almost impossible to trigger the reorientation of one crystal with respect to the other through the motion of the compound twin interface under a unidirectional actuating magnetic field, *i.e.* the compound twin interface is inert.

Clearly, the geometrical combination of the four differently oriented variants in the plate microstructure is not an optimal solution to the maximum shape memory effect. The existence of a large amount of compound twin interfaces could be considered as one of the major reasons for a high actuation stress required for these alloys [43, 96, 106]. In this connection, the compound twin interfaces should be eliminated to achieve a large strain output. Owing to the very small twinning shear of compound twins, the compound twin interfaces might be removed readily by detwinning via mechanical training, with the training force applied in the inverse twinning direction, *i.e.* $[5\ 0\bar{1}]_{5M}$ direction.

One can further conceive that, for the most ideal case, only two variants, with either type I twin or type II twin relationship, are left in the plate microstructure after

the complete detwinning of the compound twins. In such a circumstance, the shape memory process would be achieved by the detwinning or twinning of one variant with respect to the other variant. As the two types of twins have the same twinning shear, the intensity of the external actuating field would be the same for the two cases. The angle between the easy magnetization directions of the two variants is 86.04° in type I twin relation and 93.96° in type II relation. To obtain the maximum strain output under a minimum actuating field, the field should be applied in the easy magnetization direction of either of the two variants.

3.1.6 Orientation relationship between austenite and 5M martensite

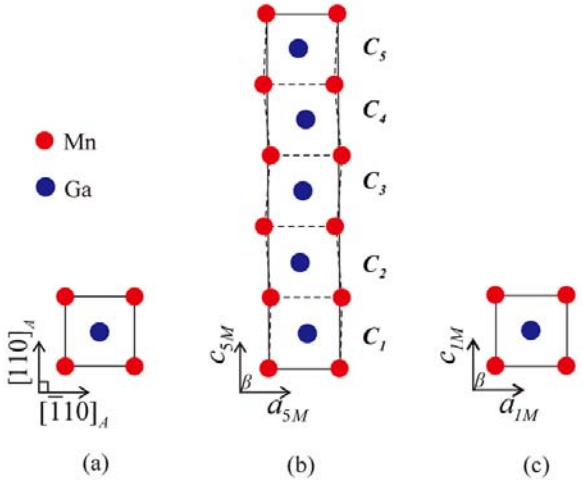

Fig. 3.5. Illustrations of (a) the unit cell of cubic austenite, (b) the supercell of monoclinic 5M modulated martensite consisting of five subcells (outlined by dash lines), and (c) the reduced average unit cell (ignoring the lattice modulation).

Fig. 3.5a and b illustrate the lattice correspondence between austenite and 5M martensite. The high-temperature austenite possesses a cubic $L2_1$ Heusler structure (*Fm-3m*, *No. 225*) with the lattice parameter a_A=5.84Å [21, 114]. The 5M martensite (a_{5M} =4.226Å, b_{5M} =5.581Å, c_{5M} =21.052Å and β=90.3°) has a monoclinic superstructure (*P2/m*, *No. 10*) and the supercell of 5M martensite can be decomposed into five consecutive subcells along the *c*-axis (denoted as C_1, C_2……C_5 in Fig. 3.5b). The monoclinic crystallographic axes of 5M martensite align along the

$[\bar{1}10]_A$ (a-axis), $[001]_A$ (b-axis) and $[110]_A$ (c-axis) directions of the cubic austenite. If we ignored the lattice modulation, the supercell could be further reduced into one unit cell with mean lattice constants $a_{1M} = a_{5M} = 4.226$ Å, $b_{1M} = b_{5M} = 5.581$ Å, $c_{1M} = c_{5M}/5 = 4.2104$ Å, and $\beta = 90.3°$, as shown in Fig 3.5c. Hereafter, we will refer to this average subcell of the 5M modulated martensite as the unit cell of a so-called "1M martensite", and denote the austenite, 1M martensite and 5M martensite by putting the symbols "A", "1M" and "5M" as the subscript in this section, respectively.

Since the martensitic transformation is diffusionless and realized by coordinate displacement of atoms, some specific ORs between the parent and product phases are required to minimize the lattice discontinuity across the phase boundary. In most cases, the determination of these ORs are rendered to find a plane and in-plane direction parallelism by making use of the coexistence of the retained parent austenite and the product martensite. However, for the present $Ni_{50}Mn_{28}Ga_{22}$ alloy, the martensitic transformation is complete at room temperature, *i.e.* no residual austenite. It is not possible to make a direct determination of the OR between the austenite and the martensite. Therefore, verifying the austenite orientations that are calculated from the orientations of the martensite variants induced from the same initial austenite under an assumed OR could be an alternative solution to deduce the transformation OR [108]. If the austenite orientations calculated from all individual martensite variants inherited from the same parent grain share a common orientation, the assumed OR could be the one that governs the martensitic transformation, and the resultant common orientation is the orientation of the initial austenite grain.

The austenite orientations (G_A^l) with respect to the sample coordinate system can be recalculated by the following equation expressed in matrix notation [108]:

$$G_A^l = G_M^k \cdot S_M^i \cdot T \cdot (S_A^j)^{-1} \tag{3.1}$$

where G_M^k represents the measured orientation of the kth martensite variant with respect to the sample coordinate system; T is the rotation matrix transforming the

orthonormal crystal coordinate system fixed to the monoclinic martensite lattice to the austenite lattice basis under the given OR; S_A^j (j = 1, 2, ..., 24) and S_M^i (i = 1, 2) are the respective cubic (austenite) and monoclinic (martensite) symmetry elements. When T is fixed, a total of 48 different austenite orientations may be generated from one martensite variant with Eq. (3.1) on account of the symmetry elements of cubic and monoclinic basis, but they are not all symmetrically independent and can be further incorporated into the physically distinct orientations.

By a survey of the literature, those widely addressed Bain [22], K-S [26], N-W[27, 28] and Pitsch [30] ORs are presumed as possible ORs between the parent austenite and the product martensite in the present work, as listed in Table 3.4. The assumed plane and in-plane direction parallelisms are firstly used to specify the ORs between austenite and 1M martensite.

Table 3.4 A selection of possible ORs between austenite and martensite. Note that the Miller indices of planes and in-plane directions for product martensite with monoclinic structure are referred to the average unit cell illustrated in Fig. 3.5c.

Transformation OR	Plane and in-plane direction parallelism
Bain relation	$(001)_A//(010)_{1M}$ & $[010]_A//[101]_{1M}$
K-S relation	$(111)_A//(011)_{1M}$ & $[10\bar{1}]_A//[\bar{1}\,\bar{1}\,1]_{1M}$
N-W relation	$(111)_A//(011)_{1M}$ & $[11\bar{2}]_A//[0\bar{1}\,1]_{1M}$
Pitsch relation	$(101)_A//(1\bar{2}\,\bar{1})_{1M}$ & $[10\bar{1}]_A//[\bar{1}\,\bar{1}\,1]_{1M}$

Based on the above considerations, we calculated the orientations of parent austenite from the measured orientations of locally adjacent four twin-related martensite variants, using the possible ORs listed in Table 3.4. Here, four twin-related variants in one broad plate were treated as a variant group. To achieve statistical significance, the variant orientation data measured from six different groups (denoted as *g1*, *g2*…… *g6*) were served as initial input data. For easy visualization, the calculated austenite orientations under a given OR were plotted in the {001} standard stereographic projection in the macroscopic sample coordinate frame.

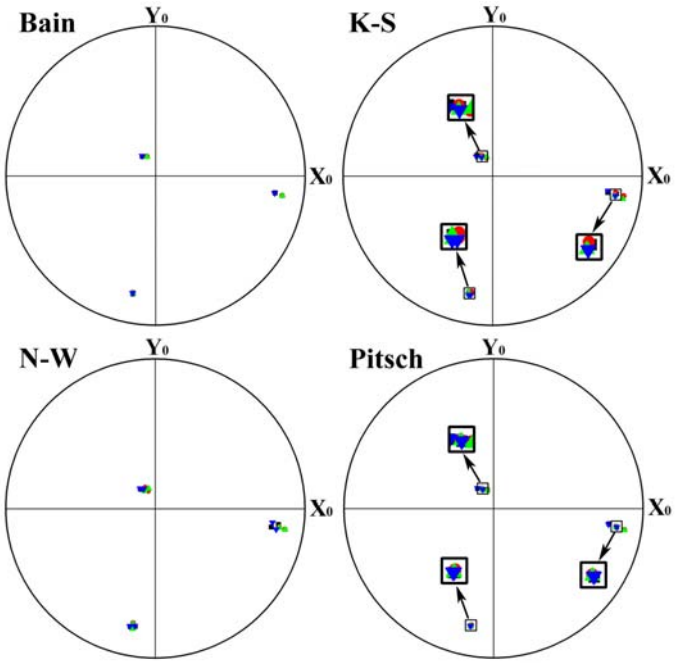

Fig. 3.6. {001} standard stereographic projections of austenite orientations in the macroscopic sample coordinate frame calculated from the four martensite variants in variant group *g1* under Bain, K-S, N-W and Pitsch relations, respectively. The common poles are enclosed in squares.

As an example, Fig. 3.6 displays the calculation results from variant group *g1*. In the figure, one austenite orientation is represented by three {001} poles. As there are 24 symmetry elements in cubic symmetry and 2 in monoclinic symmetry, 48 austenite orientations from each martensite variant can be expected, among which several are distinct and the others are equivalent to the distinct ones depending on the OR selected. As displayed in Fig. 3.6, there is one distinct austenite orientation calculated from one martensite variant under Bain relation, and two under K-S, N-W and Pitsch relations, respectively. If the assumed OR is true for the transformation, all the three {001} austenite poles from one martensite variant should correspond to those of the other three variants in the same variant group, *i.e.* the same named austenite poles from the four variants should overlap in the projection. It can be seen that K-S OR and Pitsch OR seem to give the smallest mismatch (dispersion). To quantify the mismatch for an assumed OR, the minimum misorientation angles between two calculated austenite orientations were estimated, as shown in Table 3.5. Indeed,

among all the selected variant groups, Pitsch OR represents the smallest deviation angle. Further examination on the atomic correspondence between the austenite and the 1M martensite under the Pitsch OR indicates that Pitsch OR may provide ideal lattice continuity if the crystal structure of the product martensite could be represented by the average unit cell. The respective planes, *i.e.* the $(101)_A$ and $(1\,\bar{2}\,\bar{1})_{1M}$, have the exactly same atomic stacking sequences with very close interplanar spacing and the consistent arrangements of the constituent atoms. Therefore, Pitsch OR, *i.e.* $(101)_A//(1\,\bar{2}\,\bar{1})_{1M}$ and $[10\,\bar{1}]_A//[\bar{1}\,\bar{1}\,1]_{1M}$ between austenite and 1M martensite, or $(101)_A//(1\,\bar{2}\,\bar{5})_{5M}$ and $[10\,\bar{1}]_A//[\bar{5}\,\bar{5}\,1]_{5M}$ if referred to 5M martensite, should be considered as the more favourable transformation OR.

Table 3.5 Minimum misorientation angles between the austenite orientations calculated from variant A and from other three variants in six variant groups under Bain, K-S, N-W and Pitsch OR.

Group No.	Variant pair	Bain (°)	K-S (°)	N-W (°)	Pitsch (°)
g1	A:B	3.45	0.75	2.09	0.75
	A:C	3.52	1.61	1.74	0.50
	A:D	0.44	1.58	2.44	0.25
g2	A:B	3.81	0.34	2.34	0.33
	A:C	3.30	1.89	1.86	0.66
	A:D	1.07	1.81	2.86	0.81
g3	A:B	3.33	0.66	1.80	0.66
	A:C	3.22	1.72	1.62	0.81
	A:D	0.41	1.90	2.66	0.20
g4	A:B	3.53	0.48	1.83	0.48
	A:C	3.42	1.44	1.50	0.70
	A:D	0.49	1.52	2.46	0.26
g5	A:B	3.20	0.79	1.81	0.79
	A:C	3.22	1.56	1.44	0.86
	A:D	0.84	1.38	2.38	0.40
g6	A:B	3.70	0.43	4.17	0.43
	A:C	3.66	1.90	3.94	0.36
	A:D	0.40	1.98	2.86	0.28

As the resultant martensite of the present material possesses a modulated crystal structure, the information on structural modulation should be taken into account to

evaluate the deviation from the ideal OR between two phases. The structural modulation can be considered as an atomic reshuffling in each subcell of the supercell with respect to the "averaged unit cell". Clearly, this modulation results in a certain angular deviations of the same indexed planes and directions in each subcell of 5M martensite with respect to those in the averaged unit cell. The angular deviations correspond to Pitsch OR due to structural modulation are shown in Fig. 3.7. It is seen that the angular deviation for both $(1\,\bar{2}\,\bar{1})_{1M}$ plane and $[\bar{1}\,\bar{1}\,1]_{1M}$ direction increases with the difference in the monoclinic angle between the "averaged unit cell" and each subcell. The structural modulation generates ~1-2.6° angular deviations for the corresponding plane and ~1-2.5° deviations for the in-plane direction in each subcell.

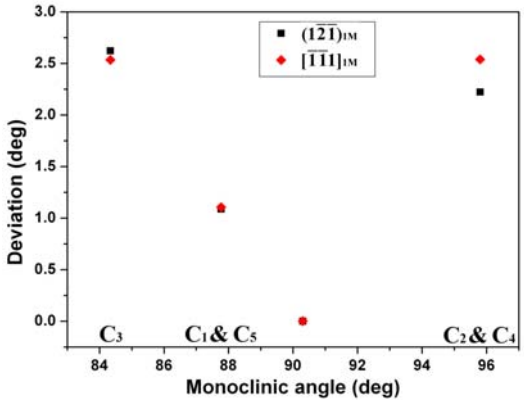

Fig. 3.7 Angular deviations of the same indexed $(1\,\bar{2}\,\bar{1})_{1M}$ and $[\bar{1}\,\bar{1}\,1]_{1M}$ in each subcell from those of the average unit cell.

Based on the determined Pitsch OR between the two phases, the theoretical number of martensite variants induced from the same austenite grain can be predicted. The possible orientations of martensite variants with respect to the sample coordinate system are given by the following equation:

$$G_M^k = G_A^l \cdot S_A^j \cdot T^{-1} \cdot (S_M^i) \tag{3.2}$$

Due to the cubic symmetry of the austenite and the monoclinic symmetry of the martensite, there are at most 24 martensite variants inherited from the same austenite grain under the Pitsch OR. As former EBSD analysis has revealed that only 4 variants appear in one variant group and they are twin-related one another, these 24 variants

can be divided into 6 groups. Thus, the formation of self-accommodated martensite in one initial austenite grain is realized firstly by combination of 4 twin-related variants in an individual group and then by combination of different groups over the entire grain. Such a configuration of the product microstructure should ensure a minimum lattice discontinuity between the parent austenite and the martensite.

3.1.7 Summary

The crystal structure, microstructural features, twin relationships of 5M martensite and phase transformation OR in a bulk polycrystalline $Ni_{50}Mn_{28}Ga_{22}$ alloy were investigated. The crystal structure analysis has shown that the martensite possesses a commensurate 5M modulated structure, the superlattice of which is composed of 5 subcells. The microstructure of the 5M martensite can be characterized by broad plates with alternatively distributed fine lamellar-shaped variants. The correct and accurate EBSD orientation indexing was made using the precise crystal structure information. From the microstructure reconstructed with the individually measured orientations, the four types of martensite variants A, B, C and D with distinct orientations were revealed. All the variants are twin related, *i.e.* the variant pair A and C (or B and D) are in type I twin relation, A and B (or C and D) in type II twin relation, and A and D (or B and C) in compound twin relation. Moreover, the twin interface planes were determined to be in coincidence with their respective twinning planes (K_1). Based on the local orientations of the individual martensite variants measured by EBSD, the orientations of the parent austenite were calculated using the assumed ORs between the cubic austenite and the monoclinic martensite. Considering the minimum misorientation angles between the calculated austenite orientations, the most favorable OR governing transformation from the austenite to 5M martensite was revealed to be the Pitsch relation with $(101)_A//(1\bar{2}\bar{5})_{5M}$ and $[10\bar{1}]_A//[\bar{5}\bar{5}1]_{5M}$ with no residual austenite. Under such an OR, at most 24 variants could be induced from the same austenite grain after the martensitic transformation.

3.2 7M Martensite

7M martensite, as the other kind of modulated martensite in Ni-Mn-Ga alloys, can generate much larger magnetic field induced strain (*i.e.* ~10%) than that of 5M martensite. So far, the crystal structure studies of these materials conducted by TEM have suffered from uncertainties in determining the number of subcells of modulated superstructure, *i.e. commensurate and incommensurate*, and consequently improper interpretations of orientation correlations of martensite variants. In this section, the microstructural and crystallographic characteristics of 7M martensite in a polycrystalline $Ni_{50}Mn_{30}Ga_{20}$ alloy were investigated by EBSD with the application of the correct incommensurate superstructure information of 7M martensite (7M(IC)). The orientation relationships of adjacent martensite variants and their twin interface characters in the incommensurate 7M martensite were unambiguously determined. With the accurate orientation measurement on inherited martensitic variants, the local orientations of parent austenite grains were predicted using four classical ORs for the martensitic transformation. Furthermore, a specific OR between austenite and 7M martensite was unambiguously determined by considering the magnitude of discontinuity between the lattices of the product and parent phases and the structural modulation of the incommensurate 7M modulated martensite.

3.2.1 Phase transformation temperatures and mechanical property

Polycrystalline Ni-Mn-Ga alloy with nominal composition of $Ni_{50}Mn_{30}Ga_{20}$ (at.%) was prepared. For the reduction of microcracks and porosity, the ingots were remelted and suction cast into a chilled copper. The actual composition was determined to be $Ni_{49.6}Mn_{30.4}Ga_{19.9}$ by energy dispersive X-ray spectrometry (EDS) measurements. The phase transformation temperatures were measured by differential scanning calorimetry (DSC). The martensitic transformation start temperature (M_s) and finish temperature ($M_{f)}$ were determined to be 88.7℃ and 78.3℃, and the reverse transformation start temperature (A_s) and finish temperature (A_f) were 87.7°C and

97.2°C, respectively.

The compressive stress-strain curves of the as-cast alloy and the suction-cast alloy are presented in Fig. 3.8. For the button without suction cast, the maximum compressive strength and compressive strain are 385MPa and 8.6%, respectively; while for the rod after suction casting, the maximum strength and strain reach the corresponding values of 705MPa and 10.1%, respectively. The compression strength and the deformation capacity of the suction cast alloy are increased by 83.1% and 17.4%; respectively, compared with those obtained by common casting. This could be attributed to the smaller grain size and the less microcracks and porosity in the as-suctioned rod than that in the as-cast button due to the faster cooling rate of suction-cast.

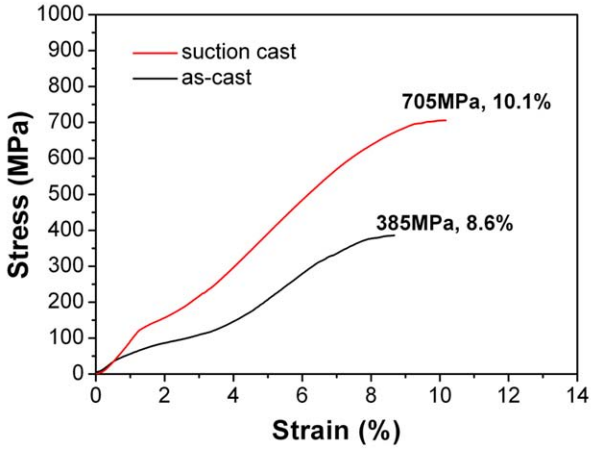

Fig 3.8 Compressive stress-strain curves of the as-cast and the as-suction alloys.

3.2.2 Crystal structure of 7M martensite

Fig. 3.9 displays the measured and recalculated powder X-ray diffraction (XRD) patterns of the $Ni_{50}Mn_{30}Ga_{20}$ suction-cast alloy at room temperature. The profile of the measured XRD pattern (Fig. 3.9a) is consistent with that reported by L. Righi *et al.* [75], suggesting that the alloy may have an incommensurate 7M modulated (7M(IC)) structure. The superlattice consists of 10 unit cells along the *c*-axis, belonging to the monoclinic space group P2/m (No.10). With the information of the atomic coordinates in the superlattice (as shown in Appendix II) [75], the measured XRD pattern was

then fitted using the Powder Cell software [109]. Accordingly, the lattice parameters were determined to be a_{7M} = 4.2651 Å, b_{7M} = 5.5114 Å, c_{7M} = 42.365 Å, and β = 93.27°. It is seen that the 7M martensite possesses much larger monoclinic angle than that of the 5M martensite (*e.g.* 90.3° for 5M martensite of $Ni_{50}Mn_{28}Ga_{22}$ alloy). It is noted that the incommensurate modulation breaks the ideal periodic $(5\bar{2})_2$ stacking sequence in the commensurate case, and the stacking arrangement can be referred to as $(4\bar{2}5\bar{2}4\bar{3})$ comprising a tenfold superstructure for a total of 20 layers of atoms [75]. As shown in Fig.3.9b, the recalculated peak positions resulting from the incommensurate superstructure model and the refined lattice constants are in good agreement with the measured ones. Generally, the easy magnetization axis in the 7M modulated martensite corresponds to the shorter axis of the distorted $L2_1$ austenitic unit cell, *i.e. b* axis of the 7M modulated superstructure. It should be remarked that the correct determination of the crystal structure of the alloy is of vital importance for the further EBSD measurements to analyze the crystallographic characteristics of modulated martensite, namely the orientation relationships between martensite variants and the crystallographic planes of twin interfaces.

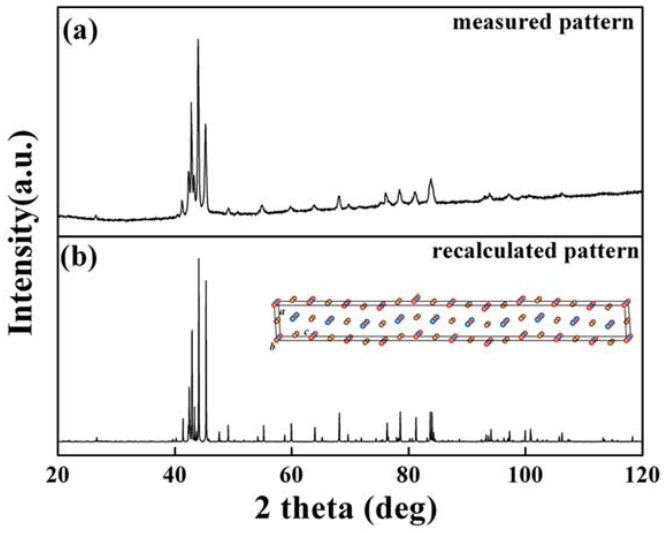

Fig. 3.9 XRD patterns of $Ni_{50}Mn_{30}Ga_{20}$ suction-cast alloy at room temperature: (a) measured; (b) recalculated using the incommensurate 7M modulation (7M(IC)) structure model. The inset shows the schematic illustration of superstructure.

3.2.3 Microstructure

Fig. 3.10a shows the typical backscattered electron (BSE) image of the $Ni_{50}Mn_{30}Ga_{20}$ suction-cast alloy taken at room temperature. It is clearly seen that the alloy presents the plate-like morphological features. The martensite plates are clustered in colonies in equiaxed shape and one colony or several colonies are located within an original austenite grain, which is different from the microstructure of 5M martensite. For the 5M martensite, the martensite colonies are in lamellar shape. Further TEM observations manifest that the 7M martensite plates possess stacking faults as internal sub-structures, as shown in Fig. 3.10b.

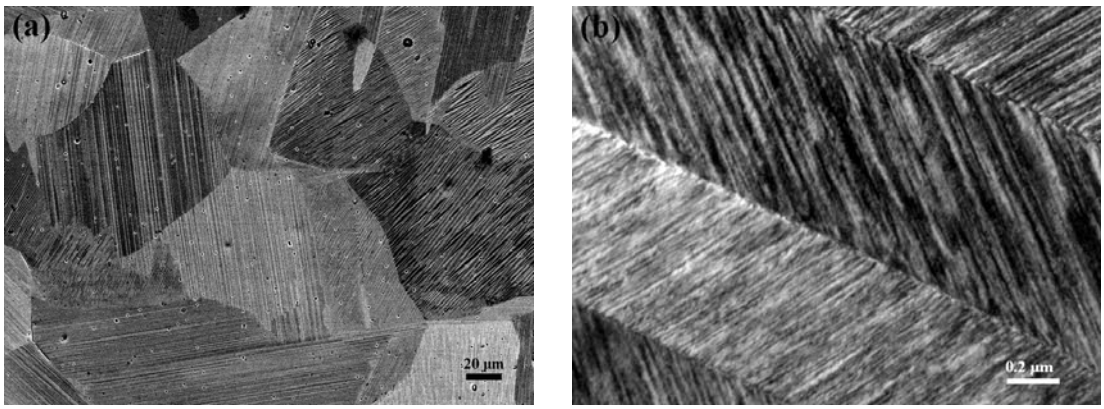

Fig. 3.10 (a) BSE image of the polycrystalline $Ni_{50}Mn_{30}Ga_{20}$ suction-cast alloy; (b) TEM dark-field image of the plates.

For the thorough analysis of the crystallographic characters of the 7M martensite variants, EBSD measurement was performed on a variant colony and the orientation map was reconstructed according to the incommensurate superstructure information illustrated before and is shown in Fig. 3.11a. It is seen that there are four kinds of variant (designated as A, B, C, and D in the figure) distributed alternately according to the different color that represents the different orientation. A Kikuchi line pattern acquired from one variant and its indexation with the incommensurate 7M crystal structure information are shown in Fig. 3.11b and c, respectively. The exact match of the recalculated pattern with the acquired pattern has confirmed the validity of the crystal structure information of the incommensurate 7M modulated martensite.

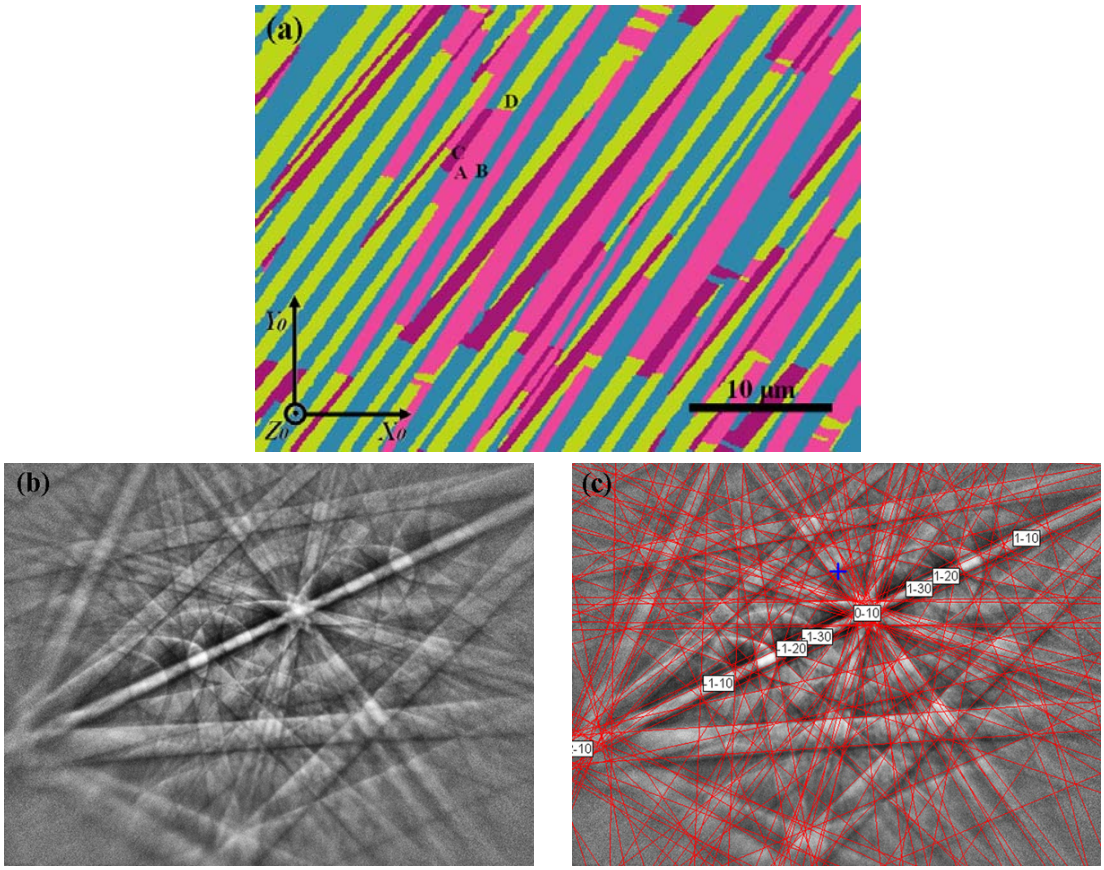

Fig. 3.11 (a) Orientation map of $Ni_{50}Mn_{30}Ga_{20}$ alloy taken at room temperature. Four types of martensite variants with different colours are designated as variant A, B, C, and D, respectively. The coordinate frame X_0-Y_0-Z_0 refers to the microscopic sample coordinate frame. (b) Kikuchi line pattern acquired from one of the variants; and (c) its indexation with the incommensurate 7M modulation (7M(IC)) structure model.

3.2.4 Determination of twin relationships and twin interfaces of 7M martensite

To determine the orientation relationships between two adjacent variants, the misorientations were calculated according to Eq.(2.4) using the orientation data of the corresponding variants in Fig. 3.11a and are shown in Table 3.6. For each variant pair, there exist two sets of misorientations (ω/**d**) owing to the monoclinic point symmetry. Among the two sets of misorientations, if taking possible experimental errors into account, there are only one 180° rotation between A and C (or B and D) and between A and B (or C and D), but two 180° rotations between A and D (or B and C) with their rotation axes perpendicular to each other. This suggests that all the variant pairs

are twin related according to the classical definition of twins [32, 112]. For variant pair A:C, the 180° rotation axis is close to the normal of the rational plane $(1\,\bar{2}\,\overline{10})_{7M}$ (with 0.41° deviation) of the monoclinic lattice, indicating that the two variants are reflection of each other with respect to this rational plane; while for the variant pair A:B, the 180° rotation axis is close to the rational direction $[\overline{10}\ \overline{10}\ 1]_{7M}$ (with 0.62° deviation), suggesting that the two variants have a rotation of 180° with each other about this rational direction. Following the definition of twinning [32, 112], one can deduce that variant pair A:C (or B:D) are type I twin; while A:B (or C:D) type II twin. As for the variant pair A:D (or B:C), one of the 180° rotation axes is close to the normal of the rational plane $(1\ 0\ 10)_{7M}$ (with 0.25° deviation) and the other is close to the rational direction $[\overline{10}\ \ 0\ \ 1]_{7M}$ (with 0.39° deviation), indicating that the variants A:D (or B:C) are compound twins to each other.

Table 3.6 Misorientation angles (ω) and rotation axes (**d**) among four types of variants (A, B, C, and D) in Fig. 3.11a, where the coordinates of rotation axes refer to an orthonormal crystal coordinate frame fixed to the monoclinic martensite lattice basis.

Variant pair	Misorientation angle ω [°]	Rotation axis, **d**		
		d_1	d_2	d_3
A:C	82.6319	-0.728809	-0.00337	-0.684708
	179.745	-0.452053	0.751082	0.481169
B:D	82.9978	-0.725021	-0.002634	-0.688722
	179.8	-0.456351	0.74897	0.480404
A:B	97.783	0.723592	0.003766	0.690218
	179.675	-0.520057	-0.65749	0.545204
C:D	96.5924	0.719889	-0.001061	0.694089
	179.909	0.518203	0.66528	-0.537465
A:D	179.219	0.724602	0.004305	0.689154
	179.507	-0.689145	-0.006812	0.724592
B:C	179.588	0.723417	0.003106	0.690404
	179.644	-0.690403	-0.003594	0.723416

According to the minimum shear criterion [33], the complete twinning elements

of the above three types of twins were unambiguously determined, as displayed in Table 3.7. It is seen that the variant pair A:C (or B:D) does possess the rational K_1 and η_2 (type I twin), A:B (or C:D) the rational η_1 and K_2 (type II twin), and A:D (or B:C) the rational K_1, η_1, K_2 and η_2 (compound twin). Among the three twin types, the compound twin type has the smallest twinning shear, while the other two types possess the twinning shear of the same order. Type I twin and type II twin are conjugate or reciprocal to each other with a common s, but K_1 and K_2, and η_1 and η_2 are interchanged [32], as the case of the 5M martensite. It is noted that the local variant number and the twin types of the 7M martensite are in consistent with those of 5M martensite, which should be due to the fact that both 7M and 5M martensite possess the monoclinic crystal structure. However, the twinning shear of the 7M martensite for each kind of twin is much larger than the corresponding value of the 5M martensite. This means that for the 7M martensite, larger force is needed for variant reorientation.

Table 3.7 Full twinning elements of $Ni_{50}Mn_{30}Ga_{20}$ 7M martensite twin variants. All the indices are expressed in the incommensurate 7M superlattice basis.

Elements	Type I (A:C / B:D)	Type II (A:B / C:D)	Compound (A:D / B:C)
K_1	$(1\ \bar{2}\ \overline{10})$	$(1.0621\ \bar{2}\ \overline{9.3785})$	(1 0 10)
K_2	$(\overline{1.0621}\ \bar{2}\ 9.3785)$	$(\bar{1}\ \bar{2}\ 10)$	$(\bar{1}\ 0\ 10)$
η_1	$[\overline{10.5541}\ \overline{10}\ 0.9446]$	$[\overline{10}\ \overline{10}\ 1]$	$[\overline{10}\ 0\ 1]$
η_2	$[10\ \overline{10}\ \bar{1}]$	$[10.5541\ \overline{10}\ \overline{0.9446}]$	[10 0 1]
P	$(1\ \overline{0.057}\ 10.5699)$	(1 0.057 10.5699)	(0 1 0)
s	0.2299	0.2299	0.0135

Since the magnetic-induced strains of Ni-Mn-Ga alloys are achieved by the reorientation of martensite variants through the motion of variant interfaces, insight into the crystallographic nature of these interface planes is surely of theoretical interest and practical significance. Here, by using the indirect two-trace method [113], the Miller indices of individual twin interface planes were unambiguously determined. To achieve statistical reliability, the results were collected from five groups of variants with different orientations, and the mean values are showed in

Table 3.8. It can be seen that for the three types of twin interfaces, the calculated interface planes are in coincidence with their respective twinning planes (K_1 plane) within reasonable deviation, being close to $\{1\ \bar{2}\ \overline{10}\}_{7M}$ for type I twin, $\{1.0621\ \bar{2}\ \overline{9.3785}\}_{7M}$ for type II twin and $\{1\ 0\ 10\}_{7M}$ for compound twin. Therefore, all these three types of twin interfaces can be considered as coherent interfaces. Obviously, individual movement of such interfaces would generate the smallest atomic mismatch, hence the highest mobility and reversibility as compared with other types of boundaries. This constitutes the positive necessities for the fast dynamic response to the actuating field in these materials.

Table 3.8 Mean values of twin interface normals in the orthonormal crystal coordinate frame calculated by indirect two-trace method [113] and their deviations from the related K_1 planes.

Twin type	Variant pair	Twin interface normal	Deviation from related K_1 plane
Type I	A:C	(0.46507, -0.75038, -0.46972)	1.09° deviation from $\{1\ \bar{2}\ \overline{10}\}$
	B:D	(0.46842, -0.74778, -0.47054)	1.14° deviation from $\{1\ \bar{2}\ \overline{10}\}$
Type II	A:B	(0.48386, -0.74886, -0.45287)	0.27° deviation from $\{1.0621\ \bar{2}\ \overline{9.3785}\}$
	C:D	(0.49928, -0.74497, -0.44242)	1.02° deviation from $\{1.0621\ \bar{2}\ \overline{9.3785}\}$
Compound	A:D	(0.72807, 0.01186, 0.68540)	0.73° deviation from {1 0 10}
	B:C	(0.72073, 0.02296, 0.69284)	1.35° deviation from {1 0 10}

3.2.5 Orientation relationship between austenite and 7M martensite

Fig. 3.12a and b illustrate the lattice correspondences between the cubic $L2_1$ structure of the austenite and the monoclinic structure of the incommensurate 7M modulated martensite. The high temperature austenite possesses the cubic (Heusler) crystal structure ($Fm\bar{3}m$, *No. 225*) with lattice parameter a_A = 5.84 Å [114]. The 7M modulated superstructure can be decomposed into ten consecutive subcells along the *c*-axis with the lattice parameters a_{7M} = 4.2651 Å, b_{7M} = 5.5114 Å, c_{7M} = 42.365 Å, and β = 93.27°. Herein, an individual subcell is visualized as a unit cell of one monoclinically distorted austenite lattice with the lattice basis vectors aligning

towards the [$\bar{1}$10], [001] and [110] directions of the cubic austenite lattice. Since there exists an inverse central symmetry in the 7M superlattice (Fig. 3.12b) [75], only five subcells are unique with distinct cell constants (denoted as C_1, C_2, C_3, C_4 and C_5) and the rest of them could be generated by the inversion operation. If we ignore the lattice modulation, the tenfold supercell can be specified by one monoclinic subcell with mean lattice constants $a_{1M} = a_{7M} = 4.2651$ Å, $b_{1M} = b_{7M} = 5.5114$ Å, $c_{1M} = c_{7M}/10 = 4.2365$ Å, and $\beta = 93.27°$, as shown in Fig. 3.12c. Hereafter, we will refer to this average subcell of the incommensurate 7M modulated martensite as the unit cell of a so-called "1M martensite", and denote the austenite, 1M martensite and 7M martensite by putting "A", "1M" and "7M" in the subscript in this section, respectively.

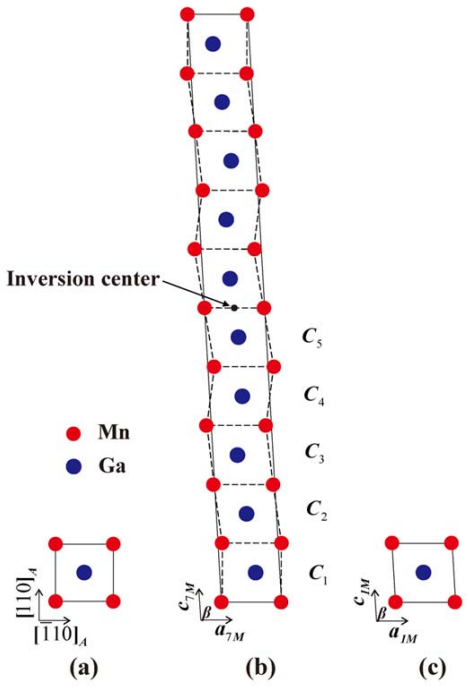

Fig. 3.12 Illustrations of (a) the unit cell of the cubic austenite; (b) the incommensurate superstructure of monoclinic 7M martensite comprising of ten subcells (outlined by dashed lines), five distinct subcells are denoted as C_1, C_2, C_3, C_4 and C_5; (c) the average unit cell of 1M martensite (ignoring the lattice modulation).

Since the martensitic transformation is complete at room temperature for $Ni_{50}Mn_{30}Ga_{20}$ alloy, the orientation relationship (OR) between austenite and 7M

martensite was determined by the indirect method, as the case of the 5M martensite. The classical Bain [22], K-S [26], N-W[27, 28] and Pitsch [30] ORs listed in Table 3.4 are presumed as possible ORs between the parent austenite and the product martensite. The assumed plane and in-plane direction parallelisms are firstly used to specify the ORs between the austenite and the 1M martensite. Based on the above considerations, the orientations of the austenite were calculated according to Eq. (3.1) by using the measured orientations of inherited martensite variants. To achieve statistical significance, the EBSD orientation data of seven groups of martensite variants (numbered as *g1*, *g2*, …, *g7*), were measured from different colonies and served as initial input data and the results were presented in the {001} standard stereographic projection of the cubic austenite in the macroscopic sample coordinate frame. As an example, Fig. 3.13 displays the three {001} austenite poles calculated from the respective martensite variants A, B, C and D from the same variant group *g1*.

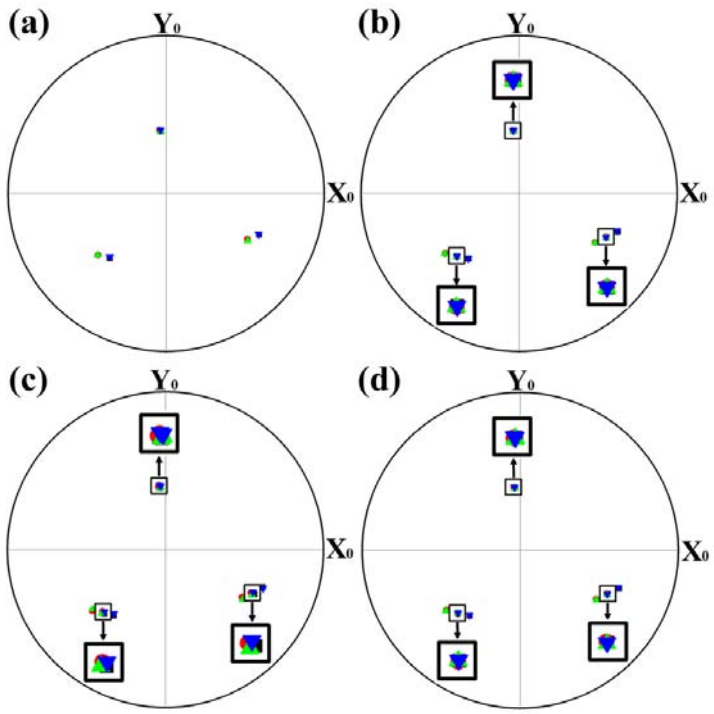

Fig. 3.13 {001} standard stereographic projections of austenite calculated from the martensite variants A (■), B (●), C (▲) and D (▼) in variant group g1 under (a) Bain, (b) K-S, (c) N-W and (d) Pitsch relations, respectively, in the macroscopic sample coordinate frame The common austenite orientations are enclosed in the open squares.

It is seen that each martensite variant is related to one austenite orientation under Bain relation (Fig. 3.13a), and two austenite orientations under K-S, N-W and Pitsch relations (Fig 3.13b-d), respectively. It is noted that the K-S and Pitsch ORs both give the smallest mismatch (dispersion) among the respective {001} poles for the common austenite orientation, as zoomed in the open squares in Fig. 3.13. To quantify the mismatch for the assumed ORs, the minimum misorientation angles between austenite orientations calculated from each martensite pair were estimated, as shown in Table 3.9. Indeed, among all the selected variant groups, both K-S and Pitsch ORs deliver the smallest deviation angle and there is almost no difference in the resultant austenite orientations, suggesting that they could be considered as two possible transformation ORs. This result is different from that of the 5M martensite, where the Pitch OR is favorable without any ambiguity.

Table 3.9 Minimum misorientation angles between austenite orientations calculated from martensitic variant pairs (A:B, A:C and A:D) in seven variant groups under Bain, K-S, N-W and Pitsch relations.

Group No.	Variant pair	Bain (°)	K-S (°)	N-W (°)	Pitsch (°)
g1	A:B	6.68	0.38	2.05	0.39
	A:C	6.78	0.33	1.38	0.30
	A:D	0.72	0.30	1.74	0.21
g2	A:B	7.47	1.14	2.31	1.14
	A:C	7.39	1.85	2.51	1.52
	A:D	0.35	0.60	1.43	0.32
g3	A:B	6.46	0.27	2.00	0.27
	A:C	6.71	0.89	1.54	0.57
	A:D	0.47	0.81	1.50	0.49
g4	A:B	7.38	1.30	3.18	1.27
	A:C	7.81	1.41	2.49	1.31
	A:D	1.13	1.12	1.98	1.03
g5	A:B	6.43	0.27	1.80	0.27
	A:C	6.43	0.72	1.22	0.42
	A:D	0.83	0.89	1.89	0.53
g6	A:B	6.13	0.89	1.09	0.89
	A:C	5.52	1.50	1.02	1.36
	A:D	0.58	1.09	1.15	0.93
g7	A:B	6.69	0.24	1.89	0.25

A:C	6.69	0.61	1.38	0.64
A:D	1.36	0.81	2.38	0.80

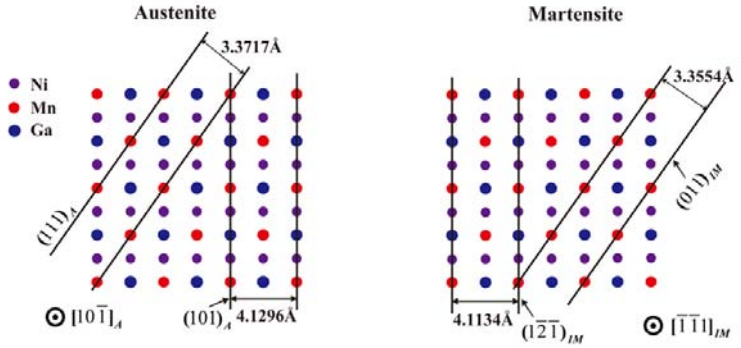

Fig 3.14 Schematic stacking sequences of the respective planes in austenite and 1M martensite viewed along $[1\,0\,\bar{1}]_A$ and $[\bar{1}\,\bar{1}\,1]_{1M}$.

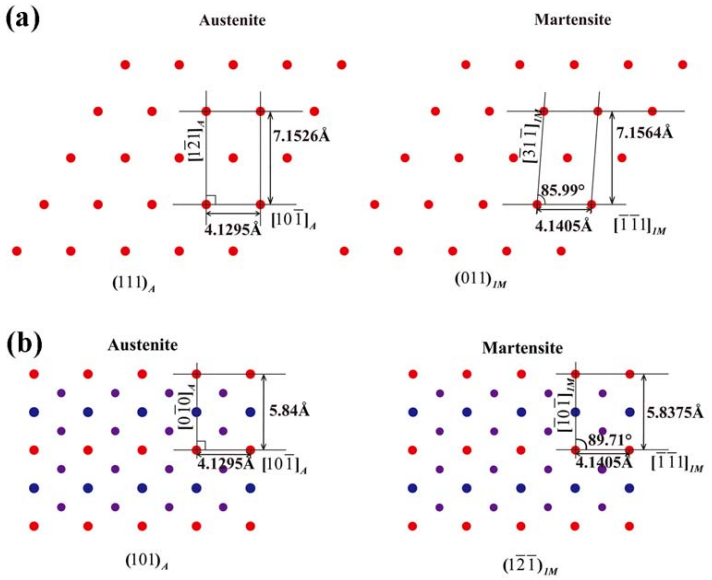

Fig. 3.15 Atomic correspondences of respective planes in austenite and 1M martensite under (a) K-S relation with $(111)_A//(011)_{1M}$ and $[10\,\bar{1}]_A//[\bar{1}\,\bar{1}\,1]_{1M}$ and (b) Pitsch relation with $(101)_A//(1\,\bar{2}\,\bar{1})_{1M}$ and $[10\,\bar{1}]_A//[\bar{1}\,\bar{1}\,1]_{1M}$.

Further examination on the atomic correspondence between the austenite and the 1M martensite under the K-S and Pitsch ORs indicates that these two ORs may provide ideal lattice continuity if the crystal structure of the product martensite could be represented by the average unit cell. As illustrated in Fig. 3.14, the respective planes in the austenite and 1M martensite, *i.e.* the $(111)_A$ and $(011)_{1M}$ (K-S OR) and

the $(101)_A$ and $(1\bar{2}\bar{1})_{1M}$ (Pitsch OR), have the exactly the same atomic stacking sequences with very close interplanar spacing. Moreover, the arrangements of the constituent atoms in the respective planes are also consistent in the two phases, as shown in Fig. 3.15. Such a good match between the lattices of the austenite and the 1M martensite suggests that the K-S and Pitsch ORs may be advantageous for the structure change during the martensitic transformation, as compared with the Bain and N-W ORs.

Unlike the situation of 5M martensite in $Ni_{50}Mn_{28}Ga_{22}$ alloy, the minimum misorientation results did not indicate a unique OR between the austenite and the 7M martensite. There appears almost no difference in the resultant austenite orientations under the assumed K-S and Pitsch ORs. To identify the most favorable transformation OR, it is essential to consider the lattice deformation during the transformation process from the viewpoint of the transformation energy. Fig. 3.16a and b illustrate the lattice deformation that transforms the austenite lattice to the 1M martensite lattice under the K-S and Pitsch ORs, respectively. The lattice deformation could be decomposed into the dilatation or contraction that causes volume change and the shear that gives rise to shape change but no volume change. In the case of the K-S OR, the elongation or contraction is assigned in the $[111]_A$, $[1\bar{2}1]_A$ and $[10\bar{1}]_A$ and the simple shear in the $(111)_A$ along $[\bar{1}01]_A$, in $(1\bar{2}1)_A$ along $[10\bar{1}]_A$ and in $(10\bar{1})_A$ along $[1\bar{2}1]_A$. For the Pitsch OR, the elongation or contraction is referred to the $[101]_A$, $[0\bar{1}0]_A$ and $[10\bar{1}]_A$ and the simple shear to the $(101)_A$ along $[\bar{1}01]_A$, to the $(0\bar{1}0)_A$ along $[10\bar{1}]_A$ and to the $(10\bar{1})_A$ along $[0\bar{1}0]_A$. The deformation amounts of all the components under the two ORs are given in Table 3.10.

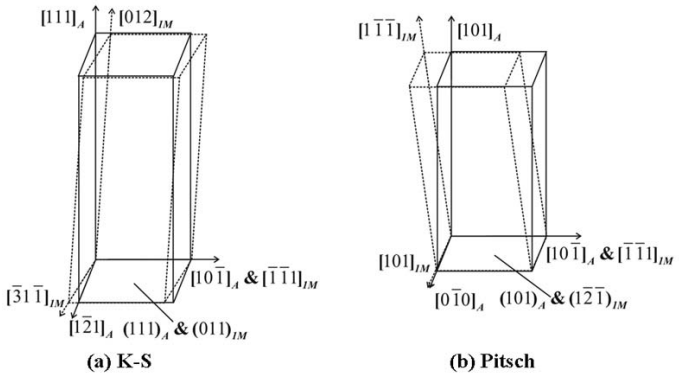

Fig.3.16 Illustration of lattice deformation to achieve the transformation from austenite to 1M martensite under (a) K-S OR and (b) Pitsch OR. The solid line represents the unit cell of austenite and the dashed line represents the average unit cell of 1M martensite.

Table 3.10 Components of lattice deformation for austenite to 1M martensite transformation under K-S OR and Pitsch OR.

K-S		Pitsch	
Dilation in $[111]_A$	-0.4834%	Dilation in $[101]_A$	-0.3923%
Dilation in $[1\,\bar{2}\,1]_A$	0.0531%	Dilation in $[0\,\bar{1}\,0]_A$	-0.0428%
Dilation in $[10\,\bar{1}\,]_A$	0.2664%	Dilation in $[10\,\bar{1}\,]_A$	0.2664%
Shear in $(111)_A\,[\,\bar{1}\,01]_A$	0.0701	Shear in $(101)_A\,[\,\bar{1}\,01]_A$	0.0051
Shear in $(1\,\bar{2}\,1)_A\,[10\,\bar{1}\,]_A$	0.0910	Shear in $(0\,\bar{1}\,0)_A\,[10\,\bar{1}\,]_A$	0.1149
Shear in $(10\,\bar{1}\,)_A\,[1\,\bar{2}\,1]_A$	0.0018	Shear in $(10\,\bar{1}\,)_A\,[0\,\bar{1}\,0]_A$	0.0045

It is seen from Table 3.10 that the deformation components that represent the discontinuity between the lattices of austenite and 1M martensite under the K-S and Pitsch ORs are not the same. As compared to the K-S OR, the Pitsch OR involves a relatively small lattice discontinuity (only the last 2 shear components in Table 3.10 are slightly elevated) for the austenite to 1M martensite transformation. Considering that an elongation or contraction requires volume change but a simple shear does not, the deformation by a simple shear may occur more easily. In this sense, the Pistch OR has somewhat energetically advantageous over that of the K-S OR for the austenite to 1M martensite transformation.

Furthermore, the information on structural modulation should be exploited to discriminate the energetically more favorable OR. For the incommensurate 7M

modulation, the tenfold superstructure can be produced in such a way that a set of ten consecutive average unit cells of the 1M martensite are sheared into the corresponding waved subcells of the 7M martensite by a monoclinic angle. Certainly, the same indexed planes and directions – expressed respectively in the 5 distinct subcells of the 7M martensite and in the average unit cell of the 1M martensite - exist somewhat angular deviations between them, as shown in Fig. 3.17. It is seen that the angular deviations both for plane (Fig. 3.17a) and in-plane direction (Fig. 3.17b) increase with the increased difference in monoclinic angle between the average unit cell of the 1M martensite and each individual subcell of the 7M martensite. Obviously, the K-S and Pitsch ORs differ from each other in the plane deviation as the $[10\,\bar{1}]_A//[\bar{1}\,\bar{1}\,1]_{1M}$ direction parallelism holds for the two ORs. As shown in Fig. 3.17a, the K-S OR ($(011)_{1M}$) possesses larger deviation than that of the Pitsch OR ($(1\,\bar{2}\,\bar{1})_{1M}$), which means that the K-S OR requires larger atomic reshuffling to achieve the structural modulation. This result may further confirm that the Pitsch OR, *i.e.* $(101)_A//[1\,\bar{2}\,\bar{1}]_{1M}$ and $[10\,\bar{1}]_A//[\bar{1}\,\bar{1}\,1]_{1M}$ between the austenite and the 1M martensite, or $(101)_A//[1\,\bar{2}\,\bar{10}]_{7M}$ and $[10\,\bar{1}]_A//[\bar{10}\,\bar{10}\,1]_{7M}$ if referred to the 7M martensite, is more energetically favorable than the K-S OR for the martensitic transformation.

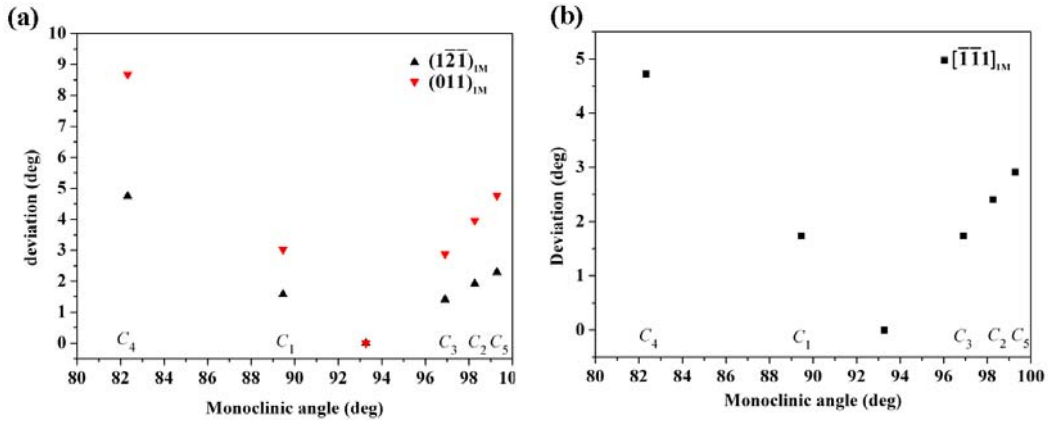

Fig 3.17 Angular deviations of the same indexed (a) $(1\,\bar{2}\,\bar{1})_{1M}$ (Pitsch OR) and $(011)_{1M}$ (K-S OR) and (b) $[\bar{1}\,\bar{1}\,1]_{1M}$ in 5 subcells (C_1, C_2, C_3, C_4 and C_5) with distinct monoclinic angle from those of the average unit cell.

Once an assumed OR is proved to be valid for the martensitic transformation, we

can predict the possible number of martensite variants within one original austenite grain according to Eq. (3.3). Because of the cubic symmetry of austenite and the monoclinic symmetry of the 7M martensite, there are at most 24 physically distinct martensite variants inherited from the same austenite grain under the Pitsch OR. As the EBSD analysis has revealed that only 4 variants appear in each variant colony (Fig. 3.11a) and they are twin-related one another, these 24 variants can be divided into 6 groups. Here, we may envisage that the formation of self-accommodated martensite variants in one initial austenite grain is realized firstly by combination of 4 twin-related variants in an individual group and then by combination of different groups over the entire grain, ensuring the minimum transformation strain and hence the lowest transformation energy consumed.

3.2.6 Summary

It has been demonstrated that the EBSD technique can be used as an advanced tool for unambiguously determining the orientation relationships of martensite variants and the crystallographic characteristics of twin interfaces for materials having modulated superstructure. Detailed analyses on the incommensurate 7M martensite of $Ni_{50}Mn_{30}Ga_{20}$ alloy showed that there exist four types of twin-related martensite variants (A, B, C, and D) that are alternately distributed. All the pairs of variants can be categorized into three twinning modes: variants A and C (or B and D) are in type I twin relation, variants A and B (or C and D) in type II twin relation and variants A and D (or B and C) in compound twin relation. All the twin interfaces are in coincidence with the respective twinning plane (K_1). Based on the local orientations of individual martensite variants measured by EBSD system, the orientations of the parent austenite were evaluated using the assumed ORs. By a detailed crystallographic analysis, the energetically favorable OR governing the austenite to incommensurate 7M martensite transformation was revealed to be the Pitsch relation with $(101)_A//(1\bar{2}\,\overline{10})_{7M}$ and $[10\,\bar{1}\,]_A//[\,\overline{10}\,\overline{10}\,1]_{7M}$. Under this determined OR, at most 24 physically distinct martensite variants may be resulted from an initial austenite grain during the

martensitic transformation. Notably, in the present work, the first attempt has been made to resolve the ambiguity of the geometrically favorable ORs by examining the lattice discontinuity caused by the phase transformation and the structural modulation. Such an approach to determine the OR from measured orientations of martensite variants - irrespective of the presence of retained austenite - can be easily adapted to various martensitic transformations that produce martensite with modulated superstructure.

3.3 Non-modulated martensite

NM martensite only exhibits a negligible magnetic shape memory strain, however, it is reported that NM martensitic alloys possess better mechanical properties than modulated martensite and some of them have good magnetocaloric effect due to the co-occurrence of the magneto-structural transition. By proper composition modification to obtain the higher martensitic transformation temperatures, NM martensitic alloys also display the potential as high-temperature shape memory alloys. In this section, the non-modulated $Ni_{54}Mn_{24}Ga_{22}$ alloys were prepared by arc-melting and suction-cast. The grain sizes were refined through suction-cast, making improvements on the mechanical properties. The morphology and the crystallographic features were further analyzed by electron backscatter diffraction (EBSD) and crystallographic calculation.

3.3.1 Phase transformation temperatures and crystal structure

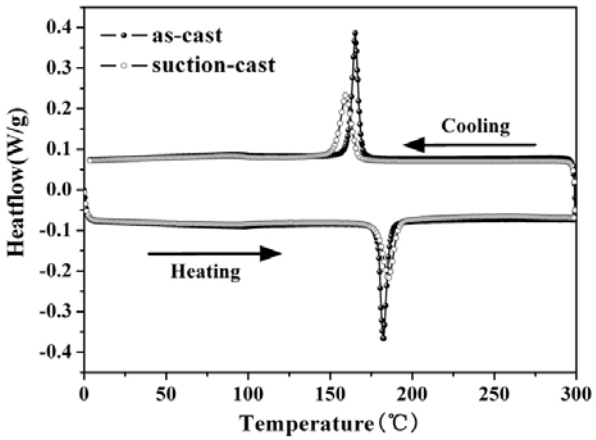

Fig. 3.18 DSC curve of the as-cast alloy and the as-suctioned $Ni_{54}Mn_{24}Ga_{22}$ alloy

Fig. 3.18 shows the measured DSC curves of the as-cast alloy and the as-suctioned alloy. For the as-cast alloy, the martensitic transformation starting temperature (M_s) and finishing temperature (M_f) are determined to be 168°C and 161°C, and the reverse transformation starting temperature (A_s) and finishing temperature (A_f) are 179°C and 187°C, respectively. The transformation temperature

hysteresis (A_f - M_s) is 19°C. While for the as-suctioned alloy, the corresponding martensitic transformation temperatures are 166°C, 153°C, 178°C and 192°C. The transformation temperature hysteresis is 26°C. The difference in martensitic transformation temperatures should be attributed to the higher cooling rate for the preparation of suction-cast alloy, which results in the higher density of lattice defects, like dislocations and grain boundaries [115]. These lattice defects increase the resistance of austenite-martensite interface motion and thus cause the decrease of the transformation temperature and larger transformation hysteresis.

The powder X-ray diffraction patterns measured at room temperature in Fig. 3.19 demonstrate that both the as-cast and the suction-cast alloys possess single non-modulated martensite with tetragonal crystal structure (space group of *I4/mmm* (No.139) [69]). The patterns can be indexed using this structure data. Obviously, suction-cast did not change crystal structure of the alloys. By comparison, the two patterns have the identical peak positions, thus the same lattice constants, *i.e.* a_{Tet}=b_{Tet}= 3.853 Å and c_{Tet}=6.625 Å.

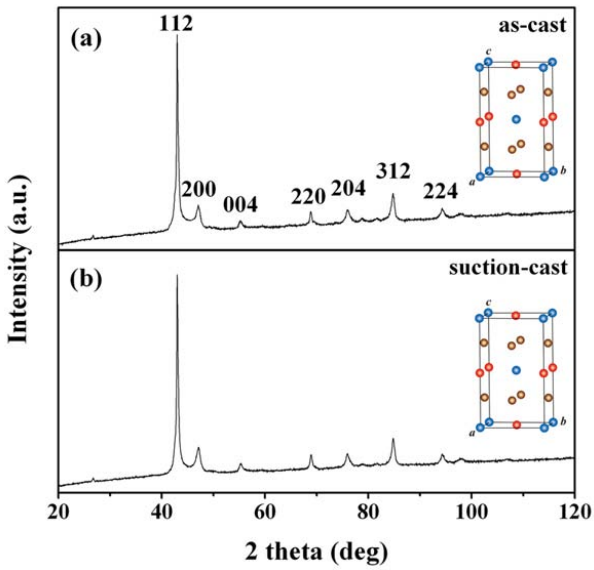

Fig. 3.19 Powder X-ray diffraction patterns measured at room temperature. (a) as-cast alloy; (b) suction-cast alloy. The inset shows the illustrations of the crystal structure.

3.3.2 Compressive properties

The compressive stress-strain curves of the as-cast alloy and the as-suctioned alloy are shown in Fig. 3.20. For the as-cast button, the maximum compressive strength and compressive strain are 670MPa and 8.5%, respectively. However, for the as-suctioned rod, the corresponding values are 990MPa and 18%, respectively. Obviously, the better mechanical properties can be achieved through suction-cast. This could be attributed to the relatively small grain size, less microcracks and porosity in the as-suctioned rod than those in the as-cast button.

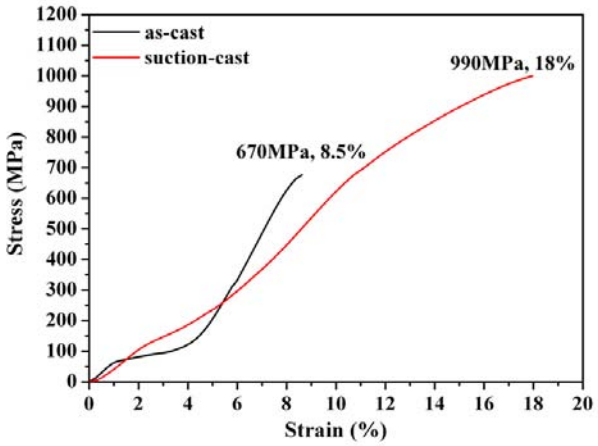

Fig. 3.20 Compressive stress-strain curves of as-cast alloy and as-suctioned alloy

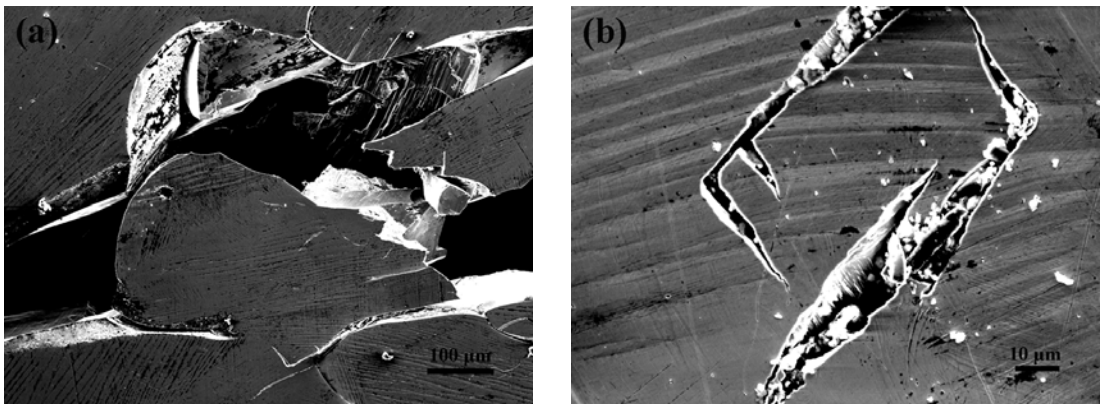

Fig. 3.21 Fractured surface after uniaxial compressive loading; (a) fracture along the grain boundaries; (b) fracture inside the martensite plates.

Fig. 3.21 shows the secondary electron images of the fractured surface after uniaxial compressive loading of the suction-cast rod. It can be seen in Fig.3.21a that

the fractures initiate mainly along the austenite grain boundaries, *i.e.* intergranular fracture. The brittle intergranular fracture phenomenon indicates the weak connection of the neighboring grain. It is also found that some cracks appear among the martensite plates, as shown in Fig.3.21b, suggesting that the cracks can also nucleate and propagate inside the martensite plates, leading to intragranular fracture.

3.3.3 Microstructure

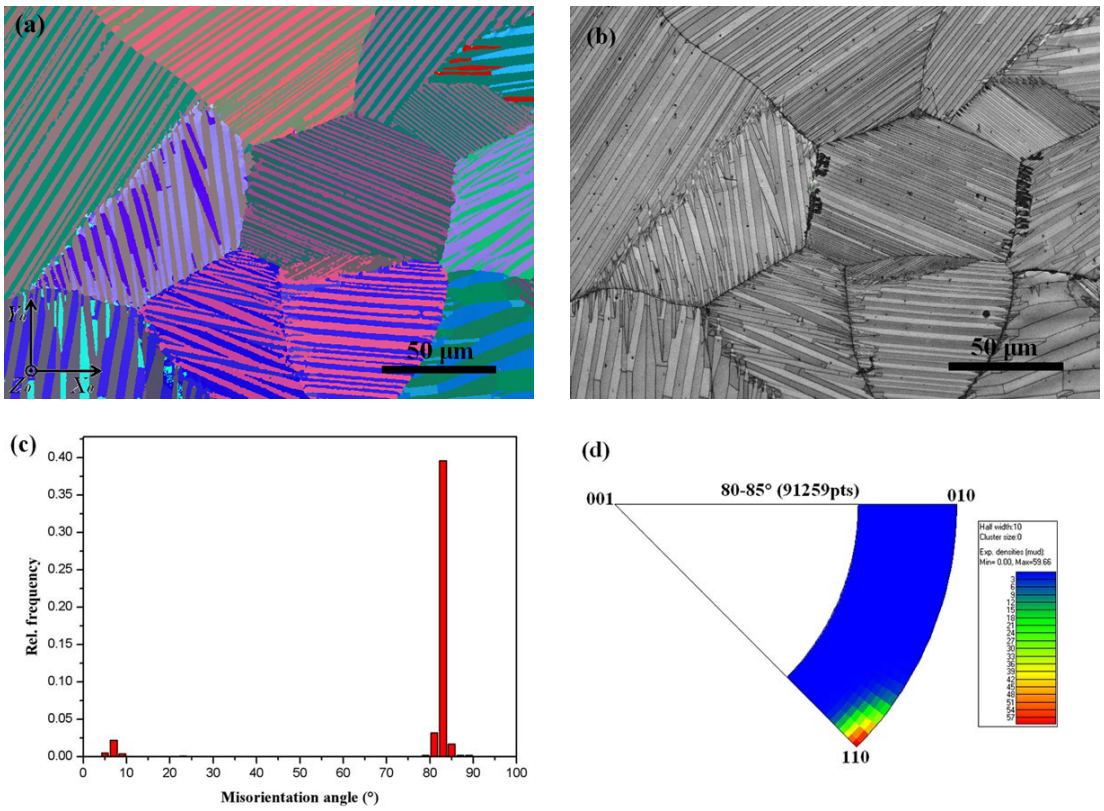

Fig.3.22 (a) Orientation micrograph of $Ni_{54}Mn_{24}Ga_{22}$ suction-cast alloy; (b) band contrast image; (c) misorientation angle distribution covering the measured region; (d) distribution of the corresponding rotation axes with misorientation angle of 80°-85°. The coordinate frame (X_0-Y_0-Z_0) refers to the macroscopic sample coordinate frame.

Fig. 3.22 displays the EBSD measurement results of the suction-cast alloy taken at the room temperature. In the orientation map in Fig. 3.22a, the plates are colored according to their orientation. It is seen that some plates are straight, while others are bent with slight orientation variation. Fig. 3.22b displays the band contrast image of

the same area and the orientation difference in plates is outlined by the contrast change. It is noted in Fig. 3.22b that there exist intra-plate boundaries corresponding to bent plate. Fig. 3.22c presents the corresponding minimum misorientation angles distribution covering the abovementioned orientation micrograph. It is shown that the misorientation angles of 80°~85° have the highest frequency, which corresponds to the misorientation angles between neighboring plates. There also exist a certain misorientation angles with 5~9°, which are corresponding to the bent plates connecting by intra-plate boundaries. Fig. 3.22d displays the distribution of the rotation axes with misorientation angle of 80°-85° in the asymmetrical triangle of the tetragonal system and the dominant rotation axes are around $<110>_{Tet}$. Here, one can see that in this alloy, the main orientation relationship between neighboring plates is of 80°-85° rotation around the $<110>_{Tet}$.

Further high magnification SEM observation manifests that there are four types of martensite plates (denoted as P1, P2, P3 and P4) in a martensite colony and the NM plates are composed of thin lamellae, as shown in Fig. 3.23. The fine lamellae appear in pairs, where one is thicker and the other is thinner. Thus, in a martensite colony, one can always find eight orientation variants. As the thickness of the fine lamellae is of tens of nanometer, it is beyond the resolution of the present automated orientation EBSD measurement. For the automatically acquired Kikuchi line patterns, only the ones from the thicker lamellae can be indexed. Thus, the auto orientation map was constructed with the orientation data from the thicker lamellae. To identify the orientation of the thinner lamellae, their Kikuchi patterns were manually acquired. For the manually acquired patterns, there are always bands from the neighboring thicker lamellae. The bands from the thinner lamellae in the mixed patterns were identified by comparing the individual bands in the mixed pattern with those from the thicker lamellae and then manually indexed to obtain the orientation information of the thinner lamellae.

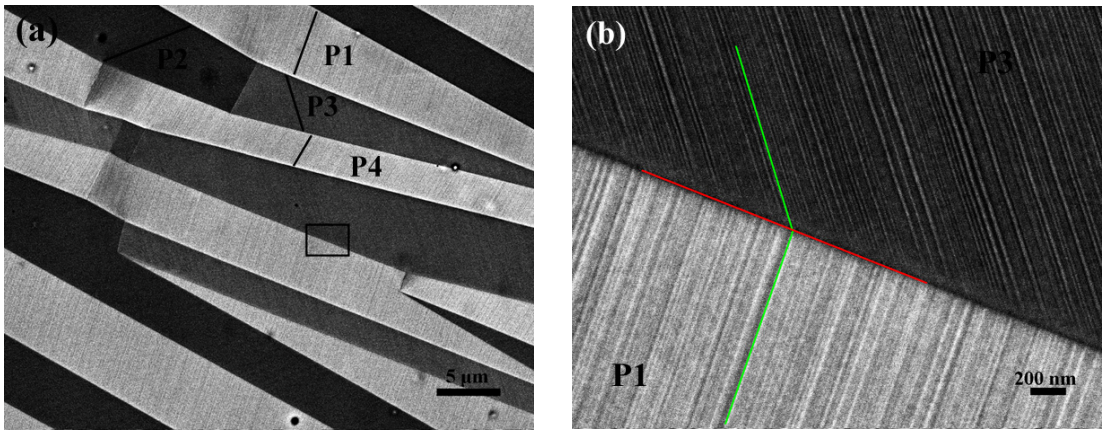

Fig. 3.23 (a) BSE image obtained in a martensite colony; four kinds of plates are numbered as P1, P2, P3, P4; (b) Zoomed image of the squared region showing the paired fine lamellae in the martensite plates. The inter-plate and inter-lamellar interfaces are marked with red and green lines, respectively.

For the paired fine lamellae in each plate, they were found to be compound twin related according to the misorientation calculations. An example of the misorientation calculation results corresponding to two fine lamellae in plate P1 was given in Table 3.11. It is seen that there are two sets of ~180° rotation and the corresponding rotation axes are perpendicular to each other, indicating that the two variants are twin-related. One ~180° rotation axis is near the normal of $\{112\}_{Tet}$ with 0.40° deviation and the other is near $<11\ \bar{1}>_{Tet}$ with 0.32° deviation. The twinning elements are unambiguously determined according to the minimum shear criterion and displayed as follows:

$K_1 = \{112\}_{Tet}$; $K_2 = \{11\ \bar{2}\}_{Tet}$; $\eta_1 = <11\ \bar{1}>_{Tet}$; $\eta_2 = <111>_{Tet}$; $P = \{110\}_{Tet}$; $s = 0.393$.

Table 3.11 Misorientation calculation results of the two fine lamellae in plate P1 expressed in the orthonormal basis.

Misorientation	Rotation axes		
angle ω (°)	***d1***	***d2***	***d3***
79.48	-0.705085	0.709088	-0.007046
100.53	0.711234	-0.702951	0.002353
113.69	-0.763601	0.002162	0.645685
114.56	0.002151	0.759855	-0.650089
126.09	0.005053	-0.862696	-0.505697

126.42	0.861443	0.005046	0.50783
179.48	-0.453318	-0.450759	0.768973
179.79	-0.540557	-0.546926	-0.639273

3.3.4 Determination of inter-plate and inter-lamellar interface

The interfaces between the neighboring plates (marked as red line in Fig.3.23b) were determined using the indirect two-trace method [113]. Table 3.12 shows the calculated indices of 14 inter-plate interfaces expressed in the orthonormal basis. The mean interface indices were determined to be {0.565129, -0.499292, 0.656763}. In the tetragonal basis, the mean value of the determined inter-plate interface plane is {1, -0.883501, 1.998241}$_{\mathrm{Tet}}$, which is 3.15° from the $\{1\,\bar{1}\,2\}_{\mathrm{Tet}}$ plane, indicating that the inter-plate interface is not fully coherent. The interfaces between the neighboring lamellae (marked as green line in Fig.3.23b) were also calculated. The calculated results show that the twin interface planes are in good agreement with the $\{112\}_{\mathrm{Tet}}$ twinning plane thus coherent.

Table 3.12 Coordinates of the inter-plate interface normal *n* expressed in the orthonormal crystal basis.

No.	n_1	n_2	n_3
1	0.564232	-0.503713	0.654153
2	0.577535	-0.474879	0.664036
3	0.582612	-0.484456	0.652583
4	0.531444	-0.52204	0.667114
5	0.577133	-0.491117	0.652473
6	0.579255	-0.506573	0.63863
7	0.576666	-0.487242	0.655783
8	0.553357	-0.498681	0.667168
9	0.580171	-0.499824	0.6431
10	0.557753	-0.508412	0.65607
11	0.549901	-0.503883	0.666116
12	0.56102	-0.516914	0.646573
13	0.563209	-0.507294	0.652264
14	0.555645	-0.483403	0.676447
Mean value	0.565129	-0.499292	0.656763

3.3.5 Summary

$Ni_{54}Mn_{24}Ga_{22}$ alloys were prepared by arc-melting and suction-cast. The two processed alloys have the identical tetragonal crystal structure, but the grain sizes were refined through suction-cast, resulting in an increase of transformation hysteresis and an improvement of mechanic property. The fractures occur mainly along the austenite grain boundaries. The adjacent plates have the misorientation of 80°~85° around $<110>_{Tet}$ axes. Locally, there are four types of martensite plates and each plate consists of paired fine variants, thus totally eight variants can be found in a martensite colony. The paired fine variants in each plate were found to be compound twin related with the $\{112\}_{Tet}$ as the twinning plane and the $<11\bar{1}>_{Tet}$ the twinning direction. The inter-plate interfaces are close to $\{1\bar{1}2\}_{Tet}$ plane but with ~3° deviation, while the interfaces of two paired fine variants are in good agreement with $\{112\}_{Tet}$ twinning plane.

Chapter 4 Austenite-7M-NM transformation

4.1 Formation of self-accommodated 7M martensite

Generally, in a transformation from high-symmetry austenite to low-symmetry martensite, more than one martensite variants can be induced in the same austenite grain to minimize the macroscopic transformation strain. Since the crystal structures of two phases are different, the elastic strain is generated by crystal lattice mismatch between martensite and its parent phase, as well as between differently oriented variants of martensite. Reducing the strain energy is an essential factor in the nucleation and growth processes of martensitic transformation, which can be achieved through the formation of unroated and undistorted phase boundaries and the self-accommodation of martensite variants. In this section, we selectively prepared the polycrystalline Ni-Mn-Ga alloys with the nominal composition of $Ni_{53}Mn_{22}Ga_{25}$, for the observation of the morphologic characters associated with martensite transformation at room temperature. Detailed microstructural investigation on the co-existed austenite and incommensurate 7M modulated martensite was performed by EBSD measurements. The formation of diamond-shaped martensite was evidenced at the beginning of the transformation and the mechanism of self-accommodation during nucleation and growth was further discussed.

4.1.1 Martensitic transformation temperatures and crystal structure

The off-stoichiometric Ni-Mn-Ga polycrystalline alloy with nominal composition of $Ni_{53}Mn_{22}Ga_{25}$ (at.%) was prepared. The composition of the alloy was verified by energy dispersive X-ray spectrometry (EDS) to be $Ni_{53.4}Mn_{21.8}Ga_{24.8}$. Fig.4.1 shows the measured DSC curves for the $Ni_{53}Mn_{22}Ga_{25}$ alloy on heating and cooling the sample. The forward martensitic transformation start temperature (M_s) and finish temperature (M_f) were determined to be 13.5℃ and 4.9℃, respectively; the inverse martensitic transformation start temperature (A_s) and finish temperature (A_f) were

16.3℃ and 30.1℃, respectively. In addition, much smaller peaks appear in the DSC curve on the cooling and the heating at the temperatures below -10°C (as arrowed in the figure), indicating the possibility of further transformation of the already formed martensite. It is noted that the martensitic transformation temperatures are around room temperature, suggesting that the co-existence of austenite and martensite at room temperature is possible. DSC curves also indicate that the Curie temperature (T_c) of the alloy is ~68.8℃ on cooling and ~74.6℃ on heating, respectively. The decrease of the magnetic transition temperatures with respect to that of the stoichiometric Ni_2MnGa alloy should be attributed to the excess of Ni [116].

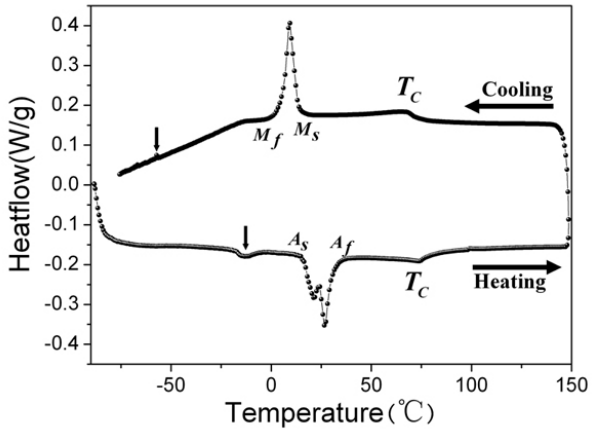

Fig.4.1 DSC curves of $Ni_{53}Mn_{22}Ga_{25}$ alloy on heating and cooling.

The powder XRD patterns of $Ni_{53}Mn_{22}Ga_{25}$ alloy measured at 25°C, -30°C and -120°C are shown in Fig.4.2, corresponding to the states of the coexistence of austenite and 7M modulated martensite, the single 7M modulated martensite and the coexistence of 7M and NM martensite. Results show that the high temperature austenite has a cubic structure ($Fm\bar{3}m$, No. 225) with lattice constant a_A = 5.811 Å. The 7M martensite was determined to possess a monoclinic long-period superstructure (P2/m, No. 10) with lattice constants a_{7M} = 4.222 Å, b_{7M} = 5.537 Å, c_{7M} = 41.982 Å, and β = 92.5°. The NM martensite has a tetragonal structure (I4/mmm, No. 139) with lattice constant $a_{Tet} = b_{Tet}$ = 3.879 Å and c_{Tet} = 6.511 Å. It is evidenced from the XRD experiments that on cooling, the parent austenite firstly transforms to the 7M modulated martensite and then the formed 7M modulated

martensite transforms to the NM martensite. Hence, the 7M modulated martensite is a thermodynamically metastable phase, intermediate between the parent austenite and the final stable NM martensite. The 7M to NM transformation will be addressed in the subsequent section.

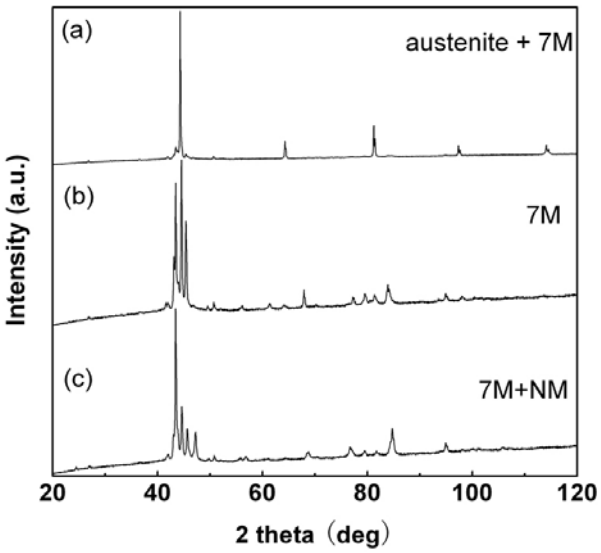

Fig.4.2 Powder XRD patterns of $Ni_{53}Mn_{22}Ga_{25}$ alloy measured at (a) 25°C; (b) -30°C and (c) -120°C.

4.1.2 Microstructure features of austenite to 7M transformation

By examining the bulk samples by SEM, we observed the microstructure composed of co-existing austenite and 7M martensite at room temperature. A backscattered electron (BSE) image covering the two phases in the same austenite grain is shown in Fig.4.3a. In the figure, the plate-like martensite in different contrasts represents different variants; while the austenite has a uniform contrast. It is seen that on cooling from high temperature, the martensite initially formed into a diamond-like structure; then the "diamond" gradually outstretched into the paired much longer martensite plates from the tips of the diamond and finally occupied the entire austenite grain. For further insight into the special diamond configuration, we performed EBSD measurements on the microstructure using the structural parameters determined from XRD measurements. Fig.4.3b shows the EBSD orientation

micrograph for the 7M martensite “diamond” surrounded by the austenite. The austenite and martensite variants are colored according to their crystallographic orientation referring to the sample coordinate system. It is seen that in the “diamond”, there are four distinct variants (denoted as A, B, C and D in the figure) placed back to back. Each variant have a straight phase interface, *i.e.* habit plane, connecting to the parent austenite.

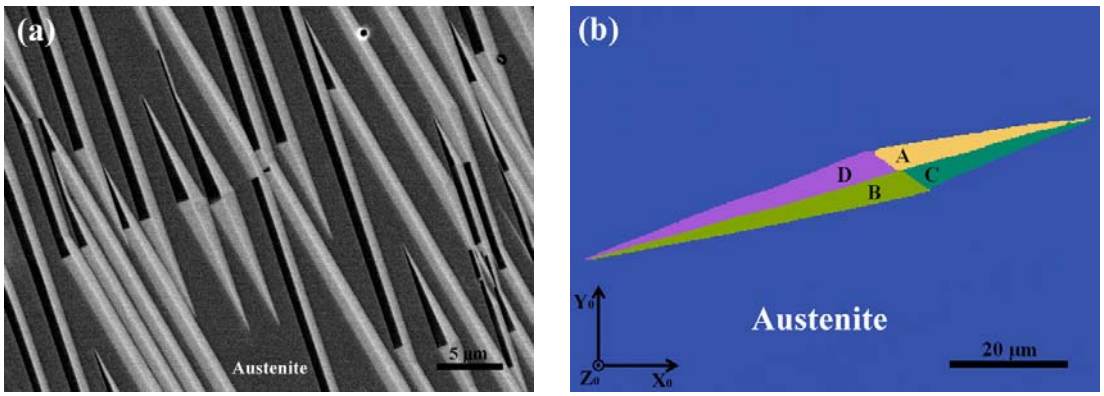

Fig.4.3 (a) BSE image of co-existing austenite and 7M martensite. (b) EBSD micrograph of martensite “diamond” composed of four variants (denoted as A, B, C and D) surrounded by austenite. The coordinate frame (X_0-Y_0-Z_0) referring to the sample coordinate frame.

Further calculations indicate that the neighbouring variants are twin-related and the twin modes are consistent with our former results in $Ni_{50}Mn_{30}Ga_{20}$ alloy. The twinning elements are slightly different from those of $Ni_{50}Mn_{30}Ga_{20}$ alloy due to the slight difference in lattice parameters of the two alloys. The twin interfaces were coincident with the respective twinning planes (K_1 plane), hence all these interfaces could be considered as coherent interfaces with low interfacial energy. Therefore, when these relationships refer to diamond-type morphology, the martensite “diamond” consists of type I twin (A:C/B:D) and compound twin (A:D/B:C); the long ridge of the martensite “diamond” corresponds to type I twin interface and the short ridge to compound twin interface. The “diamond” thus can be regarded as being built up of two spears (A:C and B:D pair) placed back to back.

Fig. 4.4 shows the microstructure evolution of the martensite “diamond” during

inverse transformation observed under an optical microscope. The sample was firstly pre-cooled into full martensite state and then subjected to the optical microscope observation at room temperature. It is seen that with the increasing temperature of the sample, the four variants in the martensite "diamond" shrink simultaneously by coordinated movement of phase interfaces till disappearance. As martensitic transformation is totally reversible, it indirectly manifests that during forward transformation, the growth of the "diamond" is through the coordinated mutual movement of the four phase interfaces into austenite matrix before it outstretches into long plates.

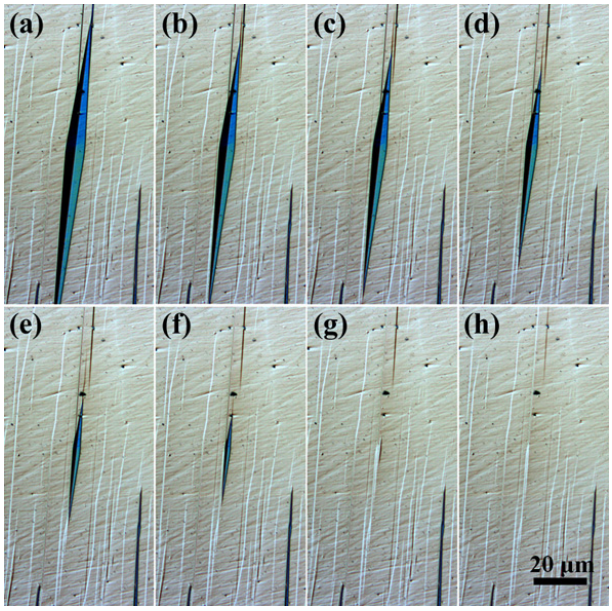

Fig.4.4 Microstructure evolution of the "diamonds" during the transformation from martensite to austenite.

Fig.4.5 shows the orientation micrographs reflecting the further growth of the martensite variants from the "diamond". It is seen in Fig.4.5a that the growth of the "diamond" proceeds by the elongation through the forward motion of spears, *i.e.* A:C or B:D pair. This elongation results in the formation of type II twin behind the spears. Then the "diamond" gradually grows into the paired plates, as shown in Fig. 4.5b. Occasionally, it was also found that the growth of the martensite variants can be realized by the formation of the fork configuration (A:D or B:C pair), as shown in Fig.

4.5c, where one thin plate bifurcates away from the other plate. The adjacent two bifurcated thin plates also tend to form into a spear. With the abovementioned two types of growth manner for the "diamond", a large number of martensite plates form and they always keep spear configuration adjacent to the austenite matrix, as shown in Fig.4.5d. Locally, a cluster of four types of martensite variants, *i.e.* A, B, C and D, constitutes one variant group. It is usually observed that there are several variant groups formed in the same austenite grain. An example is shown in Fig. 4.6.

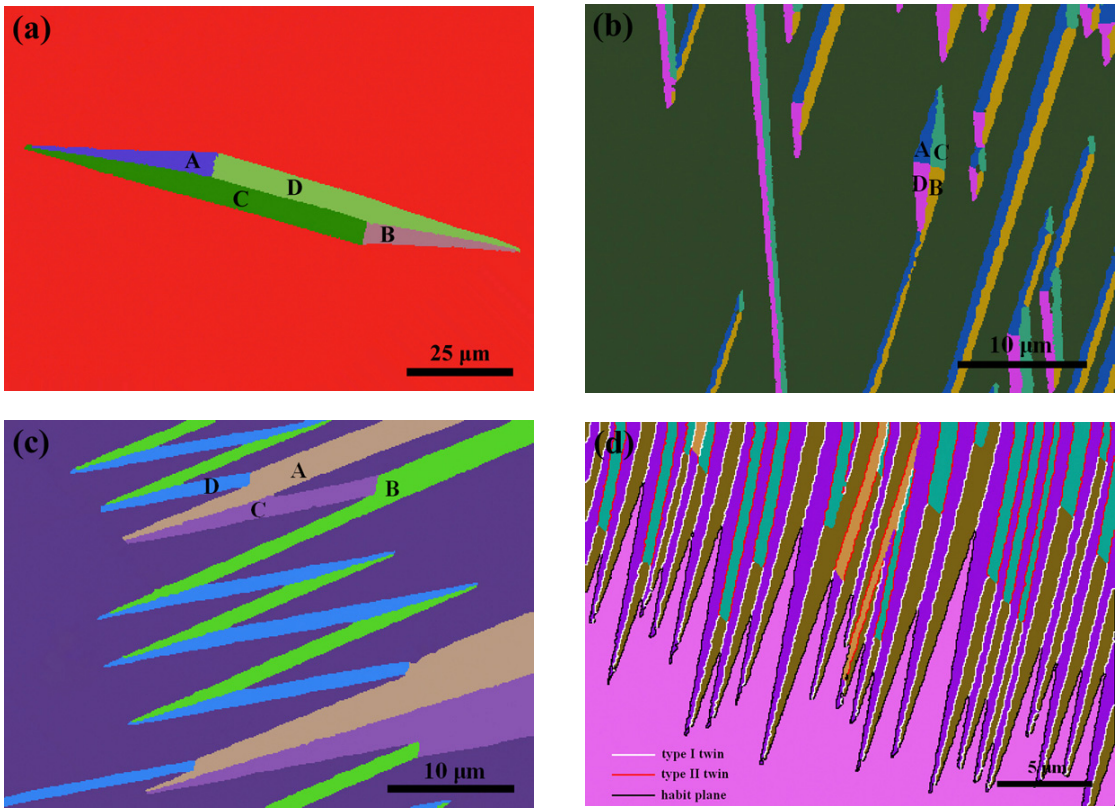

Fig.4.5 EBSD orientation map with co-existing two phases: (a) elongation of martensite "diamond"; (b) formation of paired plates from the "diamond"; (c) formation of the fork configuration by bifurcating; (d) formation of a large number of martensite plates keeping spear configuration adjacent to the austenite matrix.

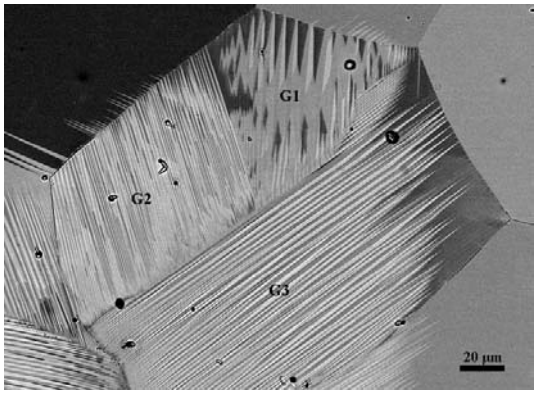

Fig.4.6 Formation of various variant groups (G1, G2, G3 in the figure) in an austenite grain.

Based on the above observations, it can be concluded that the growth of 7M martensite experiences two distinguished stages. The first stage is the coordinated growth of "diamond" from the initial formed nucleus. The second is the transition from the "diamond" into the martensite plates. The diamond only exists at the beginning of the transformation process.

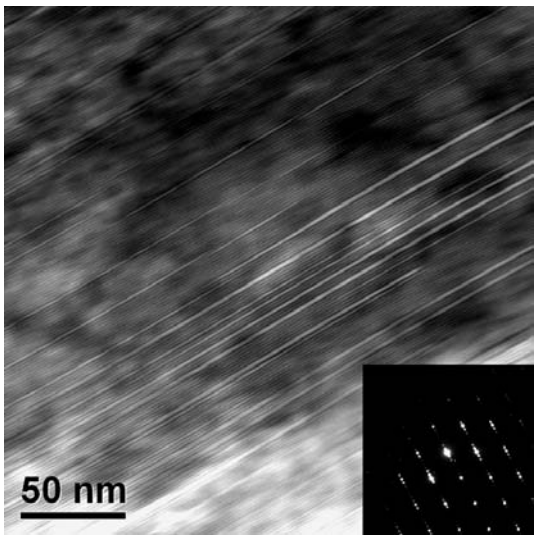

Fig.4.7 TEM bright field image showing the internal sub-structure of the 7M martensite plate. The corresponding SAED patterns are shown in the lower right corner.

Fig.4.7 shows the TEM bright field image showing the detailed microstructure inside the 7M martensite plate. The incident beam is along the $<210>_{7M}$. The

corresponding SAED pattern shows the typical character of the 7M martensite that two main spots are divided by six satellite spots. As the basal planes are at edge-on position, the lattice fringes can be seen in the figure. It is noted that considerable stacking faults on the basal plane can be recognized in the martensite plates. The occurrence of the stacking faults should be as a kind of complementary shear [117] to accommodate the transformation strain and to achieve the formation of an invariant plane between the austenite and the martensite.

4.1.3 Confirmation of the orientation relationship between austenite and 7M martensite

By crystallographic calculation using the orientation data of the two phases, we confirmed the energetically favorable OR between the austenite and 7M martensite to be the Pitsch relations, *i.e.* $(101)_A//(1\,\bar{2}\,\overline{10})_{7M}$ and $[10\,\bar{1}]_A//[\overline{10}\;\overline{10}\;1]_{7M}$, as we have found in $Ni_{50}Mn_{30}Ga_{20}$ alloy. The corresponding pole figures are shown in Fig. 4.8, which is plotted using the orientation data of the two phases in Fig.4.5b. Fig. 4.8a displays the $\{101\}_A$ pole figure of austenite and the $\{1\,\bar{2}\,\overline{10}\}_{7M}$ pole figures of the four martensite variants in the macroscopic sample coordinate system. It is noted that from the four martensite variants, one $\{1\,\bar{2}\,\overline{10}\}_{7M}$ pole of each variant is overlapped and they are all common to one $\{101\}_A$ pole of the austenite, as marked in Fig.4.8a, suggesting $\{101\}_A//\{1\,\bar{2}\,\overline{10}\}_{7M}$. Accordingly, the four variants share a common $<\overline{10}\;\overline{10}\;1>_{7M}$ pole that is in common with one $<10\,\bar{1}>_A$ pole of the austenite, as shown in Fig.4.8b, indicating $<10\,\bar{1}>_A//<\overline{10}\;\overline{10}\;1>_{7M}$. Therefore, the orientation relationships between the austenite and the 7M martensite are confirmed to be Pitsch OR with $\{101\}_A//\{1\,\bar{2}\,\overline{10}\}_{7M}$ and $<10\,\bar{1}>_A//<\overline{10}\;\overline{10}\;1>_{7M}$, which is well consistent with our previous result.

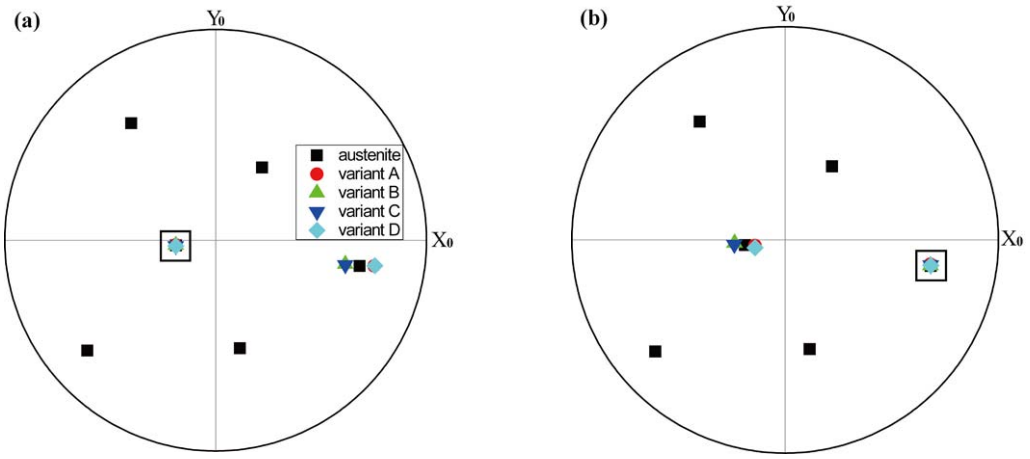

Fig 4.8 Identification the Pitsch OR from the corresponding pole figures of the two phases. (a) $\{101\}_A//\{1\bar{2}\,\overline{10}\}_{7M}$; (b) $<10\,\bar{1}>_A//<\overline{10}\;\overline{10}\;1>_{7M}$. The common poles are squared in the figures.

4.1.4 Experimental determination of habit plane

The habit plane is believed to be an invariant plane unrotated and undistorted on the macroscopic scale. In the present study, the habit plane between the austenite and the 7M martensite was determined by the indirect two-trace method [113]. To achieve statistical reliability, sixteen habit plane normals were calculated. The calculation results, expressed in the coordinate frame of austenite and listed in Table 4.1, manifest that the habit planes between the austenite and the 7M martensite are irrational. The mean values of the calculated habit plane normals determined using the formula $\bar{n} = \frac{\sum n_i}{\left\|\sum n_i\right\|}$ is $\{0.736130, 0.673329, 0.068855\}_A$, which is near to $\{110\}_A$ with 4.7° deviation.

Table 4.1 Coordinates (n_1, n_2, n_3) of the calculated habit plane normals and the mean habit plane. All the indices are expressed in the coordinate frame of austenite.

No.	n_1	n_2	n_3
1	0.738894	0.665652	0.104611
2	0.738351	0.669307	0.082866
3	0.756754	0.650963	0.059750
4	0.723577	0.687154	0.065253
5	0.742925	0.662117	0.098304

6	0.733350	0.676126	0.071078
7	0.712261	0.698620	0.067933
8	0.762323	0.647162	0.006652
9	0.722641	0.688243	0.064122
10	0.724527	0.680720	0.108080
11	0.762845	0.644734	0.048838
12	0.728520	0.684741	0.019681
13	0.737620	0.666750	0.106587
14	0.745335	0.663200	0.068130
15	0.713322	0.697283	0.070484
16	0.727408	0.683697	0.058616
Mean value	0.736130	0.673329	0.068855

4.1.5 Calculation based on the crystallographic phenomenological theory

In general, the martensitic transformation tends to proceed in a self-accommodated manner to minimize the total transformation strain when no external stress is applied. For further analyzing the martensitic transformation crystallography and the self-accommodation mechanism of 7M martensite, the crystallographic phenomenological theory of martensitic transformation [23] was used to perform the theoretical calculation, which has been well applied to the prediction of crystallographic parameters in many shape memory alloys [118-122]. This prediction is based on the assumption that the interface between austenite and its product phase is invariant on a macroscopic scale.

In the present austenite (cubic)-7M martensite (monoclinic) system, the lattice invariant shear for the calculation was supposed to occur on the basal plane in either of the two opposite crystallographic directions, which correspond to $\{101\}_A<10\bar{1}>_A$ system in the parent phase. As the 7M plate possesses the modulated structure, the structure itself (lattice modulation) provides the main contribution of invariant shear and the remaining is balanced by the stacking faults. The faulted nature of martensite plate has been revealed by TEM observation, as illustrated in Fig.4.7. By inputting the lattice parameters of austenite and martensite for the phenomenological calculation, the results show that there are 24 pairs of habit plane normal and shape deformation direction due to the symmetry of the cubic system, corresponding to 24 variants. The

24 variants are divided into 6 groups and each group is composed of four twin-related variants distributed around one of the $\{101\}_A$ pole. As an example, Table 4.2 shows the habit plane normals, shape deformation directions and shape deformation matrices of variant A, B, C and D in the group around $(101)_A$ pole. The magnitude of the shape deformation for each variant is 0.09596, but the shape deformation direction is different. The theoretical habit plane normal was predicted to be $\{0.720332, 0.692379, 0.041627\}_A$, which is consistent with experimental results with 2.11° deviation.

Table 4.2 Habit plane normals, shape deformation directions and shape deformation matrices of variant A, B, C and D in the group around $(101)_A$ pole calculated according to the phenomenological theory. The results are expressed in the austenite basis.

Variant	Habit plane normal	Shape deformation direction	Shape deformation matrix
A	[0.692379, 0.041627, 0.720332]	[-0.726173, 0.039664, 0.686367]	$\begin{pmatrix} 0.951753 & -0.002901 & -0.050195 \\ 0.002635 & 1.000158 & 0.002742 \\ 0.045603 & 0.002742 & 1.047444 \end{pmatrix}$
B	[0.720332, 0.041627, 0.692379]	[0.686367, 0.039664, -0.726173]	$\begin{pmatrix} 1.047444 & 0.002742 & 0.045603 \\ 0.002742 & 1.000158 & 0.002635 \\ -0.050195 & -0.002901 & 0.951753 \end{pmatrix}$
C	[0.720332, -0.041627, 0.692379]	[0.686367, -0.039664, -0.726173]	$\begin{pmatrix} 1.047444 & -0.002742 & 0.045603 \\ -0.002742 & 1.000158 & -0.002635 \\ -0.050195 & 0.002901 & 0.951753 \end{pmatrix}$
D	[0.692379, -0.041627, 0.720332]	[-0.726173, -0.039664, 0.686367]	$\begin{pmatrix} 0.951753 & 0.002901 & -0.050195 \\ -0.002635 & 1.000158 & -0.002742 \\ 0.045603 & -0.002742 & 1.047444 \end{pmatrix}$

Apparently, the shape deformation matrix of one single variant is far from the identity matrix, and the magnitude of deformation, *i.e.* 0.09596, is quite large. Supposing that four variants constitute a diamond group with equal volume fraction (1/4), the total shape deformation matrix can be approximated by the method of summation. Taking $(101)_A$ group as an example, the total shape deformation matrix is

$$\begin{pmatrix} 0.999599 & 0 & -0.002296 \\ 0 & 1.000158 & 0 \\ -0.002296 & 0 & 0.999599 \end{pmatrix}. \tag{4.1}$$

Since the matrix of Eq. (4.1) is symmetric, it is orthogonally diagonalizable. After the diagonalization, the total shape deformation matrix becomes as follows:

$$\begin{pmatrix} 0.997303 & 0 & 0 \\ 0 & 1.000158 & 0 \\ 0 & 0 & 1.001895 \end{pmatrix}. \tag{4.2}$$

The total shape deformation matrix is quite close to the identity matrix, thus the transform strain are effectively cancelled out by the combination of the four variants. Hence, the "diamond" as a whole is an energetically feasible, self-accommodated combination when formed from the parent phase. Further compensation of transformation strain can be achieved by the combination of different variant groups. The total shape deformation matrix of all the 6 variant groups is

$$\begin{pmatrix} 0.999599 & 0 & 0 \\ 0 & 0.999599 & 0 \\ 0 & 0 & 1.000158 \end{pmatrix}. \tag{4.3}$$

This combination of all six self-accommodation groups gives the minimum transformation strain energy.

Now, we pay our attention to the more local area in a self-accommodated variant group and the total deformation matrices for the three types of twin pairs, *i.e.* A:C (or B:D) pair, A:B (or C:D) pair and A:D (or B:C) pair, are calculated.

(1) Type-I twin pair (A:C) :

$$\begin{pmatrix} 0.997302 & 0 & 0 \\ 0 & 0.998818 & 0 \\ 0 & 0 & 1.003238 \end{pmatrix} \tag{4.4}$$

(2) Type-II twin pair (A:B):

$$\begin{pmatrix} 0.996399 & 0 & 0 \\ 0 & 1.001065 & 0 \\ 0 & 0 & 1.001894 \end{pmatrix} \tag{4.5}$$

(3) Compound twin pair (A:D):

$$\begin{pmatrix} 0.952844 & 0 & 0 \\ 0 & 1.000158 & 0 \\ 0 & 0 & 1.048646 \end{pmatrix} \tag{4.6}$$

The total shape deformation matrices of type I and type II twin pair are quite close to the identity matrix compared with the deformation matrix of a single variant. Thus, they are self-accommodated. However, the total shape deformation matrix of the compound twin is not close to the identity matrix. Thus, the compound twin can not effectively accommodate the transformation strain.

The self-accommodation is a process that minimize the transformation strain hence the strain energy. This process should guarantee an invariant interface between austenite and martensite. Considering the diamond model and without losing coherence at the phase interfaces, the initial growth is through the coordinated mutual movement of the four habit planes into the austenite matrix. This expansion will be blocked due to the accumulated elastic strain caused by the increased volume fraction of the transformed martensite, as elastic strain energy is proportional to the volume of the martensite [123]. Then the possible route of further growth for the diamond can be through the extension of either type I twin (A:C or B:D) or compound twin (A:D or B:C), if the chemical driving force is sufficient. As compound twin is not self-accommodated, it is not favorable that the growth of a variant group is through the extension of compound twin. Then, the spears (type I twin) should be responsible for the variant growth. Comparing the total shape deformation matrix over variants A and C (or B and D) with that over variants A, B, C and D, there still exist some residual unaccommodated elastic strain [124]. This residual strain can be further accommodated by introducing the type II twin pair, as the situation in Fig.4.5a and b, which renders the growth of martensite through the forward progression of the spear (type I twin). As the martensite “diamond” only consists of type I and compound twin systems, the type II twin should be a secondary twin after further shear of variant pair A and D or B and C during the growth process. Locally, type I twin and type II twin are bridged by compound twin and the compound twin interface has always appeared with its neighboring Type I and Type II twin interfaces as a whole in the final

martensite microstructure. If the chemical driving force cannot overcome the elastic barrier to induce the forward movement of spears, the martensite tends to form much thinner plates for the reduction of the elastic strain energy, as the thin plate bifurcates from the other plate in Fig. 5c.

4.1.6 Summary

The structural and microstructural characters from austenite to 7M martensite in a $Ni_{53}Mn_{22}Ga_{25}$ alloy with the martensitic transformation temperatures around room temperature were investigated. The formation of characteristic diamond-like martensite microstructure with four variants (A, B, C and D) during the martensitic transformation was evidenced. As revealed by EBSD measurements, the martensite "diamond" consists of type I twin (A:C and B:D pair) and compound twin (A:D and B:C pair); the long ridge of martensite "diamond" corresponds to type I twin interface and the short ridge to compound twin interface. The "diamond" thus can be regarded as being built up of two spears (A:C and B:D pair) placed back to back. The favourable way for the "diamond" growth is through the forward progression of spears. The OR of the martensitic transformation was further confirmed to be Pitsch relation according to the crystallographic calculation. The habit plane normals were determined experimentally to be $\{0.736130, 0.673329, 0.068855\}_A$ by means of indirect double-trace method, which is consistent with results of phenomenological theory with 2.11° deviation. Further calculation indicates that the characteristic four variants in a "diamond" group clustered around one $\{101\}_A$ pole and the elastic strains around martensite were effectively cancelled out by making such a group. Both A:C (or B:D) and A:B (or C:D) variant pairs are self-accommodated, whereas A:D (or B:D) variant pair is not.

4.2 Clarification of structure and stability of long-period modulated martensite

As one of the common characteristics of the β-phase alloys [71], Heusler alloys [70, 125] and piezoelectric materials [126], the transformation process from the parent austenite to the product martensite produces long-period lattice-modulated structures. The thermodynamic stability and the crystallographic nature of this modulated structures have been questioned [81], because the product martensite was found to have a non-modulated (NM) structure in several alloy systems [65, 127-130]. By analyzing the crystal lattice mismatch between the austenite and the NM martensite, Khachaturyan *et al.* [130, 131] interpreted that the modulated structure with a plate-like macroscopic shape is actually the combination of twin-related variants of the normal NM martensite phase, wherein the twin domain has a lamellar shape in the order of a few atomic layers. The main argument for this structure model is that the geometrical requirement for an invariant habit plane between the parent and the product lattices can be fulfilled, which lowers the volume-dependent elastic energy.

If the long-period modulated martensite is composed of nanotwin-related lamellae with a simple NM structure, the lattice constants of the modulated martensite phase should satisfy some specific relations with those of the parent austenite and the NM martensite [130, 131]. Such relations have been taken as the criteria for the verification of the nanotwin combined structure (*i.e.* adaptive phase). For instance, excellent fits between the measured and calculated lattice constants were found in Ni-Al, Fe-Pd and lead-based ferroelectric perovskites [130, 131]. However, the validity of this concept is strongly questioned in lead titanate [126], because the Raman spectroscopy measurement results demonstrated that the modulated phase possesses an independent crystal structure.

Recently, this contradiction arose in the newly developed Ni-Mn-Ga ferromagnetic shape memory alloys. Righi *et al.* [75] made a detailed study on the crystal structure of the so-called seven-layered (7M) modulated martensite by application of the superspace approach to the powder X-ray diffraction (XRD)

analysis. Results showed that the modulated martensite has its own crystal structure with an incommensurate 7M modulation, other than the nanotwin combined structure. Based upon the XRD measurement and the concept of adaptive phase, Kaufmann *et al.* [81] examined the co-existing austenite, 7M and NM martensite in an epitaxial Ni-Mn-Ga film. They concluded that the 7M modulated martensite can be simply constructed from nanotwinned lamellae of a tetragonal martensite phase with $(5\,\bar{2})_2$ stacking sequence, ruling out the existence of the independent modulated structure. The 7M modulated martensite phase built up from microscopic twins may evolve into the final NM martensite phase by thickening the nanotwin width through branching [81].

Notably, the controversy on long-period modulated structure remains unclarified for many alloy systems. Indeed, it is very difficult to make a direct validity discrimination of the above two structure models by either diffraction or thermodynamic measurements. On one hand, the formation of the modulated martensite variants is very sensitive to local constraints. On the other hand, different characterization techniques require different sample geometries and sizes that represent different internal constraints. Clearly, significant inconsistency may result from different experimental techniques and the characterization information (global and local) suffers from a lack of generality. So far, numerous experimental studies of modulated structures have been performed almost exclusively by diffraction techniques. The role of the micrstructural correlations between martensite plates has seldom been taken into account by either experimental examination or the nanotwin combination theory. These microstructural features surely have a strong influence on the stability of the modulated martensites and their functionality as shape-memory materials. In this context, insight into the microstructure-property correlation may bring convincing clues to clarify the structure of long-period modulated martensite.

Under such a background, the polycrystalline bulk $Ni_{53}Mn_{22}Ga_{25}$ alloy having martensitic transformation near room temperature is selected as an ideal testing material for the following reasons. The alloy displays a transformation sequence from the austenite to the modulated martensite and then the NM martensite during

continuous cooling detected by X-ray diffraction (XRD) measurements, and islands of modulated martensite and NM martensite coexist in some initial austenite grains when kept at room temperature. Using the local electron backscatter diffraction (EBSD) orientation determination technique, the crystal structure nature of the long-period modulated martensite was unambiguously clarified through microstructural and crystallographic examination.

4.2.1 Lattice modulation and nanotwin combination

The XRD pattern of the modulated phase in $Ni_{53}Mn_{22}Ga_{25}$ alloy measured at -30℃, as shown in Fig. 4.9a, is first solved and further refined with the incommensurate 7M modulation structure model (hereafter denoted 7M(IC) in this section) [75]. It showed that the modulated phase has a monoclinic long-period superstructure (P2/m, No. 10) with the lattice constants a_{7M} = 4.222 Å; b_{7M} = 5.537 Å; c_{7M} = 41.982 Å, and β = 92.5°. The unit cell of the combined nanotwins was artificially constructed based on the lattice constants of the tetragonal NM unit cell ($a_{Tet} = b_{Tet}$ = 3.879Å, c_{Tet} = 6.511Å) and the $(5\bar{2})_2$ stacking sequence of $(112)_{Tet}$ twins [81]. The resolved lattice constants of the adaptive phase (with a structure of combined nanotwins) [81, 130] are a_{ad} = 4.257 Å, b_{ad} = 5.486 Å, c_{ad} = 29.446 Å, and β_{ad} = 94.2°. The calculated atomic coordinates of the nanotwined superstructure is shown in Appendix III. The XRD patterns are recalculated using the two structure models and are displayed in Fig. 4.9b and c. It is seen that the two structures possess very close pattern to the measured one. Close examination reveals that the 7M(IC) model delivers a slightly better fit to the measured profile. The distinguishable difference between the two structures appears in the secondary minor peaks (as arrowed in the figure) around the three main diffraction peaks in the 2θ range from 40 to 50°.

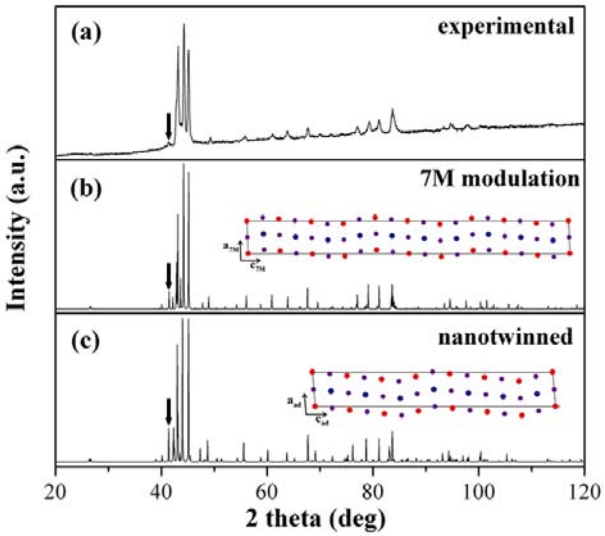

Fig.4.9 XRD patterns for the modulated martensite: (a) measured at -30°C; (b) recalculated pattern with the 7M(IC) superstructure; (c) recalculated with the tetragonal nanotwin combined unit cell. The insets show the unit cells of the two structures.

The two structure models of the modulated phase are further tested with the adaptive phase criteria [130]. The lattice constants of the 7M (IC) structure and the nanotwin combination are expressed in the cubic austenite coordinate system and compared with those calculated using the equation ($a_{ad} = c_{Tet} + a_{Tet} - a_A$; $b_{ad} = a_A$; $c_{ad} = a_{Tet}$) proposed by the nanotwin combination theory [130]. The results are given in Table 4.3. Clearly, the two sets of lattice constants also possess excellent agreement with the calculated ones. This indicates that the verification criterion of the nanotwin combination theory is not sufficient to discriminate the two structures for the modulated phase.

Table 4.3 Lattice constants of the modulated martensite in the frame of 7M(IC) and nanotwin combination, in comparison with those calculated according to the adaptive phase criteria ($a_{ad} = c_{Tet} + a_{Tet} - a_A$; $b_{ad} = a_A$; $c_{ad} = a_{Tet}$). Noted that all the lattice parameters are expressed in the cubic parent phase coordinate system.

Lattice constants	7M(IC) (Å)	Nanotwin combination (Å)	Theoretical (Å)
a	6.082	6.200	6.186
b	5.823	5.761	5.811
c	5.537	5.486	5.486

4.2.2 EBSD measurements on the coexistence of three phases

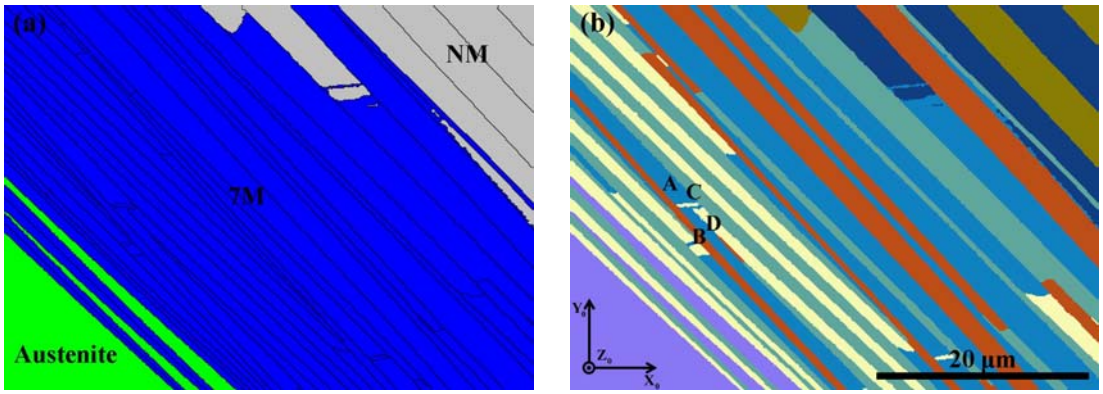

Fig.4.10 EBSD map showing (a) the coexistence of austenite, 7M(IC) and NM martensite within an initial austenite grain, and (b) four 7M variants designated as A, B, C and D where the coordinate frame (X_0-Y_0-Z_0) refers to the macroscopic sample coordinate system.

Fig.4.10a shows the measured EBSD phase micrograph covering one initial austenite grain, where the austenite is colored in green, the modulated martensite (identified with the 7M(IC) structure) in blue and the tetragonal NM martensite in gray. As no obvious composition variation of the constituent Ni, Mn and Ga elements was detected with energy-dispersive X-ray analysis (SEM/EDX) over the three phase regions, it rules out the possibility that different kinds of martensite may result from composition fluctuation. It can be seen in Fig.4.10a that the three phases are located with a fixed adjacency, *i.e.* austenite – modulated martensite – NM martensite, further indicating that modulated martensite is the intermediate phase between the austenite and the final normal NM martensite. Moreover, the modulated and the NM martensite are in plate-shape and the neighboring modulated martensite and NM plates stretch roughly in the same direction. In general, the plates of the modulated martensite are thinner than those of the NM martensite. When approaching the NM martensite, some modulated plates tend to thicken and others to vanish, indicating that the transformation from the modulated to the NM martensite is accompanied by the reduction of the specific area of the NM plate interface. The spatial correlation of the

three phases that initiates, bridges and ends the martensitic tranformation and their morphological correlation shown in Fig. 4.10a provide another direct experimental evidence for the thermodynamic metastable essence of the modulated martensite.

Fig.4.11a shows a manually measured EBSD Kikuchi pattern from the modulated martensite. The patterns recalculated using the 7M(IC) structure data and the nanotwin combination data are displayed Fig.4.11b and c, respectively. As a whole, perfect matches can be found between the measured bands and those calculated with the two structure models, especially for the high intensity bands. However, for the low intensity bands that reflect the details of the substructure, as marked with a pair of white lines in the pattern, the two solutions display clear differences with respect to the measured bands. The 7M(IC) model yields the better fit, evidencing that the 7M(IC) structure is closer to the real structure.

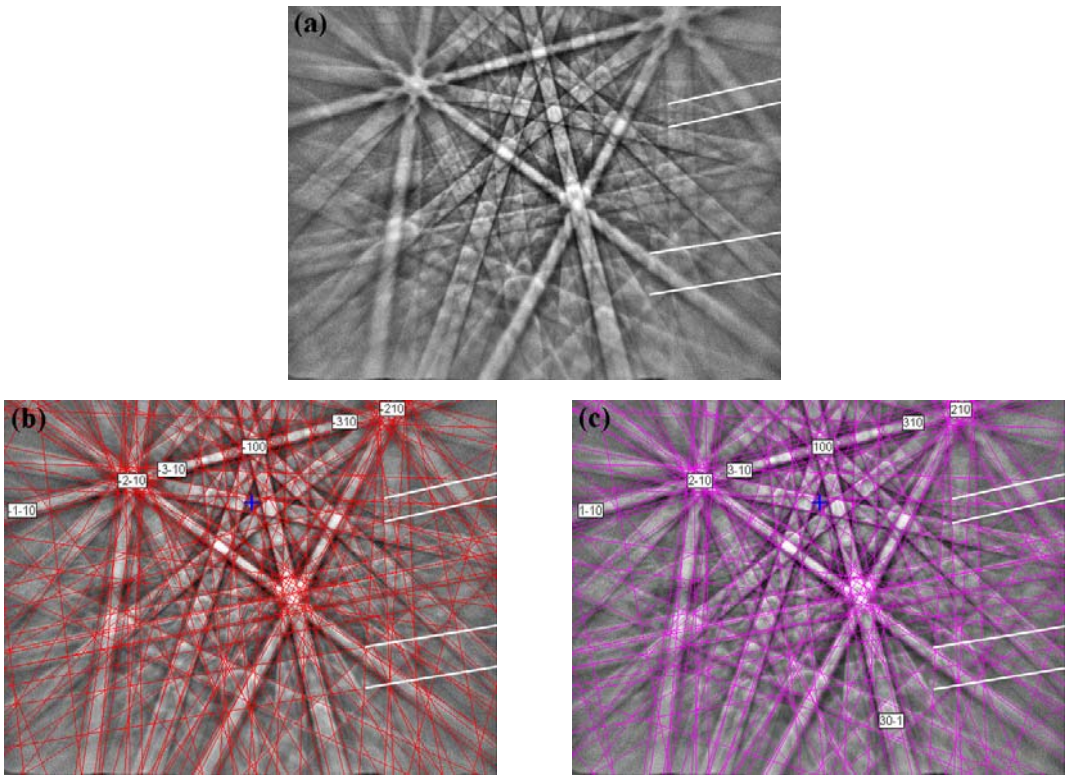

Fig.4.11 (a) Measured EBSD Kikuchi pattern of the modulated martensite; (b) recalculated with the 7M (IC) structure; (c) recalculated with the nanotwin combination structure.

Fig. 4.10b presents the EBSD orientation micrograph corresponding to Fig.4.10a,

where the three phases are colored according to their orientations. From Fig.4.10b, four 7M martensite variants A, B, C and D can be identified. With the measured orientation data (almost the same under the two structure models) of each variant, the orientation relationships between the neighboring variants and their interface planes were fully determined. In the frame of the 7M(IC) structure model, the four variants are twin-related. The twin relationships are the same as those mentioned above for the 7M martensite. The inter-plate interfaces are found to be coincident with the corresponding twinning planes. The analyses using the nanotwin combination model give the same results concerning the types of twins, but some differences appear in the twinning elements, as detailed in Table 4.4.

Table 4.4 Twinning elements of three types of twins in $Ni_{53}Mn_{22}Ga_{25}$ 7M martensite under the 7M(IC) and nanotwin combination models.

Model		Type I (A:C / B:D)	Type II (A:B / C:D)	Compound (A:D / B:C)
7M(IC)	K_1	$(1\ \bar{2}\ \overline{10})$	$(1.0632\ \bar{2}\ \overline{9.3676})$	(1 0 10)
	K_2	$(\overline{1.0632}\ \bar{2}\ 9.3676)$	$(\bar{1}\ \bar{2}\ 10)$	$(\bar{1}\ 0\ 10)$
	η_1	$[\overline{10.5719}\ \overline{10}\ 0.9428]$	$[\overline{10}\ \overline{10}\ 1]$	$[\overline{10}\ 0\ 1]$
	η_2	$[10\ \overline{10}\ \bar{1}]$	$[10.5719\ \overline{10}\ \overline{0.9428}]$	[10 0 1]
	P	$(1\ \overline{0.0589}\ 10.5888)$	(1 0.0589 10.5888)	(0 1 0)
	s	0.1883	0.1883	0.0113
Nanotwin combination	K_1	$(1\ \bar{2}\ \bar{7})$	$(1.1023\ \bar{2}\ \overline{6.2839})$	(1 0 7)
	K_2	$(\overline{1.1023}\ \bar{2}\ 6.2839)$	$(\bar{1}\ \bar{2}\ 7)$	$(\bar{1}\ 0\ 7)$
	η_1	$[\overline{7.6497}\ \bar{7}\ 0.9072]$	$[\bar{7}\ \bar{7}\ 1]$	$[\bar{7}\ 0\ 1]$
	η_2	$(7\ \bar{7}\ \bar{1})$	$[7.6497\ \bar{7}\ \overline{0.9072}]$	[7 0 1]
	P	$(1\ \overline{0.0973}\ 7.6813)$	(1 0.0973 7.6813)	(0 1 0)
	s	0.2458	0.2458	0.0239

4.2.3 Inter-plate interface

To visualize the atomic match on the plate interface, the atomic correspondences of the type I twin interface is constructed under the two structure models and displayed in Fig. 4.12. For the 7M(IC) structure (Fig. 4.12a), some of the atoms on the interface are slightly deviated from their exact equilibrium position due to the

structure modulation. The plate interface is basically coherent and thus should have low interfacial energy. This coherence surely renders a good mobility in the twinning and detwinning process. The twinning configuration (the twinning shear plane and direction parallel to the plate interface) ensures that if only two variants (plates) exist in the material, one variant can be easily reoriented to the other by twinning or detwinning through the plate interface movement. This feature has been well observed in many magnetic field driven shape memory experiments in Ni-Mn-Ga alloys [8, 89, 90]. In contrast, if the modulated martensite has the $(5\,\bar{2})_2$ nanotwin combination structure, although the crystal structure differs slightly from the 7M(IC) structure, the plate interfacial feature and the in-plate structure (atomic shuffling in 7M(IC) plates and nanotwins in nanotwin combined plates) will be very different. As shown in Fig. 4.12b, the two orientation plates correspond to four tetragonal NM orientation variants that are in lamellar shape. The in-plate variants are twin related. The twinning elements of the $(112)_{Tet}$ nanotwin in the plate are determined to be $K_1=(112)_{Tet}$; $K_2=(11\,\bar{2})_{Tet}$; $\eta_1=[11\,\bar{1}]_{Tet}$; $\eta_2=[111]_{Tet}$ and the twinning shear s=0.344. The twinning shear is almost twice as that of the 7M(IC) twins (type I and type II). The inter-lamellar interfaces are the $(112)_{Tet}$ twinning planes and coherent. Due to this in-plate twin configuration, the atomic coherency at the plate interface is greatly deteriorated. At the plate interface, two thick lamellae and two thin lamellae from neighboring plates intersect, as illustrated in Fig. 4.12b. When the thick lamellae meet, they appear to have a $(1\,\bar{1}\,2)_{Tet}[\bar{1}\,11]_{Tet}$ twin relationship but with some degrees of deviation in the twinning plane and twinning direction, *i.e.* 4.97° between $(1\bar{1}2)_{Tet}$ planes and 2.62° between the $[\bar{1}11]_{Tet}$ directions. Using the two $(1\bar{1}2)_{Tet}$ planes as reference, the closest planes of the thin lamellae from the neighboring plates are $(010)_{Tet}$. The angular deviation between the two planes is 11.44°. Thus, the parallelism of the planes is far from perfect.

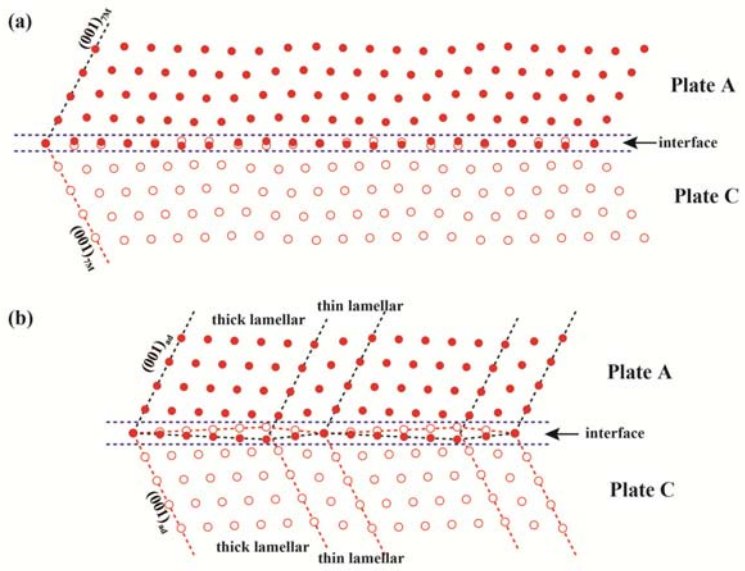

Fig.4.12 Atomic correspondences of type I twin interface of the modulated martensite viewed along the $[210]_{7M}$ direction constructed under (a) the 7M (IC) structure model; (b) the nanotwin combination structure model. For a clear representation, only Mn atoms are displayed.

To further quantify the atomic misfits at the plate interface under the two structure models, the average atomic displacement ($\bar{r}$) of the atoms on the plate interface from their equilibrium positions was calculated using the *L2* norm:

$$\bar{r} = \frac{1}{N}\sqrt{\sum_{i=1}^{N}(\Delta r_i)^2} \times 100\%. \tag{4.7}$$

Here, N represents the number of the atomic layers in one modulation period (N = 20 for the 7M(IC) structure and N = 14 for nanotwin combination structure); Δr_i is the amount of atomic displacement of the i^{th} atom on the plate interface from its equilibrium position. The results show that the average displacement is 1.52% for 7M(IC) structure and 3.81% for the nanotwin combination structure. It is clear that the deviation of the nanotwin combination at the plate interface is much larger than that of the 7M(IC) structure. In consequence, a high plate interfacial energy resulting from the atomic displacement for the nanotwin combination model could be expected. The thickening of the NM plate to reduce the specific interface displayed in Fig. 4.10a indirectly proves that the plate interface of the nanotwin combined martensite should possess high interfacial energy. Furthermore, the large mismatch on the plate

interfaces under the nanotwin combination model surely imposes significant constraints on the variant reorientation. For plate reorientation to achieve shape memory effect, it has to overcome two barriers. Firstly, no uniform magnitude of shear and shear system available for an easy coordinated atom displacement in the plate reorientation that is essential to a reversible external field induced shape change. Secondly, the coherent nanotwin interfaces that are densely distributed inside the plate act as pins to the movement of the plate interface. Under such circumstances, the plate reorientation resistance is inevitably enhanced. The loss of magnetic field induced shape change in tetragonal NM martensite is also well recognized in many Ni-Mn-Ga alloys [89]. Such experimental evidences indirectly provide support to the above analysis.

The main argument for the nanotwin combination model is that the nanotwin combined structure could offer reduced lattice mismatch with respect to the lattice of the parent austenite [130]. Actually, we will see that the 7M(IC) model offers even smaller lattice mismatch. The lattice misfits of the two structure models with respect to the cubic austenite are expressed in stress-free strain tensors [130]. The non-zero terms in these tensors (ε_{11}, ε_{22}, ε_{33}, γ) are shown in Table 4.5. It is evident that the nanotwin combination has a higher lattice mismatch than the 7M(IC) modulated structure.

Table 4.5 Strain tensors between matrix and product phases for austenite to 7M and austenite to adaptive phase (nanotwin combination structure) transformation.

	Austenite -7M modulation	Austenite - nanotwin combination
ε_{11}	0.0275	0.0360
ε_{22}	-0.0472	-0.0559
ε_{33}	0.0207	0.0210
γ	-0.0446	-0.0750

All the above results have demonstrated that the modulated martensite in the Ni-Mn-Ga alloy has its own crystal structure, other than the nanotwin combination of the tetragonal NM martensite. The transformation from the modulated martensite to the final NM martensite is realized by further lattice distortion, and this might

significantly degrade the magnetic field-induced shape memory performance.

4.2.4 Summary

In summary, we present experimental evidence for the thermodynamic stability and the crystal structure of the long-period modulated martensite in Ni-Mn-Ga alloys. It is proved that the modulated martensite is an intermediate state between the austenite to the NM martensite. It possesses its own crystal structure, instead of the nanotwins of the NM martensite (tetragonal simple structure) proposed by the nanotwin combination theory. The 7M(IC) structure can generate a reduced number of local variants and more favorable configuration for twinning and detwinning. This is essential to the attainability of the magnetic field induced shape change. The present results provide unambiguous evidence to clarify the long debated issue concerning the nature of the long-period modulated phases.

4.3 Role of 7M martensite in the transformation from austenite to NM martensite

So far, the specific roles of the modulated phase in bridging the transformation from the parent austenite to the final non-modulated (NM) tetragonal martensite and the microstructure evolution during the transformation as well as the constraints imposed by the microstructure change on the transformation path have not yet been addressed up to now. A clear explanation of these issues is surely helpful in understanding the shape memory potentials of ferromagnetic shape memory alloys and in guiding their future developments. Based on such requests, we conducted a thorough crystallographic and microstructural examination of a bulk $Ni_{53}Mn_{22}Ga_{25}$ polycrystalline alloy with the coexistence of the three concerned phases at room temperature, *i.e.* the parent austenite, the modulated martenstie and the non-modulated martensite. The microstructural evolution during the two-step phase transformation was examined by electron backscatter diffraction (EBSD). Based on the direct experimental data, the transformation path, the microstructure change in couple with the crystal structure change during the transformation and its constraints on the transformation path and the shape memory effect were unambiguously clarified.

4.3.1 EBSD measurements on the co-existing austenite, 7M martensite and NM martensite

Fig.4.13a shows the EBSD phase micrograph covering the co-existing austenite, incommensurate 7M martensite and NM martensite in the same initial austenite. The 7M and the NM martensite are in plate-shape and the neighboring 7M and NM plates stretch in roughly the same direction. In general, the plates of the 7M martensite are thinner than those of the NM martensite. When approaching the NM martensite, some 7M plates tend to thicken and the width of 7M plates is close to that of NM plates, indicating that the transformation from 7M to NM martensite is accompanied by a reduction of the specific area of the NM plate interface. This

tendency suggests that the plate interfacial energy of the NM martensite is higher than that of the 7M martensite. By thickening the plates, the total interfacial area is reduced and thus the interfacial energy is lowered.

Fig. 4.13b shows the EBSD orientation micrograph corresponding to Fig.4.13a. The three phases are colored according to their orientations. It is seen that for the 7M martensite there are 4 orientation variants, whereas for the NM martensite, it seems that one plate corresponds to one orientation variant but in reality it is composed of alternatively distributed two fine lamellae, as displayed in Fig. 4.14a. Of the two lamellae, one is thinner than the other so that the thickness of the thinner one is beyond the resolution of the present automated EBSD orientation mapping. Representing the orientation of NM plate with the orientation of the thicker lamellae, one can find 4 plate variants, as shown in Fig. 4.13b. Considering that one NM plate is composed of two orientation variants, we can obtain, in total, 8 orientation variants for NM martensite.

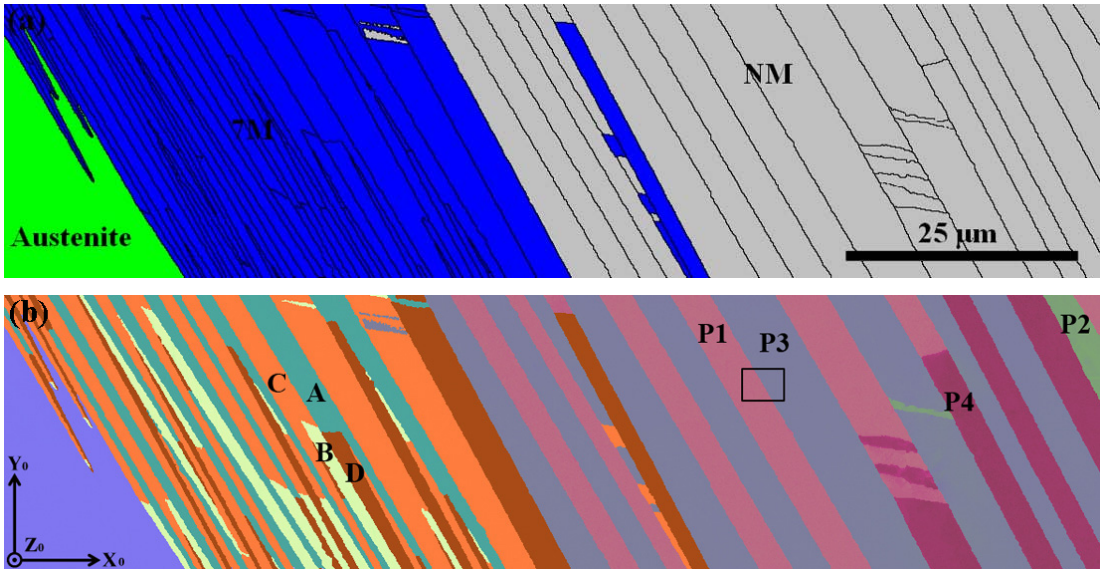

Fig 4.13 (a) EBSD phase index map of the coexisted austenite, 7M(IC) and NM martensite in the same austenite grain; (b) EBSD orientation map, four 7M variants are designated as A, B, C and D; four NM plates are nominated as P1, P2, P3 and P4. The coordinate frame (X_0-Y_0-Z_0) refers to the macroscopic sample coordinate system.

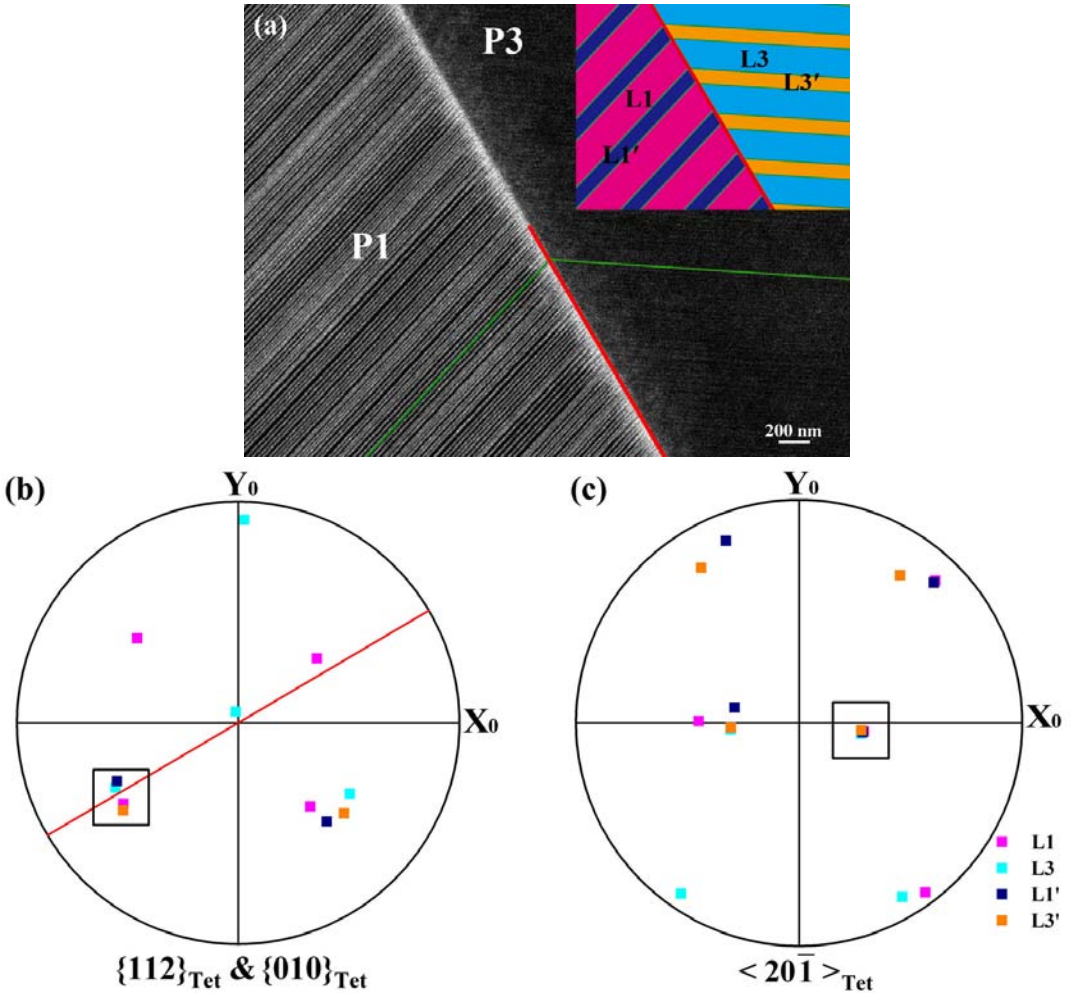

Fig.4.14 (a) Zoomed BSE image of the squared region in Fig.4.13b showing the fine lamellae in plate P1 and P3 of NM martensite. The paired fine lamellae in two plates are denoted as L1, L1′, L3 and L3′, respectively, as shown in the inset schema. L1 and L3 represent the thicker lamellae, and L1′ and L3′ the thinner lamellae. The red and green lines represent the traces of inter-plate interface and $(112)_{Tet}$ twinning interface. (b) $\{112\}_{Tet}$ pole figure of the two thick lamellae (L1 and L3) and $\{010\}_{Tet}$ pole figure of the two thin lamellae (L1′ and L3′). The red line represents the trace of the plate interface normal. (c) $<20\bar{1}>_{Tet}$ pole figure of the four fine lamellae in plate P1 and P3.

For the tetragonal NM martensite as analyzed above, the neighboring fine lamellae in each plate are also found to be compound twin related with the $(112)_{Tet}$ as the twinning plane and the $[11\bar{1}]_{Tet}$ the twinning direction. The full twinning elements are given in Table 4.6. The inter-lamellar interfaces (as marked with green line in Fig.4.13a) were determined to be the twinning planes ($(112)_{Tet}$) and thus coherent.

At the inter-plate interfaces of NM martensite (as marked with red line in Fig.4.14a), two thick lamellae and two thin lamellae from neighboring plates intersect. When the thick lamellae meet, *i.e.* L1 and L3, as illustrated at the right upper corner of Fig. 4.14a, they appear to have $(1\bar{1}2)_{Tet}$ $[\bar{1}11]_{Tet}$ twin relationship but with a certain degrees of deviation in the twinning plane and in the twinning direction. The angular deviations calculated using the experimental orientation data are 5.91° between the twinning planes and 3.89° between the twinning directions, respectively. Further calculation manifests that the plate interface of the NM martensite is oriented close to the $(1\bar{1}2)_{Tet}$ planes of the thick lamellae with ~3° deviation. Using $(1\bar{1}2)_{Tet}$ that defines the orientation of the plate interface as reference, the closest planes of the thin lamellae (L1′ and L3′) from the neighboring plates (P1 and P3) are $(010)_{L1'}$ and $(010)_{L3'}$. The closest in-plane directions of the four lamellae (L1 & L3 and L1′ & L3′) are found to be $[20\bar{1}]_{Tet}$ that are developed from the $[210]_{7M}$ of the 7M martensite. The geometrical configuration of these planes and directions that can be used to figure out the plate interface is displayed with their pole figures in Fig. 4.14b (plane pole figure) and Fig. 4.14c (direction pole figure). The projection of the plate interface normal (the red straight line) is displayed in the plane pole figure (Fig. 4.14b). The corresponding plane and direction poles are enclosed in the open squares in the pole figures and their deviations are given in Table 4.6. It is seen that the parallelisms are far from perfect, especially those of the planes. With such large degrees of deviations, elastic displacement of atoms from their equilibrium positions in vicinity of the interface area could be expected. This large mismatch on the plate interfaces surely imposes significant constraint on the transformation direct from austenite to NM martensite and this might be the reason for the formation of the 7M martensite at the intermediate state of the transformation to mitigate the transformation constraint.

Table 4.6 Orientation relationships between the NM fine lamellae connected by inter-plate interface between plate P1 and P3. The orientation data of the thin lamellae were acquired manually by EBSD measurement.

	Orientation relationship	
L1/L3′	twin-related	$K_1=(112)_{Tet}$;$K_2=(11\bar{2})_{Tet}$;
L3/L3′	twin-related	$\eta_1=[11\bar{1}]_{Tet}$; $\eta_2=[111]_{Tet}$; s=0.344
L1/L3	$(1\bar{1}2)_{L1}$ 5.91° from $(1\bar{1}2)_{L3}$	$[20\bar{1}]_{L1}$ 1.62° from $[20\bar{1}]_{L3}$
L1′/L3′	$(010)_{L1'}$ 11.05° from $(010)_{L3'}$	$[20\bar{1}]_{L1'}$ 1.07° from $[20\bar{1}]_{L3'}$
L1′/L3	$(010)_{L1'}$ 2.70° from $(1\bar{1}2)_{L3}$	$[20\bar{1}]_{L1'}$ 0.97° from $[20\bar{1}]_{L3}$

4.3.2 Orientation relationship between 7M martensite and NM martensite

To further precisely reveal the transformation process and the atomic arrangements of the 7M and the NM plate interfaces, the OR between the 7M and the NM martensites were determined. Calculations show that the 7M martensite and the NM martensite possess a specific OR with $(001)_{7M}//(112)_{Tet}$ and $[100]_{7M}//[11\bar{1}]_{Tet}$, *i.e.* the shuffling plane in one 7M variant is parallel to the twinning plane of its corresponding NM lamellae and the shuffling direction is parallel to the twinning direction. The OR secures a one-to-one correspondence between the 7M plate and the NM plate, as displayed in Fig. 4.15, where the 7M and NM martensite coexist in the same plate. In the figure, the 7M martensite and the NM martensite clearly displays different contrasts due to their different crystal structures. In the plate, the traces of the shuffling planes of the 7M are parallel to those of the twinning planes of the NM. With such an OR, variant A of 7M martensite transforms to plate P1 of NM martensite (Fig. 4.15), variant B to P2, variant C to P3 and variant D to P4.

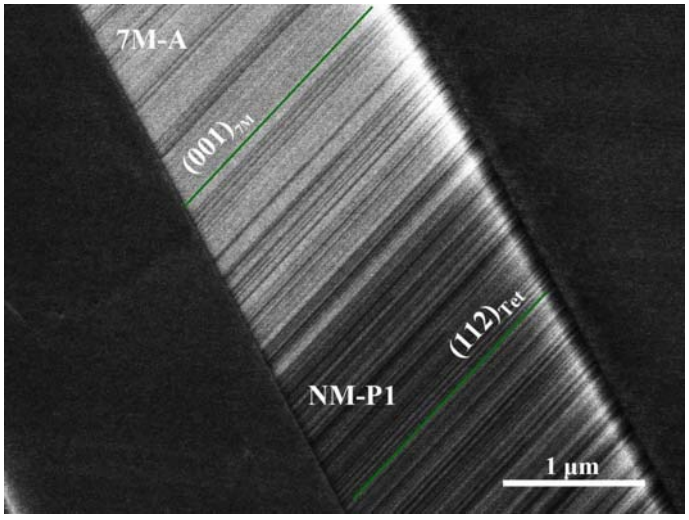

Fig.4.15 BSE image showing the transition from 7M variant A to NM plate P1.

4.3.3 Transformation mechanism from 7M martensite to NM martensite

The present experimental results allow evidencing the transformation sequence from austenite to NM martensite bridged by the 7M martensite and the microstructure evolution during this phase transition. The intrinsic OR between the 7M and NM martensites with $(001)_{7M}$ //$(112)_{Tet}$ and $[100]_{7M}$//$[11\bar{1}]_{Tet}$ indicates that the structure change from the 7M (monoclinic) to the NM (tetragonal) can be viewed as further reshuffling of the atoms on the $(001)_{7M}$ along the $[100]_{7M}$ or the $[\bar{1}00]_{7M}$ direction. As the crystal structure of the 7M is different from that of the NM, the reshuffling should also be accompanied with certain distortion of these planes and their interplanar distance. Consequently, one 7M variant finally transforms to one NM plate composed of paired twin-related fine variants. Four 7M variants correspond to 8 NM lamellae.

Based on such an ideal OR between the two phases, the plate interfaces of the 7M and the NM martensite was reconstructed to further reveal the structure change at the plate interface during this phase transition. As an example, Fig. 4.16 displays the atomic correspondence of the plate interface between variant A and C (type I twin) of 7M martensite and the plate interface between plate P1 and P3 of NM martensite following the transformation OR. It is seen from Fig. 4.16a that although some of the atoms on the interface are slightly deviated from their exact equilibrium position due to the structure modulation, the 7M plate interface is basically coherent. Therefore, the interfacial energy should be relatively low. However, when the 7M plates transforms to the NM, the misfit at the interface becomes non neglectable, as shown in Fig. 4.16b. The plate interface thus becomes non-coherent. This atomic misfit will surely result in high interfacial energy and thus contributes as energy barrier to the transformation. It is due to this high atomic misfit that the 7M to NM transformation is accompanied by the thickening of the NM martensite plates, which can reduce the specific interfacial area of the NM martensite and thus lower the total interfacial energy of NM plates, as evidenced in Fig. 4.13. Therefore, the 7M modulated structure is advantageous in the plate interfacial energy.

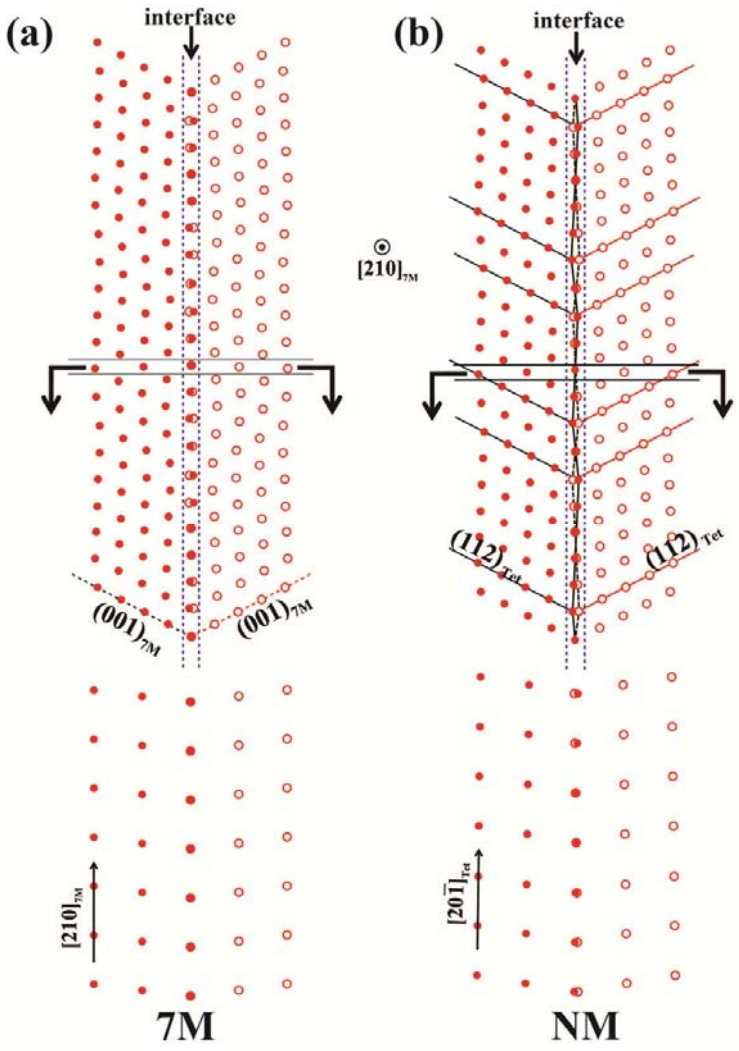

Fig.4.16 Atomic projection of (a) the type I twin interface in $[210]_{7M}$ and their cross section atomic correspondences for 7M martensite; (b) the corresponding inter-plate interface of NM martensite and their cross section atomic correspondences.

Another energetically advantage of the 7M modulated structure is that it offers smaller lattice distortion with respect to the parent lattice. This lattice distortion can be quantified with the corresponding stress-free strain tensors [130] for the transformation from the austenite to the 7M martensite and from the austenite directly to the NM martensite. The non-zero terms in these tensors (ε_{11}, ε_{22}, ε_{33}, γ) are shown in Table 4.7. It is clear that the lattice distortion accompanying the transformation from the cubic austenite to the tetragonal martensite is much larger than that occurring in the transformation from the austenite to the 7M martensite. This lattice distortion gives rise to volume dependent elastic energy that contributes as energy barrier to the

transformation. Together with the large plate interfacial energy, this volume dependent elastic energy imposes insurmountable barriers to the transformation from the austenite to the normal tetragonal martensite (NM martensite). Therefore, the formation of the intermediate 7M modulated phase is unavoidable in bridging the parent austenite to the final NM martensite and thus a two-step lattice distortion is experienced in the transformation from the austenite to the NM martensite.

Table 4.7 Strain tensors between matrix and product phases for austenite to 7M, austenite to NM and 7M to NM transformation.

	Austenite - 7M	Austenite - NM	7M-NM
ε_{11}	0.0275	-0.0560	0.0083
ε_{22}	-0.0472	0.1204	-0.0092
ε_{33}	0.0207	-0.0560	0.0002
γ	-0.0446	0	0.0252

From the microstructural configurations of the two kinds of martensite, it is clear that the reorientation of the 7M plates (variants) that gives rise to the shape memory effect is much easier than those of the NM. For 7M, there are 2 advantages. First, 7M plate corresponds to one orientation variant and the plate interface is coherent. Second, the shear system possessing a uniform and much smaller twinning shear is parallel to the plate interface. If we can obtain only two alternately distributed variants, the magnetic field can easily reorient one variant to the other by twinning or detwinning through plate interface movement. In contrast, the situation in the NM configuration is very different. Two NM plates correspond to four orientation variants (lamellae). The inter-plate interfaces and the lamellar interfaces are in an inter-pinned position. Moreover, the twinning system is not consistent with the plate interface and the twinning shear of the lamellar variants is much higher. Clearly, the pinning of the interfaces, the large atomic mismatch at the plate interface and the much larger twinning shear all act as plate or lamellae reorientation resistance. In such a context, it is not difficult to understand why modulated martensite of Ni-Mn-Ga alloys offers superior magnetic field induced reversible shape change; whereas the tetragonal martensite does not as have been demonstrated by many experiments [89].

As the 7M modulated martensite of Ni-Mn-Ga alloys is essentially important for the field induced shape memory applications, its thermodynamic metastablility has become a critical issue for the development of the Ni-Mn-Ga alloys. Its existing temperature window is of particular importance. Measures should be taken to enlarge this temperature window. From the examinations of the transformation path and the possible energy barriers in this study, it is seen that the lattice misfit between the 7M and NM (Table 4.7) and the atomic mismatch on the NM plate interfaces can be the controlling factors to postpone the 7M to NM transformation, hence enlarge the existing temperature range of 7M. This could be achieved by adjusting the composition or by alloying new elements.

4.3.4 Summary

In summary, we clarified the roles of the Ni-Mn-Ga 7M modulated martensite in the transformation from the cubic austenite to the tetragonal NM martensite through crystal structure, crystallographic orientation and microstructure examinations. In this transformation, the lattice mismatch between the cubic austenite and the tetragonal NM martensite and the formation of incoherent NM plate interfaces represent as an insurmountable energy barrier for a direct transformation from the austenite to the NM martensite. The formation of 7M modulated martensite is evidenced as an intermediate step in this transformation by introducing an intermediate crystal structure that greatly mitigates the large lattice mismatch and by forming coherent plate interfaces. During this two step transformation, one austenite variant will gives rise to 4 twin related 7M orientation variants and one 7M variant will result in 2 twin related NM variants, correspondingly 8 NM orientation variants in total. The transformation from the 7M to the NM martensite is realized by lattice distortion following the $(001)_{7M}$ //$(112)_{Tet}$ and $[100]_{7M}$ // $[11\bar{1}]_{Tet}$ OR, which is accompanied by the degradation of the atom coherency in the vicinity of the NM plate interface and the complete change of twin configuration. This microstructure change is well correlated with the experimentally observed field induced shape memory performance

degradation from 7M to NM. The available temperature window for the stable existence of the 7M martensite depends on the energy barriers related to the lattice mismatch between the 7M and the NM martensite and the atomic misfit on the plate interfaces of the NM martensite.

Chapter 5 Conclusion and perspective

Conclusion

In this dissertation, four off-stoichiometric Ni-Mn-Ga polycrystalline alloys were deliberately prepared. The microstructure and martensitic transformation features were thoroughly investigated. Through this dissertation, it has been demonstrated that the EBSD technique can be used as an advanced characterization tool for accurate crystallographic analyses for materials having modulated superstructure. The conclusions of the present study are summarized as follows:

(1) $Ni_{50}Mn_{28}Ga_{22}$ alloy:

The martensite possesses a monoclinic 5M modulated superstructure, the superlattice of which is composed of 5 subcells. The microstructure of the 5M martensite can be characterized by broad plates with alternatively distributed fine variants. EBSD measurements using the monoclinic superstructure information revealed four twin-related variants A, B, C and D with distinct orientations in one broad plate, *i.e.* the variant pair A:C (or B:D) has the relation of type I twin, A:B (or C:D) type II twin, and A:D (or B and C) compound twin. The variant interfaces were revealed to be the corresponding twinning planes (K_1). Based on the local orientations of the individual martensite variants measured by EBSD system and crystallographic calculation, the more favorable transformation OR from austenite to 5M martensite was revealed to be the Pitsch relation with $(101)_A//(1\bar{2}\bar{5})_{5M}$ and $[10\bar{1}]_A//[\bar{5}\bar{5}1]_{5M}$ with no residual austenite.

(2) $Ni_{50}Mn_{30}Ga_{20}$ alloy:

It is confirmed by Kikuchi pattern indexation that 7M martensite possesses an incommensurate monoclinic superstructure and the superlattice is composed of ten subcells. From a parent austenite grain, one or several martensite colonies are inherited, each consisting of 4 types of twin-related variants (A, B, C, and D)

according to EBSD measurements. All the pairs of variants can be categorized into three twinning modes: variants A and C (or B and D) are in type I twin relation, variants A and B (or C and D) type II twin, and variants A and D (or B and C) compound twin. All the twin interfaces are in coincidence with the respective twinning plane (K_1). Furthermore, based on the local orientations of individual martensite variants measured by EBSD system and detailed crystallographic analysis, the energetically favorable OR governing the austenite to incommensurate 7M martensite transformation was revealed to be the Pitsch relation with $(1\ 0\ 1)_A//(1\ \bar{2}\ \overline{10})_{7M}$ and $[1\ 0\ \bar{1}]_A//[\overline{10}\ \ \overline{10}\ \ 1]_{7M}$. Under this determined OR, at most 24 physically distinct martensite variants may be resulted from an initial austenite grain during the martensitic transformation. Notably, in the present work, the first attempt has been made to resolve the ambiguity of the geometrically favorable ORs by examining the lattice discontinuity caused by the phase transformation and the structural modulation.

(3) $Ni_{54}Mn_{24}Ga_{22}$ alloy:

The alloys are composed of self-accommodated NM martensitic plates with tetragonal crystal structure. The adjacent plates have the relationship of 80°~85° rotation around the $<110>_{Tet}$ axes. Locally, four types of plates are identified and each plate consists of paired fine variants. Totally, eight orientation variants are found in one martensite colony. The paired fine variants in each plate were found to be compound twin related with the $\{112\}_{Tet}$ as the twinning plane and the $<11\bar{1}>_T$ the twinning direction. The inter-plate interfaces are close to $\{1\bar{1}2\}_{Tet}$ plane but with ~3° deviation, while the interfaces of two paired fine variants are in good agreement with $\{112\}_{Tet}$ twinning plane.

(4) $Ni_{53}Mn_{22}Ga_{25}$ alloy:

At room temperature, austenite and martensite co-exist in $Ni_{53}Mn_{22}Ga_{25}$ alloy. The formation of the characteristic diamond-like martensite microstructure with four variants (A, B, C and D) during the austenite-7M martensite transformation was evidenced. As revealed by EBSD measurements, the martensite “diamond” consists of type I twin (A:C and B:D pair) and compound twin (A:D and B:C pair); the long ridge

of martensite “diamond” corresponds to type I twin interface and the short ridge to compound twin interface. The “diamonds” finally transforms into martensite plates. The favorable way for the “diamond” growth is through the forward of spears. Crystallographic calculation manifests that the characteristic four variants in a “diamond” group clustered around one $\{101\}_A$ pole and the elastic strains around martensite were effectively cancelled out by making such a group. Both A:C (or B:D) and A:B (or C:D) variant pairs are self-accommodated; while A:D (or B:D) variant pair is not.

The microstructure with co-existing three phases (austenite, modulated martensite and final NM martensite) was observed in some austenite grains. Three phases are located with a fixed adjacency, *i.e.* austenite – modulated martensite – NM martensite. The long-period 7M martensite occurs on cooling as a thermodynamically metastable phase that is intermediate between the parent austenite and the final stable NM martensite. The modulated martensite phase possesses an independent crystal structure, rather than the nanotwin combination of the normal non-modulated martensite proposed by the nanotwin combination theory. The modulated structure of 7M martensite provides reduced local number of variants and favors twinning and detwinning configuration. This is essential to the attainability of the magnetic field induced shape change.

The role of 7M martensite in the transformation from the cubic austenite to the tetragonal NM martensite has been clarified. In this transformation, the lattice mismatch between the cubic austenite and the tetragonal NM martensite and the formation of the incoherent NM plate interfaces represent as an insurmountable energy barrier for a direct transformation from the austenite to the NM martensite. The formation of 7M modulated martensite is evidenced as an intermediate step in this transformation by introducing an intermediate crystal structure that greatly mitigates the large lattice mismatch and by forming coherent plate interfaces. During this two step transformation, one austenite variant will gives rise to 4 twin related 7M orientation variants and one 7M variant will result in 2 twin related NM variants, correspondingly 8 NM orientation variants in total. The transformation from the 7M

to the NM martensite is realized by lattice distortion following the $(001)_{7M}$ // $(112)_{Tet}$ and $[100]_{7M}$ // $[11\bar{1}]_{Tet}$ OR, which is accompanied by the degradation of the atom coherency in the vicinity of the NM plate interface and the complete change of twin configuration. This microstructure change is well correlated with the experimentally observed field induced shape memory performance degradation from in NM state. The available temperature window for the stable existence of the 7M martensite depends on the energy barriers related to the lattice mismatch between the 7M and the NM martensite and the atomic misfit on the plate interfaces of the NM martensite.

Perspective

Since Ni-Mn-Ga ferromagnetic shape memory alloys are newly developed system, there are still some research margins. In these alloys, giant magnetic field induced strains were only obtained in the bulk single crystals with modulated structure. Due to the complexity of producing single crystal, the high fabricating cost and the severe composition segregation hinder their practical application. In contrast, the manufacture of polycrystalline alloys is much simpler and easier to be implemented in practical production, but the randomness of the crystallographic orientation of the polycrystalline alloys leads to the loss of the magnetic shape memory performance. Texturation of polycrystalline alloys has become a promising way to improve the shape memory performance comparable to that of the single crystal. To achieve this goal, it is necessary to introduce innovative fabricating routes or external field training processes.

Moreover, the low blocking stress and the intrinsic brittleness of Ni-Mn-Ga alloys act as a great hindrance to the practical applications. To increase the blocking stress and improve the ductility, appropriate alloying is quite necessary.

Since the inter-variant interfaces are crucial for the magnetic shape memory effect, further work should pay more attention on revealing the details of inter-variant interface by considering the lattice modulation. Therefore, detailed TEM or HRTEM characterizations of the interface structure are needed.

Appendix I: atomic coordinates of 5M superstructure

a_{5M} = 4.226 Å; b_{5M} = 5.581 Å; c_{5M} = 21.052 Å; β = *90.3*°; space group: *P2/m* (*No.* 10)

Atom type	Wyck. position	x	y	z
Mn	*1a*	0	0	0
Mn	*2m*	0.948	0	0.4
Mn	*2m*	0.044	0	0.2
Mn	*2n*	0.552	0.5	0.1
Mn	*2n*	0.456	0.5	0.3
Mn	*1h*	0.5	0.5	0.5
Ni	*2j*	0.5	0.25	0
Ni	*4o*	0.052	0.25	0.1
Ni	*4o*	0.544	0.25	0.2
Ni	*4o*	0.956	0.25	0.3
Ni	*4o*	0.448	0.25	0.4
Ni	*2k*	0	0.25	0.5
Ga	*1b*	0	0.5	0
Ga	*2m*	0.552	0	0.1
Ga	*2n*	0.044	0.5	0.2
Ga	*2m*	0.456	0	0.3
Ga	*2n*	0.948	0.5	0.4
Ga	*1g*	0.5	0	0.5

Appendix II: atomic coordinates of incommensurate 7M superstructure

a_{7M} = 4.2651 Å; b_{7M} = 5.5114 Å; c_{7M} = 42.365 Å; β = 93.27°; space group: *P2/m* (*No.* 10)

Atom type	Wyck. position	x	y	z
Mn	*1a*	0	0	0
Mn	*1c*	0	0	0.5
Mn	*2m*	0.066	0	0.1004
Mn	*2m*	-0.02139	0	0.1996
Mn	*2m*	-0.0848	0	0.3000
Mn	*2m*	0.1055	0	0.4002
Mn	*2n*	0.605	0.5	0.0501
Mn	*2n*	0.5083	0.5	0.1502
Mn	*2n*	0.4096	0.5	0.2496
Mn	*2n*	0.5475	0.5	0.3499
Mn	*2n*	0.5414	0.5	0.4505
Ga	*1b*	0	0.5	0
Ga	*1f*	0	0.5	0.5
Ga	*2n*	0.066	0.5	0.1004
Ga	*2n*	-0.02139	0.5	0.1996
Ga	*2n*	-0.0848	0.5	0.3000
Ga	*2n*	0.1055	0.5	0.4002
Ga	*2m*	0.605	0	0.0501
Ga	*2m*	0.5083	0	0.1502
Ga	*2m*	0.4096	0	0.2496
Ga	*2m*	0.5475	0	0.3499
Ga	*2m*	0.5414	0	0.4505
Ni	*2l*	0.5	0.75	0.5
Ni	*2j*	0.5	0.75	0
Ni	*4o*	0.1056	0.25	0.0501
Ni	*4o*	0.0075	0.25	0.1502
Ni	*4o*	-0.0920	0.25	0.2496
Ni	*4o*	0.0511	0.25	0.3499
Ni	*4o*	0.0395	0.25	0.4505
Ni	*4o*	0.5663	0.75	0.1004
Ni	*4o*	0.4786	0.75	0.1996
Ni	*4o*	0.4151	0.75	0.3000
Ni	*4o*	0.6055	0.75	0.4002

Appendix III: atomic coordinates of nanotwinned 7M superstructure

a_{ad} = 4.257 Å; b_{ad} = 5.486 Å; c_{ad} = 29.446 Å; β_{ad} = 94.2°; space group: *PM* (*No.* 6)

Atom type	Wyck. position	x	y	z
Mn	*1a*	0	0	0
Mn	*1b*	0.4518	0.5	0.0714
Mn	*1a*	-0.0965	0	0.1429
Mn	*1b*	0.3553	0.5	0.2143
Mn	*1a*	-0.1930	0	0.2857
Mn	*1b*	0.2588	0.5	0.3571
Mn	*1a*	-0.1206	0	0.4286
Mn	*1b*	0.5	0.5	0.5
Mn	*1a*	-0.0482	0	0.5714
Mn	*1b*	0.4035	0.5	0.6429
Mn	*1a*	-0.1447	0	0.7143
Mn	*1b*	0.3070	0.5	0.7857
Mn	*1a*	-0.2412	0	0.8571
Mn	*1b*	0.3794	0.5	0.9286
Ga	*1b*	0	0.5	0
Ga	*1a*	0.4518	0	0.0714
Ga	*1b*	-0.0965	0.5	0.1429
Ga	*1a*	0.3553	0	0.2143
Ga	*1b*	-0.1930	0.5	0.2857
Ga	*1a*	0.2588	0	0.3571
Ga	*1b*	-0.1206	0.5	0.4286
Ga	*1a*	0.5	0	0.5
Ga	*1b*	-0.0482	0.5	0.5714
Ga	*1a*	0.4035	0	0.6429
Ga	*1b*	-0.1447	0.5	0.7143
Ga	*1a*	0.3070	0	0.7857
Ga	*1b*	-0.2412	0.5	0.8571
Ga	*1a*	0.3794	0	0.9286
Ni	*2c*	0.5	0.25	0
Ni	*2c*	-0.0482	0.25	0.0714
Ni	*2c*	0.4035	0.25	0.1429
Ni	*2c*	-0.1447	0.25	0.2143
Ni	*2c*	0.3070	0.25	0.2857
Ni	*2c*	-0.2412	0.25	0.3571
Ni	*2c*	0.3794	0.25	0.4286
Ni	*2c*	0	0.25	0.5
Ni	*2c*	0.4517	0.25	0.5714

Ni	*2c*	-0.0965	0.25	0.6429
Ni	*2c*	0.3553	0.25	0.7143
Ni	*2c*	-0.1930	0.25	0.7857
Ni	*2c*	0.2588	0.25	0.8571
Ni	*2c*	-0.1206	0.25	0.9286

References

[1] A.G. Olabi, A. Grunwald, Materials & Design, 29 (2008) 469-483.

[2] K. Otsuka, X. Ren, Intermetallics, 7 (1999) 511-528.

[3] X.L. Zhao, H.D. Gao, G.F. Zhang, B. Ayhan, F. Yan, C. Kwan, J.L. Rose, Smart Materials & Structures, 16 (2007) 1208-1217.

[4] G. Song, V. Sethi, H.N. Li, Engineering Structures, 28 (2006) 1513-1524.

[5] M.J. Hoffmann, H. Kungl, Current Opinion in Solid State and Materials Science, 8 (2004) 51-57.

[6] M.M. Schwartz, Encyclopedia of smart materials, J. Wiley, New York, 2002.

[7] K. Ullakko, J.K. Huang, C. Kantner, R.C. Ohandley, V.V. Kokorin, Appl. Phys. Lett., 69 (1996) 1966-1968.

[8] A. Sozinov, A.A. Likhachev, N. Lanska, K. Ullakko, Appl. Phys. Lett., 80 (2002) 1746.

[9] C.P. Henry, D. Bono, J. Feuchtwanger, S.M. Allen, R.C. O'Handley, Journal of Applied Physics, 91 (2002) 7810-7811.

[10] R.C. O'Handley, S.J. Murray, M. Marioni, H. Nembach, S.M. Allen, Journal of Applied Physics, 87 (2000) 4712-4717.

[11] T. Yamamoto, M. Taya, Appl. Phys. Lett., 90 (2007) 251905-251903.

[12] T. Omori, K. Watanabe, R.Y. Umetsu, R. Kainuma, K. Ishida, Appl. Phys. Lett., 95 (2009) 082508-082503.

[13] R. Kainuma, Y. Imano, W. Ito, Y. Sutou, H. Morito, S. Okamoto, O. Kitakami, K. Oikawa, A. Fujita, T. Kanomata, K. Ishida, Nature, 439 (2006) 957-960.

[14] R. Kainuma, Y. Imano, W. Ito, H. Morito, Y. Sutou, K. Oikawa, A. Fujita, K. Ishida, S. Okamoto, O. Kitakami, T. Kanomata, Appl. Phys. Lett., 88 (2006) 192513-192513.

[15] S.J. Murray, M. Marioni, S.M. Allen, R.C. O'Handley, T.A. Lograsso, Appl. Phys. Lett., 77 (2000) 886-888.

[16] G. Olson, M. Cohen, Metallurgical and Materials Transactions A, 13 (1982) 1907-1914.

[17] E. Patoor, D.C. Lagoudas, P.B. Entchev, L.C. Brinson, X. Gao, Mechanics of Materials, 38 (2006) 391-429.

[18] K. Otsuka, C.M. Wayman, Shape memory materials, Cambridge University Press, Cambridge; New York, 1998.

[19] J.L. Macqueron, M. Morin, G. Guenin, A. Planes, J. Elgueta, T. Castan, Journal De Physique IV, 1 (1991) 259-263.

[20] L. Delaey, Diffusionless Transformations, Wiley-VCH Verlag GmbH & Co. KGaA, 2005.

[21] P.J. Webster, K.R.A. Ziebeck, S.L. Town, M.S. Peak, Philosophical Magazine Part B, 49 (1984) 295 - 310.

[22] E.C. Bain, Transactions of the American Institute of Mining and Metallurgical Engineers, 70 (1924) 25-46.

[23] M.S. Wechsler, D.S. Lieberman, T.A. Read, Transactions of the American Institute of Mining and Metallurgical Engineers, 197 (1953) 1503-1515.

[24] J.S. Bowles, J.K. Mackenzie, Acta Metallurgica, 2 (1954) 129-137.

[25] J.W. Christian, Journal of the Institute of Metals, 84 (1956) 386-394.

[26] G. Kurdjumow, G. Sachs, Zeitschrift für Physik A Hadrons and Nuclei, 64 (1930) 325-343.

[27] Z. Nishiyama, Science Reports of Tohoku Imperial University, 23 (1934) 637-664.
[28] G. Wassermann, Mitt. K.-Wilh.-Inst. Eisenforsch, 17 (1935) 149-155.
[29] A.B. Greninger, A.R. Troiano, Transactions of the American Institute of Mining and Metallurgical Engineers, 185 (1949) 590-598.
[30] W. Pitsch, Acta Metallurgica, 10 (1962) 897- 900.
[31] J.W. Christian, The theory of transformations in metals and alloys PERGAMON, 2002.
[32] J.W. Christian, S. Mahajan, Progress in Materials Science, 39 (1995) 1-157.
[33] Y. Zhang, Z. Li, C. Esling, J. Muller, X. Zhao, L. Zuo, Journal of Applied Crystallography, 43 (2010) 1426-1430.
[34] F.A. Hames, Journal of Applied Physics, 31 (1960) S370-S371.
[35] M. Elfazani, M. Demarco, S. Jha, G.M. Julian, J.W. Blue, Journal of Applied Physics, 52 (1981) 2043-2045.
[36] C. Mitros, S. Yehia, S. Kumar, S. Jha, M. Demarco, D. Mitchell, G.M. Julian, R.A. Dunlap, Hyperfine Interactions, 34 (1987) 419-422.
[37] T. Kanomata, K. Shirakawa, T. Kaneko, Journal of Magnetism and Magnetic Materials, 65 (1987) 76-82.
[38] J. Soltys, Acta Physica Polonica A, A 47 (1975) 521-523.
[39] V.V. Kokorin, V.A. Chernenko, Fizika Metallov I Metallovedenie, 68 (1989) 1157-1161.
[40] V.V. Kokorin, V.V. Martynov, V.A. Chernenko, Scripta Metallurgica et Materialia, 26 (1992) 175-177.
[41] V.A. Chernenko, E. Cesari, V.V. Kokorin, I.N. Vitenko, Scripta Metallurgica et Materialia, 33 (1995) 1239-1244.
[42] V.A. Chernenko, R.L. Anton, M. Kohl, J.M. Barandiaran, M. Ohtsuka, I. Orue, S. Besseghini, Acta Materialia, 54 (2006) 5461-5467.
[43] U. Gaitzsch, M. Potschke, S. Roth, B. Rellinghaus, L. Schultz, Acta Materialia, 57 (2009) 365-370.
[44] Y. Boonyongmaneerat, M. Chmielus, D.C. Dunand, P. Mullner, Physical Review Letters, 99 (2007).
[45] M. Chmielus, X.X. Zhang, C. Witherspoon, D.C. Dunand, P. Mullner, Nature Materials, 8 (2009) 863-866.
[46] P.J. Brown, J. Crangle, T. Kanomata, M. Matsmuoto, K.U. Neumann, B. Ouladdiaf, K.R.A. Ziebeck, Journal of Physics: Condensed Matter, 14 (2002) 10159-10171.
[47] V.V. Kokorin, V.A. Chernenko, E. Cesari, J. Pons, C. Segui, Journal of Physics: Condensed Matter, 8 (1996) 6457-6463.
[48] L. Manosa, A. GonzalezComas, E. Obrado, A. Planes, V.A. Chernenko, V.V. Kokorin, E. Cesari, Physical Review B, 55 (1997) 11068-11071.
[49] V.A. Chernenko, J. Pons, C. Seguí, E. Cesari, Acta Materialia, 50 (2002) 53-60.
[50] V.V. Khovailo, T. Takagi, A.D. Bozhko, M. Matsumoto, J. Tani, V.G. Shavrov, Journal of Physics: Condensed Matter, 13 (2001) 9655-9662.
[51] F. Zuo, X. Su, P. Zhang, G.C. Alexandrakis, F. Yang, K.H. Wu, Journal of Physics: Condensed Matter, 11 (1999) 2821-2830.
[52] V.A. Chernenko, S. Besseghini, T. Kanomata, H. Yoshida, T. Kakeshita, Scripta Materialia, 55 (2006) 303-306.
[53] A. Zheludev, S.M. Shapiro, P. Wochner, L.E. Tanner, Physical Review B, 54 (1996) 15045.

[54] U. Stuhr, P. Vorderwisch, V.V. Kokorin, P.A. Lindgard, Physical Review B, 56 (1997) 14360-14365.
[55] G. Fritsch, V.V. Kokorin, A. Kempf, Journal of Physics: Condensed Matter, 6 (1994) L107-L110.
[56] A. Planes, E. Obrado, A. GonzalezComas, L. Manosa, Physical Review Letters, 79 (1997) 3926-3929.
[57] M.A. Uijttewaal, T. Hickel, J. Neugebauer, M.E. Gruner, P. Entel, Physical Review Letters, 102 (2009) 035702.
[58] J. Enkovaara, A. Ayuela, A.T. Zayak, P. Ente, L. Nordstrom, M. Dube, J. Jalkanen, J. Impola, R.M. Nieminen, Materials Science and Engineering a-Structural Materials Properties Microstructure and Processing, 378 (2004) 52-60.
[59] V.V. Khovailo, T. Takagi, J. Tani, R.Z. Levitin, A.A. Cherechukin, M. Matsumoto, R. Note, Physical Review B, 65 (2002).
[60] C.B. Jiang, G. Feng, H.B. Xu, Appl. Phys. Lett., 80 (2002) 1619-1621.
[61] V.A. Chernenko, Scripta Materialia, 40 (1999) 523-527.
[62] X. Jin, M. Marioni, D. Bono, S.M. Allen, R.C. O'Handley, T.Y. Hsu, Journal of Applied Physics, 91 (2002) 8222-8224.
[63] C. Seguí, V.A. Chernenko, J. Pons, E. Cesari, V. Khovailo, T. Takagi, Acta Materialia, 53 (2005) 111-120.
[64] W.H. Wang, G.H. Wu, J.L. Chen, S.X. Gao, W.S. Zhan, G.H. Wen, X.X. Zhang, Appl. Phys. Lett., 79 (2001) 1148-1150.
[65] V.A. Chernenko, C. Segui, E. Cesari, J. Pons, V.V. Kokorin, Physical Review B, 57 (1998) 2659-2662.
[66] W.H. Wang, Z.H. Liu, J. Zhang, J.L. Chen, G.H. Wu, W.S. Zhan, T.S. Chin, G.H. Wen, X.X. Zhang, Physical Review B, 66 (2002) 052411.
[67] V.A. Chernenko, V.V. Kokorin, O.M. Babii, I.K. Zasimchuk, Intermetallics, 6 (1998) 29-34.
[68] O. Heczko, N. Lanska, O. Soderberg, K. Ullakko, Journal of Magnetism and Magnetic Materials, 242-245 (2002) 1446-1449.
[69] D.Y. Cong, P. Zetterstrom, Y.D. Wang, R. Delaplane, R.L. Peng, X. Zhao, L. Zuo, Appl. Phys. Lett., 87 (2005).
[70] J. Pons, V.A. Chernenko, R. Santamarta, E. Cesari, Acta Materialia, 48 (2000) 3027-3038.
[71] K. Otsuka, T. Ohba, M. Tokonami, C.M. Wayman, Scripta Metallurgica et Materialia, 29 (1993) 1359-1364.
[72] V.V. Martynov, V.V. Kokorin, Journal De Physique III, 2 (1992) 739-749.
[73] Y.L. Ge, in: Helsinki University of Technology, Helsinki University of Technology, Finland, 2007.
[74] L. Righi, F. Albertini, L. Pareti, A. Paoluzi, G. Calestani, Acta Materialia, 55 (2007) 5237-5245.
[75] L. Righi, F. Albertini, E. Villa, A. Paoluzi, G. Calestani, V. Chernenko, S. Besseghini, C. Ritter, F. Passaretti, Acta Materialia, 56 (2008) 4529-4535.
[76] V.V. Martynov, Journal De Physique Iv, 5 (1995) 91-99.
[77] B. Wedel, M. Suzuki, Y. Murakami, C. Wedel, T. Suzuki, D. Shindo, K. Itagaki, Journal of Alloys and Compounds, 290 (1999) 137-143.
[78] A. Zheludev, S.M. Shapiro, P. Wochner, L.E. Tanner, Physical Review B, 54 (1996) 15045.
[79] L. Righi, F. Albertini, G. Calestani, L. Pareti, A. Paoluzi, C. Ritter, P.A. Algarabel, L. Morellon, M. Ricardo Ibarra, Journal of Solid State Chemistry, 179 (2006) 3525-3533.

[80] I. Glavatskyy, N. Glavatska, I. Urubkov, J.U. Hoffman, F. Bourdarot, Materials Science and Engineering: A, 481-482 (2008) 298-301.
[81] S. Kaufmann, U.K. Rößler, O. Heczko, M. Wuttig, J. Buschbeck, L. Schultz, S. Fähler, Physical Review Letters, 104 (2010) 145702.
[82] A. Ayuela, J. Enkovaara, R.M. Nieminen, Journal of Physics: Condensed Matter, 14 (2002) 5325-5336.
[83] A. Ayuela, J. Enkovaara, K. Ullakko, R.M. Nieminen, Journal of Physics: Condensed Matter, 11 (1999) 2017-2026.
[84] R. Tickle, R.D. James, Journal of Magnetism and Magnetic Materials, 195 (1999) 627-638.
[85] L. Straka, O. Heczko, Journal of Applied Physics, 93 (2003) 8636-8638.
[86] O. Heczko, L. Straka, N. Lanska, K. Ullakko, J. Enkovaara, Journal of Applied Physics, 91 (2002) 8228-8230.
[87] F. Albertini, L. Pareti, A. Paoluzi, L. Morellon, P.A. Algarabel, M.R. Ibarra, L. Righi, Appl. Phys. Lett., 81 (2002) 4032-4034.
[88] O. Heczko, Journal of Magnetism and Magnetic Materials, 290-291 (2005) 787-794.
[89] A. Sozinov, A.A. Likhachev, K. Ullakko, IEEE Transactions on Magnetics, 38 (2002) 2814-2816.
[90] P. Müllner, V.A. Chernenko, G. Kostorz, Journal of Applied Physics, 95 (2004) 1531-1536.
[91] H.E. Karaca, I. Karaman, B. Basaran, Y.I. Chumlyakov, H.J. Maier, Acta Materialia, 54 (2006) 233-245.
[92] O. Heczko, L. Straka, Materials Science and Engineering A, 378 (2004) 394-398.
[93] L. Straka, O. Heczko, S.P. Hannula, Scripta Materialia, 54 (2006) 1497-1500.
[94] R.D. James, R. Tickle, M. Wuttig, Materials Science and Engineering A, 273-275 (1999) 320-325.
[95] A. Sozinov, A.A. Likhachev, N. Lanska, O. Söderberg, K. Ullakko, V.K. Lindroos, Materials Science and Engineering A, 378 (2004) 399-402.
[96] L. Straka, O. Heczko, H. Hänninen, Acta Materialia, 56 (2008) 5492-5499.
[97] G. Mogylnyy, I. Glavatskyy, N. Glavatska, O. Söderberg, Y. Ge, V.K. Lindroos, Scripta Materialia, 48 (2003) 1427-1432.
[98] M. Han, J.C. Bennett, M.A. Gharghouri, J. Chen, C.V. Hyatt, Acta Materialia, 55 (2007) 1731-1740.
[99] M. Han, F.F. Kong, Journal of Alloys and Compounds, 458 (2008) 218-222.
[100] M. Nishida, T. Hara, M. Matsuda, S. Ii, Materials Science and Engineering: A, 481-482 (2008) 18-27.
[101] D.Y. Cong, Y.D. Zhang, Y.D. Wang, C. Esling, X. Zhao, L. Zuo, Journal of Applied Crystallography, 39 (2006) 723-727.
[102] D.Y. Cong, Y.D. Zhang, Y.D. Wang, M. Humbert, X. Zhao, T. Watanabe, L. Zuo, C. Esling, Acta Materialia, 55 (2007) 4731-4740.
[103] N. Scheerbaum, O. Heczko, J. Liu, D. Hinz, L. Schultz, O. Gutfleisch, New Journal of Physics, 10 (2008) 073002.
[104] N. Scheerbaum, Y.W. Lai, T. Leisegang, M. Thomas, J. Liu, K. Khlopkov, J. McCord, S. Fähler, R. Träger, D.C. Meyer, L. Schultz, O. Gutfleisch, Acta Materialia, 58 (2010) 4629-4638.
[105] R. Chulist, W. Skrotzki, C.G. Oertel, A. Böhm, T. Lippmann, E. Rybacki, Scripta Materialia, 62 (2010) 650-653.
[106] R. Chulist, W. Skrotzki, C.G. Oertel, A. Böhm, M. Pötschke, Scripta Materialia, 63 (2010) 548-551.

[107] M. Pötschke, S. Weiss, U. Gaitzsch, D. Cong, C. Hürrich, S. Roth, L. Schultz, Scripta Materialia, 63 (2010) 383-386.
[108] M. Humbert, F. Wagner, H. Moustahfid, C. Esling, Journal of Applied Crystallography, 28 (1995) 571-576.
[109] W. Kraus, G. Nolze, Journal of Applied Crystallography, 29 (1996) 301-303.
[110] H.J. Bunge, C. Esling, J. Muller, Journal of Applied Crystallography, 13 (1980) 544-554.
[111] C. Jiang, Y. Muhammad, L. Deng, W. Wu, H. Xu, Acta Materialia, 52 (2004) 2779-2785.
[112] B.A. Bilby, A.G. Crocker, Proceedings of the Royal Society of London Series A-Mathematical and Physical Sciences, 288 (1965) 240-&.
[113] Y.D. Zhang, C. Esling, X. Zhao, L. Zuo, Journal of Applied Crystallography, 40 (2007) 436-440.
[114] D.Y. Cong, Y.D. Wang, P. Zetterstrom, R.L. Peng, R. Delaplane, X. Zhao, L. Zuo, Materials Science and Technology, 21 (2005) 1412-1416.
[115] V.A. Chernenko, E. Cesari, J. Pons, C. Segui, Journal of Materials Research, 15 (2000) 1496-1504.
[116] A.N. Vasil'ev, A.D. Bozhko, V.V. Khovailo, I.E. Dikshtein, V.G. Shavrov, V.D. Buchelnikov, M. Matsumoto, S. Suzuki, T. Takagi, J. Tani, Physical Review B, 59 (1999) 1113.
[117] H. Kato, Scripta Materialia, 38 (1998) 1125-1130.
[118] K. Otsuka, K. Shimizu, Transactions of the Japan Institute of Metals, 15 (1974) 103-108.
[119] T.A. Schroeder, C.M. Wayman, Acta Metallurgica, 25 (1977) 1375-1381, 1383-1391.
[120] K. Bhattacharya, Acta Metallurgica et Materialia, 39 (1991) 2431-2444.
[121] X. Balandraud, G. Zanzotto, Journal of the Mechanics and Physics of Solids, 55 (2007) 194-224.
[122] S. Miyazaki, K. Otsuka, C.M. Wayman, Acta Metallurgica, 37 (1989) 1873-1884.
[123] Y. Deng, G.S. Ansell, Journal of Materials Science, 26 (1991) 5254-5260.
[124] K. Adachi, J. Perkins, C.M. Wayman, Acta Metallurgica, 34 (1986) 2471-2485.
[125] Y. Sutou, Y. Imano, N. Koeda, T. Omori, R. Kainuma, K. Ishida, K. Oikawa, Applied Physics Letters, 85 (2004) 4358-4360.
[126] M. Ahart, M. Somayazulu, R.E. Cohen, P. Ganesh, P. Dera, H.-k. Mao, R.J. Hemley, Y. Ren, P. Liermann, Z. Wu, Nature, 451 (2008) 545-548.
[127] T. Krenke, M. Acet, E.F. Wassermann, X. Moya, L. Manosa, A. Planes, Physical Review B, 72 (2005).
[128] T. Krenke, M. Acet, E.F. Wassermann, X. Moya, L. Manosa, A. Planes, Physical Review B, 73 (2006).
[129] K. Oikawa, L. Wulff, T. Iijima, F. Gejima, T. Ohmori, A. Fujita, K. Fukamichi, R. Kainuma, K. Ishida, Appl. Phys. Lett., 79 (2001) 3290-3292.
[130] A.G. Khachaturyan, S.M. Shapiro, S. Semenovskaya, Physical Review B, 43 (1991) 10832.
[131] Y.M. Jin, Y.U. Wang, A.G. Khachaturyan, J.F. Li, D. Viehland, Physical Review Letters, 91 (2003) 197601.

Publication list

1. **Z. B. Li**, Y. D. Zhang, C. Esling, X. Zhao, L. Zuo, "EBSD-based crystallographic study on a Ni-Mn-Ga alloy with incommensurate 7M structure", **Materials Science Forum**, 702-703 (2012) 530-535.

2. **Z. B. Li**, Y. D. Zhang, C. Esling, H. Yang, J. J. Wang, C. S. He, X. Zhao, L. Zuo, "Application of EBSD to the crystallographic investigation on Ni-Mn-Ga alloys", **Materials Science Forum**, 706-709 (2012) 1879-1884

3. Y. D. Zhang, **Z. B. Li**, C. Esling, X. Zhao, L. Zuo,"Calculation methods to determine crystallographic elements based on electron diffraction orientation measurements by SEM/EBSD or TEM", **Materials Science Forum**, 706-709 (2012) 2674-2679

4. **Z. B. Li**, Y. D. Zhang, C. Esling, X. Zhao, L. Zuo, "Determination of the orientation relationship between austenite and 5M modulated martensite in Ni-Mn-Ga alloys", **J. Appl. Cryst.** (2011). 44, 1222-1226

5. **Z. B. Li**, Y.D. Zhang, C. Esling, X. Zhao, L. Zuo,"Determination of the orientation relationship between austenite and incommensurate 7M modulated martensite in Ni-Mn-Ga alloys", **Acta Mater**. 59 (2011) 2762-2772.

6. **Z. B. Li**, Y.D. Zhang, C. Esling, X. Zhao, L. Zuo, "Twin relationships of 5M modulated martensite in Ni-Mn-Ga alloy", **Acta Mater.** 59 (2011) 3390-3397.

7. **Z. B. Li**, Y.D. Zhang, C. Esling, X. Zhao, Y.D. Wang, L. Zuo. "New approach into twin interfaces of modulated martensite", **J. Appl. Cryst.**, 43(2010), 617-622.

8. **Z. B. Li**, J.J. Wang, Y.D. Zhang, K.Z. He, X. Zhao, L. Zuo, G. Hofer, C. Esling, "Texturation of Ni-Co-Mn-In ribbons by melt spinning", **Adv. Eng. Mater.**, 10(2010), 1024-1028.

9. Y.D. Zhang, **Z. B. Li**, C. Esling, J. Muller, X. Zhao, L. Zuo, "A general method to determine twinning elements", **J. Appl. Cryst.**, 43(2010), 1426-1430.

Résumé Etendu

Les alliages à mémoire de forme ferromagnétiques sont de nouveaux matériaux pour actionneurs et capteurs, car ils peuvent combiner de grandes déformations avec une réponse dynamique rapide lors d'un événement d'actionnement par un champ magnétique extérieur. Cette fonctionnalité ne pourrait pas être obtenue avec d'autres matériaux à mémoire de forme comme les céramiques piézo-électriques, les matériaux magnétostrictifs et les alliages à mémoire de forme classiques. Parmi les alliages ferromagnétiques à mémoire de forme, les matériaux les plus représentatifs sont les alliages de Ni-Mn-Ga avec les structures de martensite modulées qui présentent un excellent effet magnétique à mémoire de forme (par exemple, des déformations entièrement réversibles jusqu'à 10% dans des monocristaux) [1, 2]. Leurs énormes déformations en sortie résultent de la réorientation des variantes martensitiques par le mouvement des joints de variantes induits par un champ magnétique externe.

Il apparaît que les relations d'orientation entre les variantes martensitiques, les caractéristiques des plans cristallographiques entre les variantes et le nombre de variantes sont les facteurs déterminants qui affectent la réorientation des variantes, et donc les performances de mémoire de forme magnétique. Pourtant, l'exploration de ces questions clés a été plutôt limitée et empirique, en raison d'un manque d'analyse complète et correcte de la superstructure de la martensite modulée. Avec les progrès récents faits par diffraction de poudre [3, 4], les structures de martensite modulées en 5M et en 7M dans les alliages Ni-Mn-Ga ont été entièrement résolues. Ceci établit les fondements pour une caractérisation plus avancée de ces matériaux. À cet égard, nous avons fait les premiers efforts en examinant de façon approfondie les microstructures et les orientations cristallographiques des variantes martensitiques, les relations d'orientation (OR) entre les variantes de martensite et les relations d'orientation dans la transformation. Ces résultats offrent une base solide pour des études futures vers la

conception et le contrôle des structures modulées.

L'alliage polycristallin Ni-Mn-Ga de composition nominale $Ni_{50}Mn_{28}Ga_{22}$ (5M), $Ni_{50}Mn_{30}Ga_{20}$ (7M), $Ni_{54}Mn_{24}Ga_{22}$ (NM) et $Ni_{53}Mn_{22}Ga_{22}$ (austénite plus martensite) a été préparé et examiné par rayons X et en MEB-EBSD.

1. Caractérisation cristallographique de la martensite 5M

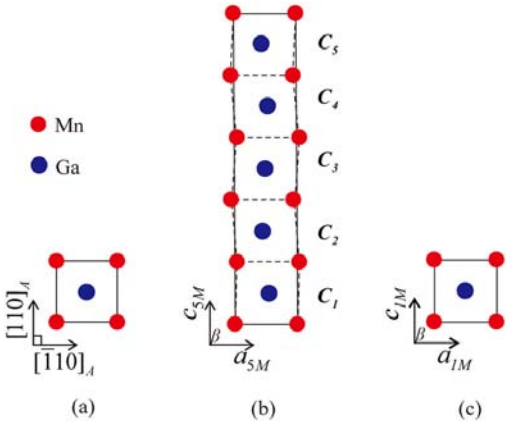

Fig.1 Représentations schématiques de (a) de la cellule élémentaire de l'austénite cubique, (b) de la supercellule monoclinique de la martensite modulée 5M constituée de cinq sous-cellules (décrites par les traits pointillés), et (c) de la cellule réduite unitaire moyenne (en ignorant les modulations du réseau).

L' alliage polycristallin $Ni_{50}Mn_{28}Ga_{22}$ (at.%) hors-stoechiométrique riche en Mn avec une martensite modulée (5M) à la température ambiante a été préparé par fusion sous arc. Les mesures DSC montrent que la transformation de l'austénite en martensite a débuté à 43,8 °C (Ms) et fini à 30,0 °C (Mf) lors du refroidissement. La transformation inverse a commencé à 41,1 °C (As) et fini à 51,3 °C (A_f) lors du chauffage. Les figures 1a et b illustrent la correspondance des mailles entre l'austénite et la martensite 5M. L'austénite à haute température possède une structure de Heusler L_{21} cubique ($Fm\bar{3}m$, N° 225) avec le paramètre de maille a_A= = 5.84Å [5, 6]. La martensite 5M a une superstructure monoclinique (P2 / m, N° 10) [3], composée de cinq sous-mailles consécutives le long de l'axe c (notées C1, C2 ... ... C5 dans la Fig. 1b). Les axes cristallographiques monocliniques de la martensite 5M s'alignent le long de $[\bar{1}10]_A$ (axe *a*), $[001]_A$ (axe *b*) et $[110]_A$ (axe *c*), des directions de l'austénite cubique. Selon la mesure de diffraction aux rayons X, les paramètres de maille de la

martensite 5M ont été établis à a_{5M} = 4.226Å, b_{5M} = 5.581Å, C_{5M} = 21.052Å et β =90,3°. Si nous ignorons la modulation des atomes, la supercellule pourrait être encore réduite en une seule sous-cellule (1M martensite) avec des constantes de réseau $a_{1M} = a_{5M}$ = 4,226 Å, $b_{1M} = b_{5M}$ = 5,581 Å, $c_{1M} = c_{5M} / 5$ = 4,2104 Å, et β = 90.3 °, comme illustré dans la figure 1c. Ci-après, l'austénite, la martensite 1M et la martensite 5M sont désignées par les indices "A", "1M" et "5M", respectivement.

La figure 2a montre une image typique des électrons rétrodiffusés (*BSE backscattered electrons*), de l'alliage polycristallin $Ni_{50}Mn_{28}Ga_{22}$ prise à la température ambiante. La martensite est composée de larges plaques distribuées alternativement avec plusieurs micromètres de largeur. Les observations complémentaires à grossissement supérieur montrent que les grandes plaques sont composées de fines lamelles de l'épaisseur de l'ordre du nanomètre. En appliquant les informations de superstructure de la martensite 5M à l'indexation des clichés de Kikuchi, la carte d'orientation des lamelles fines dans les plaques larges a été reconstruite comme indiqué dans la figure 2b, où les lamelles individuelles fines ont été colorées en fonction de leurs orientations. Notamment, quatre types de variantes d'orientation ont été identifiés et désignés comme A, B, C et D. Cependant, seulement deux variantes peuvent être identifiés en cas d'utilisation de la structure tétragonale non modulée simplifiée à l'indexation des clichés de Kikuchi.

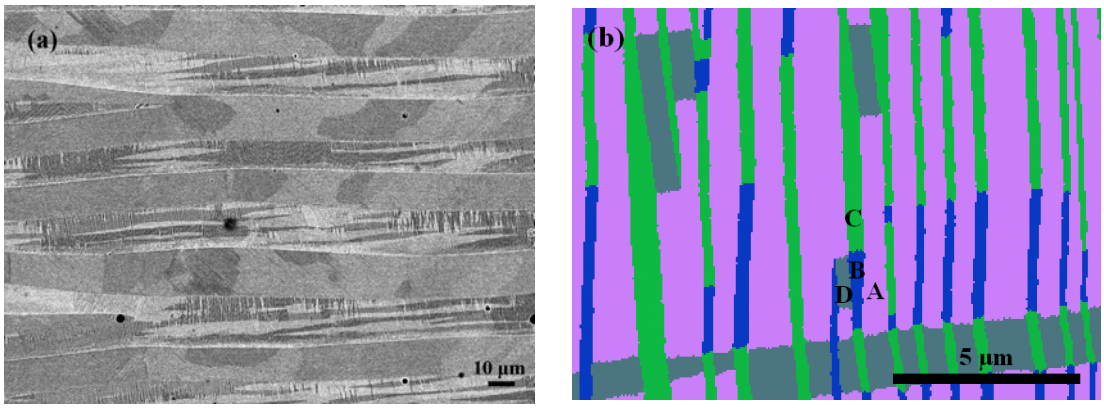

Fig.2 (a) L'image ESB des plaques de martensite larges dans un grain initial d'austénite; (b) micrographie d'orientation des fines lamelles.

Avec les données correctes d'orientation des variantes de martensite individuelle acquis par EBSD, les relations d'orientation entre les variantes ont été déterminées

selon le calcul de désorientation (comme indiqué dans le tableau 1). Les résultats ont démontré que les variantes adjacentes sont en relation de maclage. Les variantes A et C (ou B et D) sont en relation de macles de type I, A et B (ou C et D) de type II, et A et D (ou B et C) en relation de macles composées. Les éléments complets de maclage des trois types de macles ont été déterminés de façon univoque comme indiqué dans le tableau 2. Par ailleurs, les interfaces entre les macles sont également entièrement déterminées à l'aide de la méthode de la double trace indirecte [7]. Les interfaces se trouvent en coïncidence avec leurs plans respectifs de maclage (plan K1).

Tableau 1 Angles de désorientation (ω) et les axes de rotation (**d**) entre les variantes A, B, C et D dans la figure 3(a). Les axes de rotation sont répérés au repère orthonormé de cristal placé sur le réseau monoclinique de la martensite.

Variant pair	Misorientation angle ω [°]	Rotation axis, **d**		
		d_1	d_2	d_3
A:C	86.80	-0.70846	0.00241	-0.70575
	179.81	0.48490	-0.72659	-0.48676
B:D	86.79	-0.71242	-0.00221	-0.70175
	179.83	-0.48214	0.72661	0.48947
A:B	93.32	0.70870	0.00098	0.70551
	179.92	-0.51312	-0.68633	0.51543
C:D	93.09	0.70882	0.00435	0.70538
	179.64	-0.51205	-0.68778	0.51455
A:D	179.64	0.70487	-0.00098	-0.70933
	179.89	-0.70933	0.00317	-0.70487
B:C	179.88	0.70978	0.00079	0.70443
	179.91	-0.70443	-0.00102	0.70978

Tableau 2 Eléments de maclage de la martensite modulée 5M dans $Ni_{50}Mn_{28}Ga_{22}$.

	Type I (A:C and B:D)	Type II (A:B and C:D)	Compound (A:D and B:C)
K_1	$(1\ \bar{2}\ \bar{5})$	$(1.0569\ \bar{2}\ \overline{4.7155})$	(1 0 5)
K_2	$(\overline{1.0569}\ \bar{2}\ 4.7155)$	$(\bar{1}\ \bar{2}\ 5)$	$(\bar{1}\ 0\ 5)$
η_1	$[\overline{5.2504}\ \bar{5}\ 0.9499]$	$[\bar{5}\ \bar{5}\ 1]$	$[\bar{5}\ 0\ 1]$
η_2	$[5\ \bar{5}\ \bar{1}]$	$[5.2504\ \bar{5}\ \overline{0.9499}]$	[5 0 1]
P	$(1\ \overline{0.0514}\ 5.2568)$	(1 0.0514 5.2568)	(0 1 0)
s	0.1387	0.1387	0.0074

Comme la transformation martensitique est réalisée par le déplacement coordonné d'atomes, certaines relations d'orientation (ORs) spécifiques entre la phase parent et la

phase produit sont nécessaires pour éliminer la discontinuité de réseau. Ces ORs ont été généralement déterminées en tirant parti de la coexistence de l'austénite résiduelle et la martensite produite. Pourtant, pour le présent alliage étudié, comme la transformation martensitique est complète à la température ambiante, il n'est pas possible de faire une détermination directe. Donc la vérification des orientations de l'austénite qui sont calculées à partir des orientations des variantes de martensite produites à partir de la même austénite initiale en vertu d'une OR assumée pourrait être une solution alternative pour déduire la OR [5]. Si les orientations de l'austénite calculées à partir des variantes de martensite partagent une orientation d'austénite parente commune, la relation d'orientation assumée pourrait être celle qui gouverne la transformation martensitique, et l'orientation commune de l'austénite est celle du grain d'austénite initiale.

L'orientation G_A^l d'un grain d'austénite par rapport au repère orthonormé de l'échantillon peut être exprimée par la relation suivante en matrices:

$$G_A^l = G_M^k \cdot S_M^i \cdot T \cdot (S_A^j)^{-1}$$

où G_M^k représente l'orientation mesurée du $k^{ème}$ variant de la martensite par rapport au repère orthonormé de l'échantillon ; T est la matrice de rotation qui transforme le repère orthonormé lié à la base du réseau monoclinique de la martensite à celui cubique de l'austénite en respectant la OR donnée ; S_A^j (j = 1, 2, ..., 24) et S_{7M}^i (i = 1, 2) sont les éléments de symétrie de rotation du système cristallin cubique et du système cristallin monoclinique, respectivement. En se basant sur une étude bibliographique, les ORs de Bain, de KS, de NW et de Pitsch sont présumées comme les ORs possibles de la transformation dans le présent travail. Pour des raisons de simplicité, les ORs exprimées en parallélisme des plans et des directions dans les plans sont d'abord vérifiées entre l'austénite et la martensite 1M moyenne (Fig.1c).

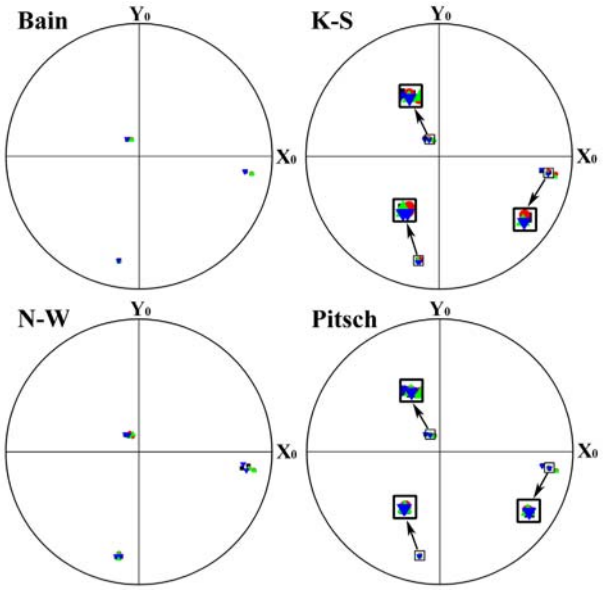

Fig.3 {001} Projections stéréographiques standard des orientations de l'austénite calculées à partir des variantes de martensite A (■), B (●), C (▲) et D (▼) dans la variante du groupe g1 sous les hypothèses d'OR de Bain, KS, N-W et Pitsch, respectivement. Les orientations communes de l'austénite sont encadrées.

En se basant sur les considérations qui précèdent, nous avons calculé les orientations de l'austénite parente à partir des orientations mesurées des quatre variantes de martensite qui sont localement liées en relation de macle. Ici, un ensemble de quatre variantes en relation de macle dans un platelet large est traité comme un groupe de variantes. Les orientations calculées de l'austénite sous une OR donnée ont été tracées dans la projection stéréographique standard {001} de l'austénite dans le repère macroscopique de l'échantillon. A titre d'exemple, la figure 3 affiche les résultats du calcul d'un groupe de variantes, où une orientation de l'austénite est représentée par trois pôles {001}. On voit qu'il y a une orientation distincte calculée pour l'austénite à partir de la martensite sous l'hypothèse de la relation de Bain, et deux sous KS, NW et Pitsch, respectivement. Si la OR présumée est vraie pour la transformation, tous les trois pôles {001} austénite d'une variante de martensite devraient correspondre à celles des trois autres variantes dans le même groupe de variantes. Il apparaît que les relations de KS et Pitsch donnent le moins de dispersion parmi les pôles {001} respectifs pour une orientation commune de l'austénite. Afin de quantifier les écarts pour une OR présumée, les angles

désorientation minimum entre deux orientations calculées de l'austénite ont été estimés. En effet, parmi tous les groupes de variantes choisies, Pitsch présente le plus petit angle de déviation. Par conséquent, la OR de Pitsch, c'est à dire $(101)_A//(1\bar{2}\bar{1})_{1M}$ et $[10\bar{1}]_A//[\bar{1}\bar{1}1]_{1M}$ entre l'austénite et la martensite 1M, ou $(101)_A//(1\bar{2}\bar{5})_{5M}$ et $[10\bar{1}]_A//[\bar{5}\bar{5}1]_{5M}$ si raaportée à la martensite 5M, devrait être considérée comme la OR la plus favorable pour la transformation.

2. Caractérisation cristallographique de la martensite 7M

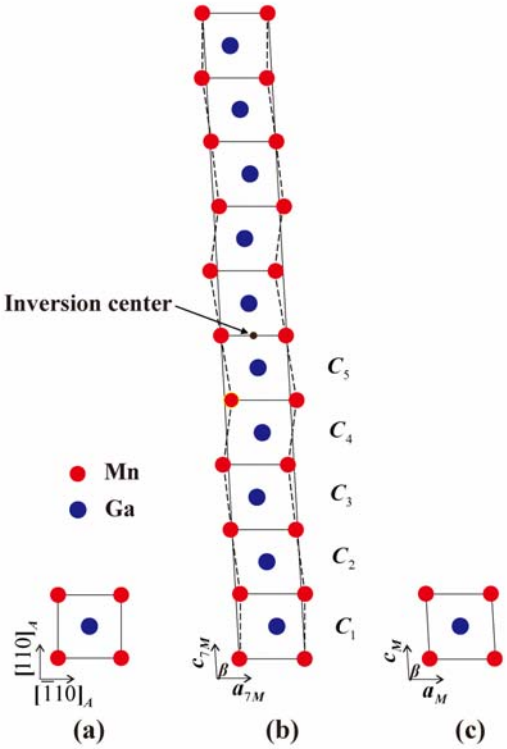

Fig.4 Représentation schématique de (a) maille de l'austénite; (b) supercellule de martensite 7M, où chaque cellule élémentaire (martensite 1M) est indiquée en pointillés et les cinq cellules élémentaires avec des constantes distinctes sont désignées comme C_1, C_2 ... C_5 ; (c) cellule moyenne de la martensite modulée.

Pour l'alliage étudié ($Ni_{50}Mn_{30}Ga_{20}$), la transformation martensitique de l'austénite en martensite commence à 361.7K et se termine à 351.3K, la transformation inverse commence à 360.7K et se termine à 370.2K, respectivement. L'austénite possède une structure cristalline cubique $L2_1$ (Fm3m, No. 225) avec le paramètre de maille a_A = 5,84 Å [6]. La martensite 7M a une structure cristalline monoclinique avec une modulation incommensurable composée de 10 sous-cellules le long de l'axe c (P2/m,

No. 10) [4]. Les paramètres de maille ont été déterminés à partir des mesures XRD comme étant a_{7M} = 4.2651Å, b_{7M} = 5.5114Å, c_{7M} = 42.365Å, et β = 93,27°. La cellule primitive de l'austénite cubique et celle de la martensite modulée sont illustrées dans la figure 4. Les vecteurs de base de réseau de la superstructure 7M modulée s'alignent le long de [$\bar{1}$ 10], [001] et [110] du réseau austénitique cubique. Comme le superréseau de 7M est centrosymétrique (la figure 4(b)) [4], seules cinq sous-cellules constituent la cellule primitive (notées C_1, C_2, C_3, C_4 et C_5) avec des constantes de cellules distinctes et les autres sous-cellules pourraient être générés par l'opération d'inversion. Si nous ignorons la modulation du réseau, la supercellule de dix éléments peut être réduit en une seul sous-cellule monoclinique avec les constantes de réseau moyennes $a_{1M} = a_{7M}$ = 4.2651 Å, $b_{1M} = b_{7M}$ = 5.5114 Å, $c_{1M} = c_{7M}/10$ = 4.2365 Å, et β = 93.27°, comme schématisé dans la figure 4(c). Ci-après, nous ferons référence à cette sous-cellule moyenne appelée "1M martensite" pour représenter la martensite 7M incommensurable modulée, et noterons l'austénite, la martensite 1M et la martensite 7M en précisant le symbole "A ", "1M" et "7M" dans l'indice, respectivement.

En utilisant le modèle de superstructure modulée de la martensite, nous avons réussi à faire des mesures en EBSD (MEB) qui n'avaient jamais été rapportées ailleurs. La Fig.5a montre l'image typique en contraste d'électron rétrodiffusé (ESB) de l'alliage polycristallin $Ni_{50}Mn_{30}Ga_{20}$ et la Fig.5b la cartographie d'orientation cristallographique déterminée localement sur une colonie. L'orientation de chaque pixel de l'image est déterminée avec le modèle de structure illustré dans la Fig.5b. On voit dans la Fig.5a que la martensite est en forme de plaques et que les plaques sont regroupées en colonies. Une colonie ou plusieurs colonies sont situées au sein d'un grain d'austénite initiale. Dans la Fig.5b les plaques de martensite sont colorées en fonction de leur orientation. Localement, il y a quatre variantes réparties alternativement, désignées comme variante A, B, C et D.

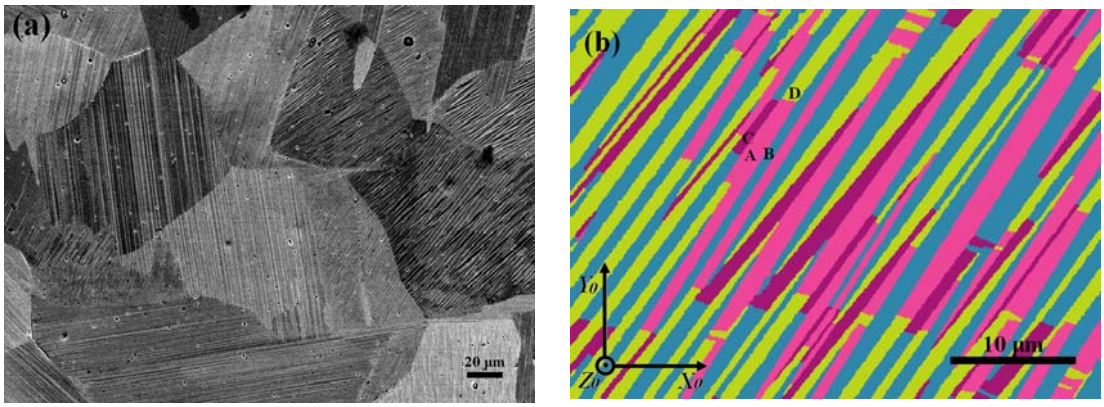

Fig.5 (a) Une image typique en contraste d'ESB de l'alliage polycristallin $Ni_{50}Mn_{30}Ga_{20}$. (b) Cartographie d'orientation EBSD déterminée localement sur une colonie. Le système de coordonnées (X_0-Y_0-Z_0) se réfère au système de coordonnées macroscopiques de l'échantillon.

En se basant sur les données d'orientation acquises par EBSD, les relations d'orientation entre les variantes martensitiques adjacentes ont été déterminées avec les techniques de calcul de désorientation. Les résultats ont montré que les variantes adjacentes sont en relation de maclage. Les variantes A: C (ou B: D) sont en relation de macle de type I, A: B (ou C: D) de macle de type II, et A: D (ou B: C) de macle composée. Les éléments complets des trois types de macle ont été déterminés avec précision en utilisant une méthode développée par notre groupe de recherche [7] et présentés dans le tableau 3. De plus, les interfaces entre les macles sont également entièrement déterminées, en utilisant une autre méthode développée par notre groupe de recherche [8]. Les interfaces entre les macles se trouvent en coïncidence avec leurs plans respectifs de maclage (plan K_1). Ces résultats essentiels offrent un nouveau regard sur la nature cristallographique des interfaces de macles doubles avec des informations microstructurales fondamentales nécessaires pour la modification de microstructure et le contrôle des performances fonctionnelles des alliages à mémoire de forme ferromagnétiques.

Tableau 3 Éléments de maclage de la martensite 7M modulée de l'alliage $Ni_{50}Mn_{30}Ga_{20}$. Tous les indices sont exprimés en utilisant le modèle de supermaille composée de 10 sous cellules.

Elements	Type-I (A:C or B:D)	Type-II (A:B or C:D)	Compound (A:D or B:C)
K_1	$(1\ \bar{2}\ \overline{10})$	$(1.0621\ \bar{2}\ \overline{9.3785})$	(1 0 10)
K_2	$(\overline{1.0621}\ \bar{2}\ 9.3785)$	$(\bar{1}\ \bar{2}\ 10)$	$(\bar{1}\ 0\ 10)$
η_1	$[\overline{10.5541}\ \overline{10}\ 0.9446]$	$[\overline{10}\ \overline{10}\ 1]$	$[\overline{10}\ 0\ 1]$
η_2	$[10\ \overline{10}\ \bar{1}]$	$[10.5541\ \overline{10}\ \overline{0.9446}]$	[10 0 1]
P	$(1\ \overline{0.057}\ 10.5699)$	(1 0.057 10.5699)	(0 1 0)

s	0.2299	0.2299	0.0135

La relation d'orientation (OR) entre l'austénite et la martensite 7M a en outre été prédite sur la base de mesures expérimentales et de calculs cristallographiques. La OR de Bain classique, celles de KS, de NW et de Pitsch sont présumés comme OR possibles entre l'austénite parent et la martensite 7M. Les parallélismes des plan présumés et de directions dans le plan sont d'abord utilisés pour spécifier les ORs entre l'austénite et la martensite 1M (Fig. 4c).

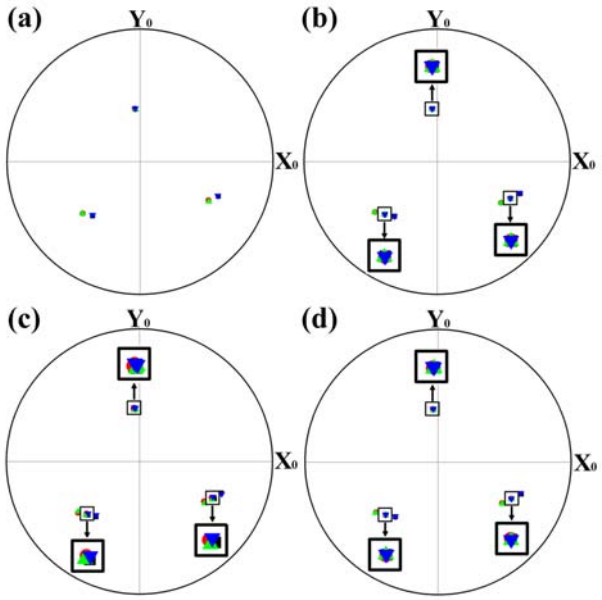

Fig. 6 Figures de pôles {0 0 1} de l'austénite calculées pour les variantes A (■), B (●), C (▲) and D (▼) de la martensite sous l'hypothèse des ORs de (a) Bain, (b) K-S, (c) N-W et (d) Pitsch, respectivement. Les pôles correspondant à l'orientation commune de l'austénite sont encadrées.

Avec la méthode ci-dessus, nous avons calculé les orientations de l'austénite à partir des orientations mesurées de variantes martensitiques, en utilisant les quatre ORs classiques. Pour faciliter la visualisation, les orientations calculées de l'austénite sont montrées dans la figures de pôles {001} dans le repère macroscopique de l'échantillon (figure 6). Si la OR assumée est effectivement celle de la transformation, les pôles {001} de l'austénite calculés à partir de différentes variantes martensitiques devraient tomber en coïncidence dans la figure de pôle. Apparemment, la relation d'orientation de KS et celle de Pitsch peuvent donner lieu au meilleur accord parmi les figures de pôles {001} correspondantes pour une orientation d'austénite commune,

comme cela apparaît dans les agrandissements des carrés sur les figures 6 (b) et (d). Pour quantifier la qualité de l'accord des relations d'orientation, les angles de désorientation minimum entre les orientations des diverses solutions calculées pour l'austénite ont été estimés. Les résultats ont montré que l'OR de KS et celle de Pitsch donnent le plus petit angle de déviation et qu'il n'y a presque pas de différence entre les deux ORs, ce qui suggère que ces deux ORs pourraient être considérées comme possibles pour la transformation.

Pour continuer à discriminer les deux relations et déterminer celle qui serait la plus favorable pour la transformation, les déformations de réseau pendant la transformation sous l'hypothèse des deux relations (cf. figure 7) ont été examinées. La déformation du réseau est décomposée en dilatation ou contraction et en cisaillement, comme indiqué dans la figure 7. Les quantités de déformation sous l'hypothèse des deux relations ont été calculées et reportées dans le tableau 4. Dans le cas de KS, l'allongement ou la contraction est assigné dans $[111]_A$, $[1\,\bar{2}\,1]_A$ et $[10\,\bar{1}\,]_A$. Le cisaillement simple dans $(111)_A$ le long de $[\,\bar{1}\,01]_A$, dans $(1\,\bar{2}\,1)_A$ le long de $[10\,\bar{1}\,]_A$ et dans $(10\,\bar{1}\,)_A$ le long de $[1\,\bar{2}\,1]_A$. Pour celle de Pitsch, l'allongement ou la contraction est assigné dans $[101]_A$, $[0\,\bar{1}\,0]_A$ and $[10\,\bar{1}\,]_A$ et le cisaillement simple dans $(101)_A$ le long de $[\,\bar{1}\,01]_A$, dans $(0\,\bar{1}\,0)_A$ le long de $[10\,\bar{1}\,]_A$ et dans $(10\,\bar{1}\,)_A$ le long de $[0\,\bar{1}\,0]_A$, respectivement. Par rapport à la relation de KS, celle de Pitsch implique une distorsion de réseau relativement petite (seulement les 2 derniers éléments de cisaillement sont légèrement élevés) pour la transformation de l'austénite à la martensite 1M moyenne. Considérant que l'allongement ou la contraction exige un changement de volume, et que le cisaillement simple n'exige pas, la déformation par un cisaillement simple peut se produire plus facilement. De ce point de vue, la relation de Pistch est énergiquement avantageuse par rapport à celle de KS pour la transformation de l'austénite en martensite 1M. Afin de mieux distinguer les quantités de déformation sous l'hypothèses des deux relations, les écarts entre les plans $(1\,\bar{2}\,\bar{1}\,)$ (Pitch)/(011) (KS) et les directions $[\,\bar{1}\,\bar{1}\,1]$ (Pitch et KS) de chaque souscellule 7M de la supermaille par rapport au ceux de la cellule moyenne 1M sont évalués. Comme montré dans la figure 8, la relation de KS et celle de Pitsch diffèrent l'une de l'autre

seulement par l'écart de plan, dans la mesure où les deux relations d'orientation possèdent le même parallélisme entre les directions. La OR de KS provoque un écart plus grand que celle de Pitsch, ce qui signifie que la OR de KS exige un plus grand réarrangement atomique pour réaliser la modulation de la structure. Ce résultat confirme également que la relation d'orientation de Pitsch, c'est à dire $(101)_A//(1\,\bar{2}\,\overline{10})_{7M}$ et $[10\,\bar{1}]_A//[\overline{10}\;\overline{10}\;1]_{7M}$ entre l'austénite et la martensite, est plus favorable que celle de KS pour la transformation martensitique.

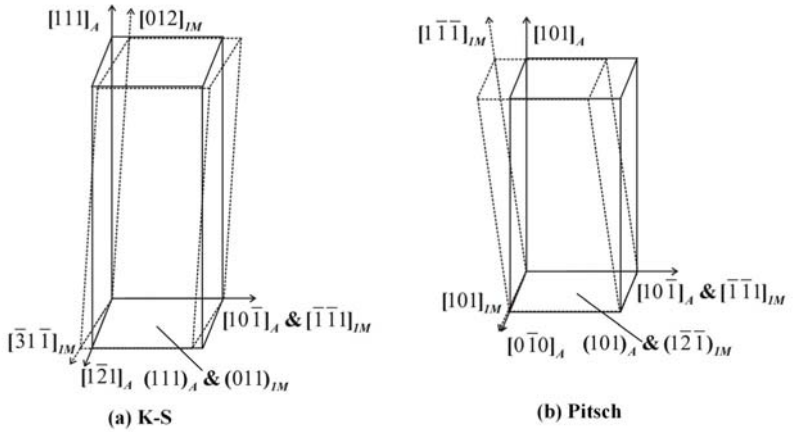

Fig.7 Correspondances atomiques des plans respectifs dans l'austénite et la martensite 1M sous l'hypothèse (a) relation de K-S avec $(111)_A//(011)_{1M}$ et $[10\,\bar{1}]_A//[\bar{1}\;\bar{1}\;1]_{1M}$; (b) relation de Pitsch avec $(101)_A//(1\,\bar{2}\;\bar{1})_{1M}$ et $[10\,\bar{1}]_A//[\bar{1}\;\bar{1}\;1]_{1M}$.

Tableau 4. Quantité de déformation des réseaux lors de la transformation de l'austénite en martensite sous l'hypothèse de la relation de K-S avec $(111)_A//(011)_{1M}$ et $[10\,\bar{1}]_A//[\bar{1}\;\bar{1}\;1]_{1M}$ et celle de Pitsch avec $(101)_A//[1\,\bar{2}\;\bar{1}]_{1M}$ et $[10\,\bar{1}]_A//[\bar{1}\;\bar{1}\;1]_{1M}$.

K-S		Pitsch	
Dilatation dans $[111]_A$	-0.4834%	Dilatation dans $[101]_A$	-0.3923%
Dilatation dans $[1\,\bar{2}\,1]_A$	0.0531%	Dilatation dans $[0\,\bar{1}\,0]_A$	-0.0428%
Dilatation dans $[10\,\bar{1}]A$	0.2664%	Dilatation dans $[10\,\bar{1}]A$	0.2664%
Cisaillement $(111)_A\,[\bar{1}01]_A$	0.0701	Cisaillement$(101)_A\,[\bar{1}01]_A$	0.0051
Cisaillement$(1\,\bar{2}\,1)_A\,[10\,\bar{1}]_A$	0.0910	Cisaillement$(0\,\bar{1}\,0)_A[10\,\bar{1}]_A$	0.1149
Cisaillement$(10\,\bar{1})_A\,[1\,\bar{2}\,1]_A$	0.0018	Cisaillement$(10\,\bar{1})_A\,[0\,\bar{1}\,0]_A$	0.0045

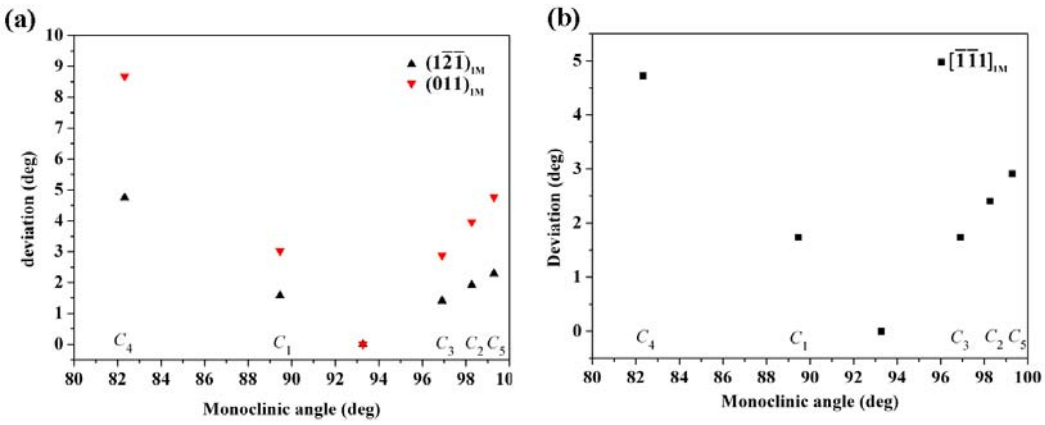

Fig. 8 Écarts angulaires de (a) plans $(1\,\bar{2}\,\bar{1})_{1M}$ (relation de Pitsch) et $(011)_{1M}$ (relation de K-S) et (b) direction $[\,\bar{1}\,\bar{1}\,1]_{1M}$ dans les 5 sous cellules (C1, C2, …, C5) par rapport à ceux de la cellule moyenne 1M.

3. Caractéristiques cristallographiques de la martensite NM.

L'alliage $Ni_{54}Mn_{24}Ga_{22}$ avec la martensite non-modulée à la température ambiante a été préparé. Les diagrammes de diffraction de rayons X de poudre mesurés à la température ambiante démontrent que l'alliages possède seulement la martensite non-modulée avec une structure cristalline tétragonale. Les spectres peuvent être indexés par le groupe d'espace I4/mmm (n ° 139) [10]. Les constantes de maille de l'alliages ont été déterminés comme a_T=b_T= 3.853 Å et c_T=6.625 Å, respectivement.

Des mesures EBSD ont révélé que les plaques de martensite adjacentes ont la relation d'orientation de 80° ~ 85° de rotation autour d'axes <110> $_T$. Des observations additionnelles en MEB à fort grossissement ont montré que les plaques NM sont composées de lamelles mince et il y a quatre types de plaques de martensite (notées P1, P2, P3 et P4) dans une colonie de martensite selon l'orientation des minces interfaces lamellaires, comme représenté sur la fig. 9. Les lamelles fine apparaissent en paires, dans lesquelles l'une est plus épaisse que l'autre. Ainsi, dans une colonie de martensite, on peut toujours trouver huit variantes d'orientation. Les variantes fines appariées dans chaque plaque ont été trouvées en relation de macle avec le plan $\{112\}_T$ comme plan de macle et $<11\,\bar{1}>_T$ comme direction de maclage. Les interfaces inter-plaques sont proches du plan $\{1\,\bar{1}\,2\}_T$, mais avec un écart de ~ 3 °, tandis que les interfaces de deux paires de variantes fines appariées sont en bon accord avec le

plan de macle {112}.

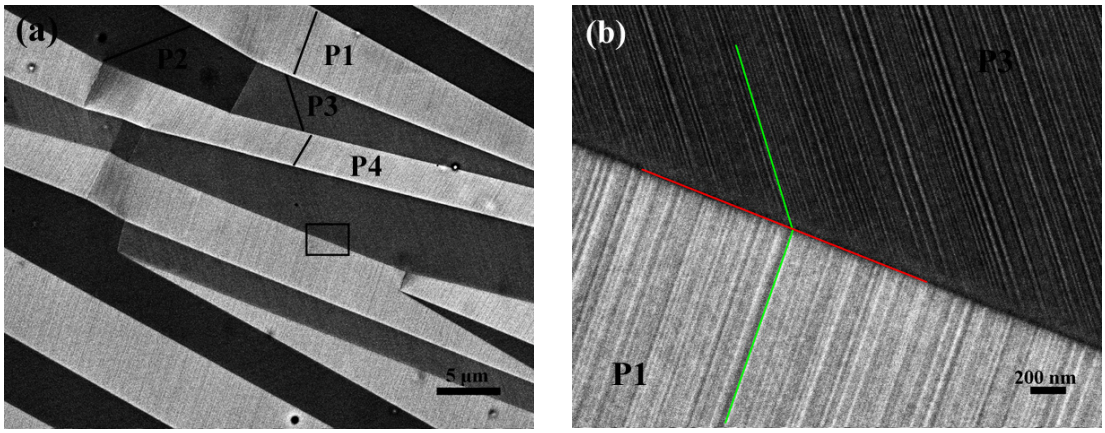

Fig.9 (a) Image en électrons rétrodiffusés obtenue dans une colonie de martensite; quatre sortes de plaques sont numérotés P1, P2, P3, P4; (b) Image agrandie de la région délimitée par le rectangle qui montre les lamelles fines appariées dans les plaques de martensite. Les interfaces inter-plaques et inter-lamellaires sont marquées avec des lignes rouge et verte, respectivement.

4. Formation de la martensite 7M auto-accommodée

L'alliage non-stoechiométrique polycristallin Ni-Mn-Ga avec composition nominale de $Ni_{53}Mn_{22}Ga_{25}$ (en % at.) a été préparé. Les mesures DSC ont montré que les températures de transformation martensitique (Ms, Mf, As, Af) étaient de 13,5 ℃, 4,9 ℃, 16,3 ℃ et 30,1 ℃, respectivement. Les diagrammes de poudre XRD de l'alliage $Ni_{53}Mn_{22}Ga_{25}$ ont été mesurées à 25 ° C, -30 ° C et -120 ° C, correspondant aux états de la coexistence d'austénite et de martensite modulée 7M, de la martensite 7M modulée seule et de la coexistence de martensite 7M et NM. Les résultats montrent que l'austénite haute température a une structure cubique ($Fm\bar{3}m$, No. 225) avec une constante de réseau a_A = 5.811 Å. La martensite 7M a été déterminée comme possédant une superstructure monoclinique à longue période (P2/m, No. 10) avec les constantes de réseau a_{7M} = 4.222 Å, b_{7M} = 5.537 Å, c_{7M} = 41.982 Å, and β = 92.5°. La martensite NM a une structure tétragonale (I4/mmm, n ° 139) avec constante de réseau $a_{Tet} = b_{Tet}$ = 3.879 Å and c_{Tet} = 6.511 Å. Il a été mis en évidence à partir des expériences de DRX que lors du refroidissement, l'austénite parente se transforme d'abord en martensite modulée 7M et ensuite la martensite modulé 7M formée se transforme en martensite NM.

La formation de microstructures caractéristique de martensite en forme de « diamant » avec quatre variantes (A, B, C et D) au cours de la transformation de l'austénite en martensite modulée 7M a été mise en évidence, comme représenté sur la Fig.10a. Comme révélé par des mesures d'EBSD, la martensite en forme de « diamant » est constituée de macles de type I (paires A:C et B:D) et de macles composées (paires A:D et B:C); la crête longue de martensite « diamant » correspond à l'interface de macles de type I et la crête courte à l'interface de macles composées. La croissance du « diamant » procède par l'allongement par le mouvement des lances vers l'avant, c.-à-d. les paires A:C ou B:D. Cet allongement entraîne la formation de macles de type II à l'arrière des lances. Ensuite, le « diamant » continue progressivement sa croissance dans les platelets appariés, comme montré dans la Fig. 10b.

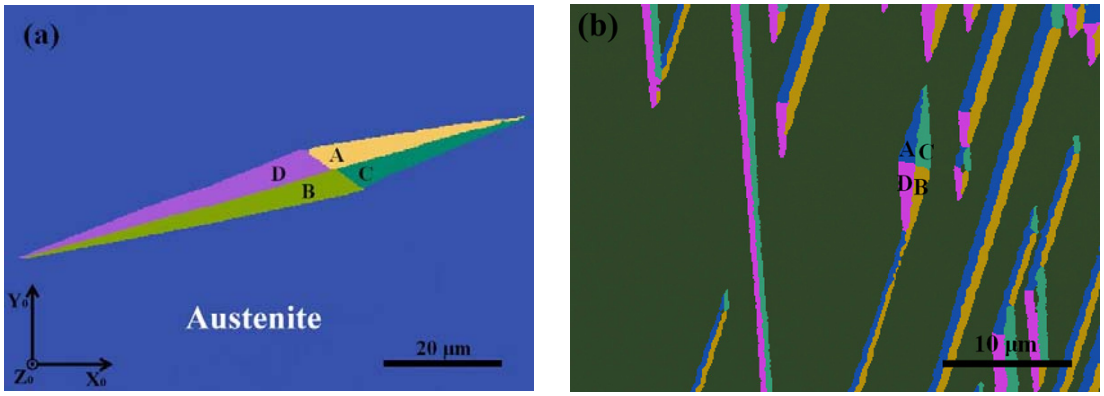

Fig.10 (a) Micrographie EBSD de martensite en forme de « diamant » composée de quatre variantes notées A, B, C et D. (b) Formation des platelets appariés à partir du « diamant ».

Les plans d'habitat ont été déterminés expérimentalement comme étant {0.736130, 0.673329, 0.068855}A au moyen de la méthode de la double trace indirecte, plans qui sont proches de {110}, avec un écart de 4,7°. Des calculs additionnels avec la théorie cristallographique phénoménologique [11] ont montré que les quatre variantes dans un groupe de type « diamant » agglomérés autour d'un pôle {101}A et que les déformations élastiques autour de la martensite se compensent effectivement mutuellement par la formation d'un tel groupe. À la fois les paires de variantes A:C (ou B:D) et A:B (ou C:D) sont auto-accommodées, tandis que les paires variantes A:D (ou B:D) paire ne le sont pas. Ainsi, la croissance du groupe de variantes n'est pas favorisée par l'extension des macles composées.

Les lances (macles de type I) devrait être responsable de la croissance de la martensite en forme de « diamant ». En comparant la déformation totale de matrice par les variantes A et C (ou B et D) avec celle par les variantes A, B, C et D, il existe encore une certaine déformation élatique résiduelle non accommodée. Cette déformation résiduelle peut être accomodée en introduisant les macles de type II, qui contribuent à la croissance de la martensite par l'intermédiaire de la progression en avant de la pointe (macles de type I). Comme la martensite en forme de « diamant » ne se compose que de macles de type I et de type composées jumeaux, les macles de type II devraient être des macles secondaire après un cisaillement supplémentaire pour la croissance de la variante. Localement, les macles de type I et de type II deux sont reliés par des macles composées et une interface de type composée est toujours apparue avec ses interfaces voisines des macles de type I et type II comme un ensemble dans la microstructure finale de la martensite.

5. Clarification de la structure et la stabilité de longue période martensite modulée

Une apparente contradiction dans l'interprétation de la structure martensitique de longue période a été soulevée récemment dans les alliages à mémoire de forme ferromagnétiques Ni-Mn-Ga. Righi et al. [4] ont fait une étude détaillée sur la martensite modulée 7M par application de l'approche du superespace à l'analyse de diffraction de rayons X (XRD) de poudres. Les résultats ont montré que la martensite modulée possède sa propre structure cristalline avec une modulation incommensurable 7M (désignée ci-après 7M (IC)). En se basant sur des mesures DRX et le concept de la phase d'adaptation [12], Kaufmann et al. [13] ont examiné la co-existence de l'austénite, de la martensite 7M et NM dans des films épitaxiaux de Ni-Mn-Ga. Ils ont conclu que la martensite 7M modulée peut être tout simplement construite à partir de variantes nanomaclées de la martensite tétragonale MN avec la séquence d'empilement $(5\,\overline{2})_2$, ce qui exclut l'existence d'un structure indépendante modulée.

En effet, il est très difficile de faire une discrimination directe de la validité de

ces deux modèles de structure. Jusqu'ici, de nombreuses études expérimentales de structures modulées ont été réalisées presque exclusivement par des techniques de diffraction. Le rôle des corrélations microstructurales entre les platelets de martensite a rarement été pris en compte soit par l'examen expérimental soit par le modèle de la combinaison de nanomacles. Ces caractéristiques microstructurales existant dans la nature ont sans doute une forte influence sur la stabilité et les fonctionnalités de la martensite modulée. Dans un tel contexte, l'alliage polycristallin massif $Ni_{53}Mn_{22}Ga_{25}$ ayant une température de transformation martensitique voisine de la température ambiante est sélectionné en tant que matériau d'essai idéal. L'alliage affiche une séquence de transformation de l'austénite à la martensite modulée puis la martensite NM au cours du refroidissement continu, détectée par des mesures de diffraction de rayons X (XRD) et des îlots de martensite modulée et martensite NM coexistent dans certains grains initiaux d'austénite, lorsqu'ils sont conservés à la température ambiante.

Le diagramme XRD de la phase modulée dans l'alliage $Ni_{53}Mn_{22}Ga_{25}$ mesuré à -30°C, comme représenté sur la fig.11a, est tout d'abord résolu puis affiné ensuite avec le modèle de structure 7M(IC) [4] en utilisant le logiciel PowderCell [14]. Il est montré que la phase modulée possède une superstructure monoclinique à longue période (P2/m, No. 10) avec les constantes de réseau a_{7M} = 4.222 Å; b_{7M} = 5.537 Å; c_{7M} = 41.982 Å, and β = 92.5°. La cellule élémentaire de la combinaison des nanomacles a également été construite artificiellement sur la base des constantes de réseau de la cellule élémentaire tétragonale NM ($a_T = b_T$ = 3.879Å, c_T = 6.511Å) et la séquence d'empilement $(5\,\bar{2})_2$ des macles $(112)_T$ [13]. Les constantes de réseau résolues pour la phase d'adaptation sont a_{ad} = 4.257 Å, b_{ad}= 5.486 Å, c_{ad} = 29.446 Å, et β_{ad} = 94.2°. Les diagrammes DRX sont recalculés en utilisant les deux modèles de structure et sont présentés dans les Fig.11b et c. On voit que les deux structures possèdent un diagramme de diffraction très proche de celui mesuré. Un examen attentif révèle que le modèle 7M(IC) fournit un ajustement au profil mesuré légèrement meilleur. La différence distinguable entre les deux structures apparaît dans les pics secondaires mineurs correspondants (marqués par une flèche dans la figure) localisés

près des trois pics de diffraction principaux dans le domaine 2 entre 40 et 50°.

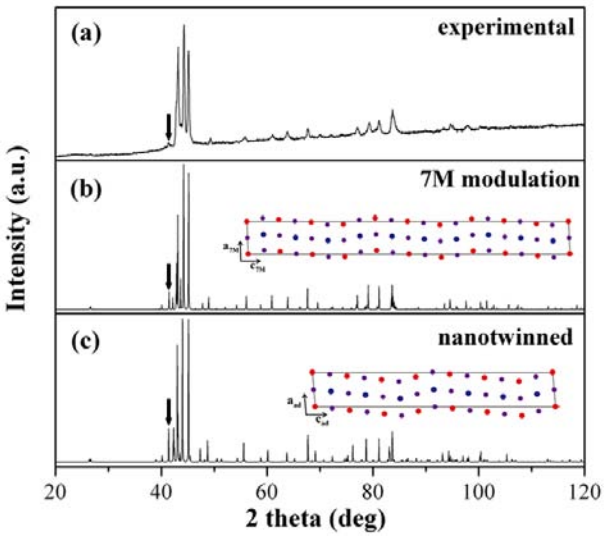

Fig.11 Diagrammes XRD pour la martensite modulée: (a) mesuré à -30 ° C; (b) recalculé avec la superstructure 7M(IC); (c) recalculé avec la cellule élémentaire tétragonale de nanomacles combinées. Les encadrés dans les figures montrent les cellules élémentaires des deux structures.

La figure 12a montre la micrographie des trois phases qui co-existent dans un grain d' austenite initiale mesurée par EBSD, où l'austenite est colorée en vert, la martensite modulée (identifiée avec la structure 7M (IC)) en bleu et la martensite NM tétragonale en gris. Les trois phases sont situées avec une contiguïté fixe, c.-à-d. austénite - martensite modulée - martensite NM, ce qui suggère que la martensite modulée est la phase intermédiaire entre l'austénite et la martensite NM. La martensite modulée et la martensite NM sont en forme de platelets et s'étendent à peu près dans la même direction. En général, les platelets de martensite modulée sont plus minces que ceux de la martensite NM. Lorsque nous approchons de la martensite NM, certains platelets modulés ont tendance à épaissir et d'autres à disparaître, ce qui indique que la transformation de la martensite modulée en martensite NM est accompagnée de la réduction de l'aire spécifique de l'interface des platelets de NM.

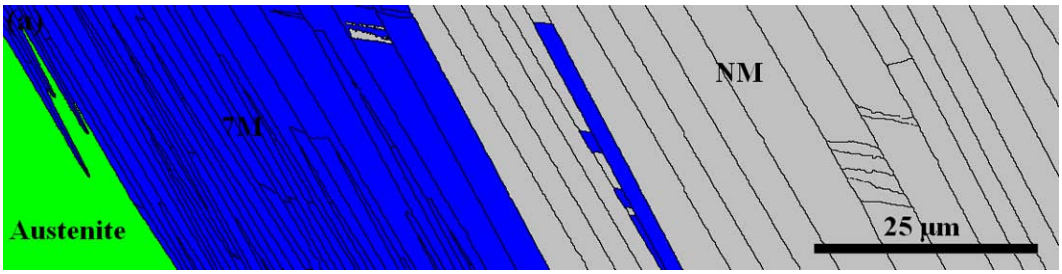

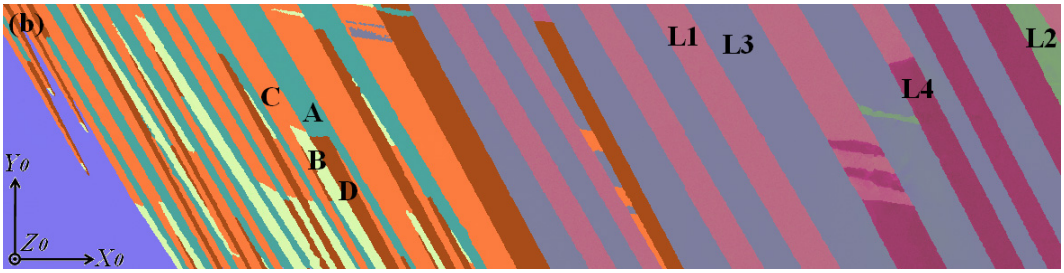

Fig.12 (a) Micrographie EBSD des phases qui montre l'austénite, la marteniste 7M (IC) et la martensite NM coexistant dans un même grain d'austénite; (b) micrographie d'orientation EBSD, où les quatre variantes de 7M sont désignées A, B, C et D et les quatre platelets de NM sont nommés P1, P2, P3 et P4. Le système de coordonnées (X0 Y0-Z0-) se réfère au système de coordonnées de l'échantillon macroscopique.

La figure 12b présente la micrographie EBSD d'orientation correspondant à la figure 12a, où les trois phases sont colorées en fonction de leurs orientations. Quatre variantes de martensite 7M A, B, C et D ont été identifiées. Dans le cadre de la structure modèle de 7M (IC), les quatre variantes sont en relation de maclage entre elles, comme dans le cas de la martensite 7M de l'alliage $Ni_{50}Mn_{30}Ga_{20}$. Les analyses en utilisant le modèle de combinaison de nano-macles donnent les mêmes résultats concernant les types de macles, mais certaines différences apparaissent dans les éléments de maclage.

Les correspondances atomiques à l'interface de macle de type I sous les deux modèles de structure sont construites et présentées dans la figure 13. Pour la structure 7M (IC) (figure 13a), l'interface des platelets est essentiellement cohérente et donc à faible énergie interfaciale. La configuration de maclage assure que s'il existe seulement deux variantes (platelets) dans le matériau, une variante peut être facilement réorientée dans l'orientation de l'autre par maclage ou démaclage par le mouvement de l'interface des platelets. En revanche, si la martensite modulée a une structure de combinaison de nano-macles en séquence $(5\,\bar{2})_2$, les caractéristiques au niveau de l'interface enter les platelets et de la structure à l'intérieur du platelet sont très différentes. Comme le montre la figure 13b, les deux platelets d'orientation correspondent à quatre variantes d'orientation de la martensite tétragonale NM qui sont en forme lamellaire. Les variantes à l'intérieur du platelet sont liées par relation de macle. À l'interface du platelet, la cohérence atomique est fortement dégradée par

le fait que deux lamelles épaisses et deux lamelles minces à partir des platelets voisins se croisent à l'interface, comme illustré dans la figure 13b. Lorsque les lamelles épaisses se rencontrent, elles semblent être en relation de macle $(1\,\bar{1}\,2)_T[\,\bar{1}\,11]_T$ mais avec quelques degrés de déviation du plan de maclage et de la direction de maclage, c'est à dire 4,97 ° entre les plans $(1\bar{1}2)_T$ et 2,62 ° entre les directions $[\bar{1}11]_T$. En utilisant les deux plans $(1\bar{1}2)_T$ en tant que référence, les plans des lamelles minces les plus proches à partir des platelets voisins sont $(010)_T$. L'écart angulaire entre les deux plans est 11,44 °. Ainsi, le parallélisme des plans est loin d'être parfait.

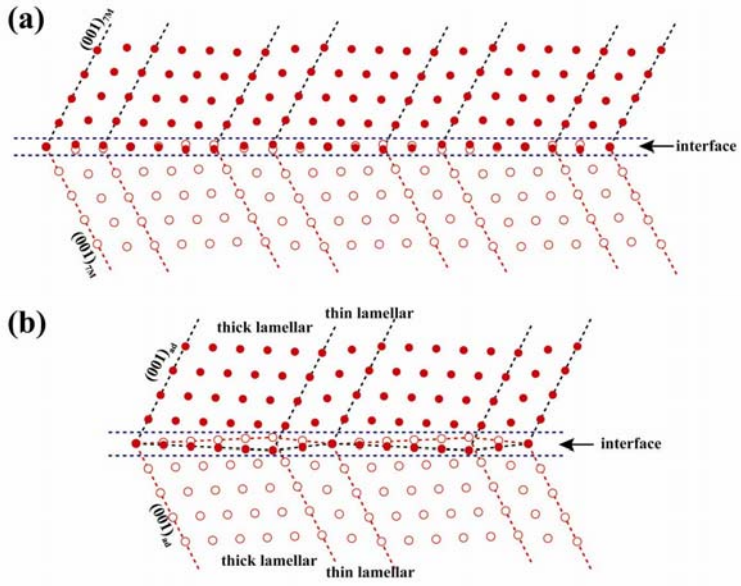

Fig. 13 Correspondance atomique à l'interface de macle de type I de la martensite modulée vue le long de la direction $[210]_{7M}$ construite sous l'hypothèse (a) du modèle de la structure 7M(IC) et (b) du modèle de la structure de combinaison de nano-macles. Pour une représentation claire, uniquement les atomes de Mn sont dessinés.

Le déplacement atomique moyen des atomes ($\bar{r}$) sur l'interface entre les platelets par rapport à leurs positions d'équilibre sous l'hypothèse des deux modèles de structure a été calculé. Les résultats montrent que le déplacement moyen est de 1,52% pour la structure 7M (IC) et 3,81% pour la structure de combinaison de nano-macles. Il est clair que l'écart des atomes à l'interface du platelet sous la combinaison de nano-macles est beaucoup plus élevé que celui sous 7M (IC). En conséquence, on peut s'attendre à une haute énergie de l'interface de platelet résultant du déplacement atomique pour le modèle de la combinaison de nano-macles. L'épaississement des

platelets de NM pour réduire l'interface spécifique prouve indirectement que l'interface des platelets de la martensite de nano-macles combinées doit posséder une haute énergie interfaciale. En outre, le décalage important sur les interfaces du platelet et la configuration de macles dans le platelet du modèle de la combinaison de nano-macles sûrement impose des contraintes importantes sur la réorientation de variantes.

L'écart de la maille des deux modèles de structure par rapport à celle de l'austénite cubique ont été calculées et exprimées en tenseurs de déformations sans contraintes (ε_{11}, ε_{22}, ε_{33}, γ) [9]. Les termes non nuls de ces tenseurs sont indiqués dans le tableau 5. Il est évident que la combinaison de nano-macles a un décalage de maille supérieur à celui de la structure modulée 7M(IC). Tous les résultats ci-dessus ont montré que la martensite modulée dans l'alliage Ni-Mn-Ga a son propre structure cristalline, autre que la combinaison de nano-macles de la martensite NM tétragonale.

Tableau 5 Tenseurs de déformations entre la matrice et les phases produites pour la transformation de l'austénite en 7M et de l'austénite en phase adaptive (structure de combinaison de nano-macles).

	Austenite -7M modulation	Austenite - nanotwin combination
ε_{11}	0.0275	0.0360
ε_{22}	-0.0472	-0.0559
ε_{33}	0.0207	0.0210
γ	-0.0446	-0.0750

6. Rôle de la martensite 7M dans la transformation de l'austénite en martensite NM

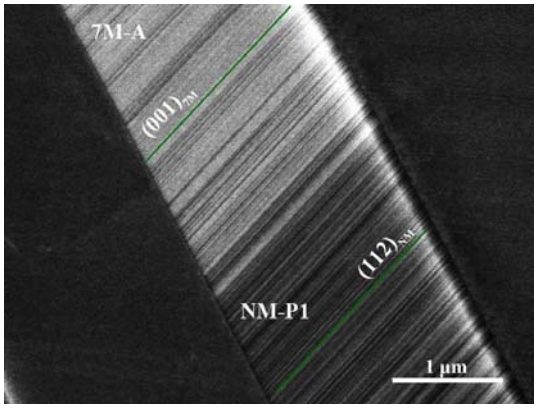

Fig. 14 Image en électrons rétrodiffusés (BSE) montrant la transition de la variante A de 7M au

platelet P1 de NM.

La relation d'orientation entre les martensites 7M et NM a été déterminée. Les calculs montrent que la martensite 7M et la martensite NM possèdent une relation d'orientation spécifique avec $(001)_{7M}//(112)_T$ et $[100]_{7M}//[11\bar{1}]_T$, *i.e.* le plan de réarrangement dans une variante 7M est parallèle au plan de maclage des lamelles NM correspondant et la direction de cisaillement est parallèle à la direction de maclage. La relation d'orientation assure une correspondance univoque entre les platelet de 7M et ceux de NM, tel que cela apparaît dans la figure 14, où les martensites 7M et NM coexistent dans le même platelet. Dans la figure, la martensite 7M et la martensite NM affichent clairement des contrastes différents en raison de leurs structures cristallines différentes. Dans le platelet, les traces des plans de réarrangement de 7M sont parallèles à ceux de maclage de NM.

La relation d'orientation intrinsèque entre les martensites 7M et NM avec $(001)_{7M}//(112)_{NM}$ et $[100]_{7M}//[11\bar{1}]_{NM}$ indique que la transformation de la structure 7M (monoclinique) en NM (tétragonale) peut être considérée comme un réarrangement additionnel des atomes sur le plan $(001)_{7M}$ le long de la direction $[100]_{7M}$ ou la direction $[\bar{1}00]_{7M}$ avec certaines distorsions de ces plans et de leurs distances interplanaires.

La figure 15 présente les correspondances atomiques à l'interface entre variante A et C (macle de type I) de la martensite 7M et l'interface entre les platelets P1 et P3 de la martensite NM suite à la relation d'orientation de la transformation. On voit que, bien que quelques uns des atomes à l'interface sont légèrement déviés de leur position exacte d'équilibre en raison de la modulation de la structure, l'interface du platelet de 7M est fondamentalement cohérente. Toutefois, lorsque les platelets de 7M se transforment en NM, les écarts des atomes à l'interface deviennent non négligeables, comme indiqué dans la figure 15b. L'interface de platelet devient ainsi non-cohérente. Cet écart atomique sans doute élève l'énergie interfaciale et contribue ainsi comme un obstacle énergétique à la transformation. Du à cet écart atomique élevé, la

transformation de 7M en NM est accompagnée par l'épaississement des platelets de martensite NM, ce qui peut réduire l'aire interfaciale spécifique de la martensite NM et donc réduire l'énergie totale interfaciale de platelets NM.

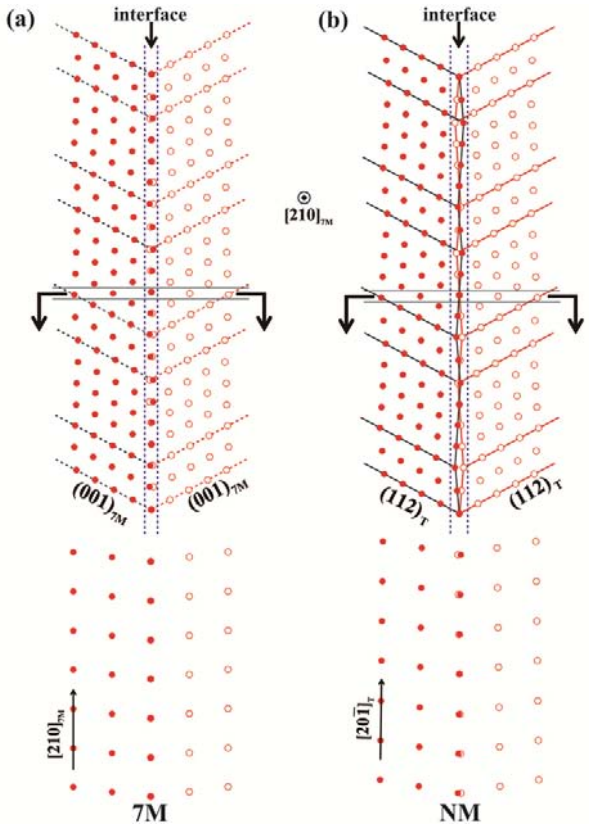

Fig. 15 (a) La projection de l'interface atomique de macle de type I dans la direction $[210]_{7M}$ et les correspondances atomiques dans la section transversale pour la martensite 7M ; (b) l'interface correspondante entre les platelets de martensite NM et les correspondances atomiques dans la section transversale.

Cette distorsion du réseau pour la transformation de l'austénite en martensite 7M et de l'austénite directement en martensite NM a été quantifiée par les tenseurs de déformation sans contrainte [12], comme indiqué dans le tableau 6. De toute évidence, la distorsion du réseau de l'austénite cubique à la martensite tétragonale est beaucoup plus grande que celle qui se produit dans la transformation de l'austénite à la martensite 7M. Avec la grande énergie interfaciale de platelet, l'énergie élastique dépendante du volume générée par la distorsion du réseau impose des obstacles insurmontables à la transformation de l'austénite en martensite NM. Par conséquent, la formation de la phase intermédiaire modulée 7M est inévitable pour établir le pont entre l'austénite parent et la martensite NM finale et donc une distorsion du réseau en

deux étapes est subie dans la transformation de l'austénite en martensite NM. Au cours de cette transformation en deux étapes, une variante d'austénite donnera lieu à 4 variantes d'orientation de 7M en relation de macle et une variante de 7M formera 2 variantes de NM qui sont en relation de macle, de manière correspondante 8 variantes d'orientation de NM au total sont obtenues.

Tableau 6 Tenseurs de déformation entre la matrice et les phases produites pour la transformation de l'austénite en 7M, de l'austénite en NM et de 7M en NM.

	Austenite - 7M	Austenite - NM	7M-NM
ε_{11}	0.0275	-0.0560	0.0083
ε_{22}	-0.0472	0.1204	-0.0092
ε_{33}	0.0207	-0.0560	0.0002
γ	-0.0446	0	0.0093

Conclusions

(1) L'alliage $Ni_{50}Mn_{28}Ga_{22}$

La martensite possède une superstructure monoclinique 5M modulée à la température ambiante. Le super-réseau est composé de 5 sous-cellules. La microstructure de la martensite 5M peut être caractérisée par des platelets larges avec des variantes fines distribuées alternativement. Des mesures EBSD en utilisant les informations de la superstructure monoclinique ont révélé quatre variantes A, B, C et D qui sont en relations de macle l'une par rapport à l'autre avec des orientations distinctes dans une platelet large, c'est à dire la paire de variantes A: C (ou B: D) est en relation de macle de type I, A: B (ou C: D) de macle de type II et A: D (ou B et C) de macle composée. Les interfaces des variantes se sont révélées être les plans de maclage (K1) correspondants. En se basant sur des orientations locales des variantes individuelles de la martensite mesurées par EBSD et des calculs cristallographiques, la relation d'orientation de la transformation de l'austénite en martensite 5M la plus favorable a été révélée être la relation de Pitsch avec $(101)_A//(1\ \bar{2}\ \bar{5})_{5M}$ et $[10\ \bar{1}]_A//[\bar{5}\ \bar{5}\ 1]_{5M}$ sans recours à l'austénite résiduelle.

(2) L'alligae $Ni_{50}Mn_{30}Ga_{20}$:

Il est confirmé par l'indexation de clichés de Kikuchi que la martensite 7M possède une superstructure incommensurable monoclinique et le super-réseau est composé de dix sous-cellules. Dans un grain d'austénite parente, une ou plusieurs colonies de martensite se forment, chacune constituée de 4 variantes (A, B, C et D) qui sont en relation de macle l'une par rapport à l'autre. Toutes les paires de variantes peuvent être classées en trois modes de macle: les variantes A et C (ou B et D) forment des macles de type I, les variantes A et B (ou C et D) des macles de type II, et les variantes A et D (ou B et C) des macles composées. Toutes les interfaces sont en coïncidence avec le plan respectif de maclage (K1). En outre, en se basant sur les orientations locales des différents variantes martensitiques mesurées par EBSD et sur les analyses cristallographiques détaillées, la relation d'orientation la plus favorable énergétiquement régissant la transformation de l'austénite en martensite 7M incommensurable a été identifiée être la relation de Pitsch avec $(1\ 0\ 1)_A//(1\ \bar{2}\ \overline{10})_{7M}$ et $[1\ 0\ \bar{1}]_A//[\overline{10}\ \overline{10}\ 1]_{7M}$. Notamment, l'ambiguïté de la relation d'orientation géométriquement la plus favorable a été résolue par l'examen de la discontinuité du réseau causée par la transformation de phase et par la modulation structurale.

(3) L'alliage $Ni_{54}Mn_{24}Ga_{22}$:

L'alliage se compose de platelets de martensite NM auto-accomodés ayant une structure cristalline tétragonale. Les platelets adjacents ont la relation de désorientation 80° ~ 85° autour des axes $<110>_T$. Localement, quatre types de platelets sont identifiés et chaque platelet se compose de paires de variantes fines. Totalement, huit variantes d'orientation se trouvent dans une colonie de martensite. Les variantes fines en paires dans chaque platelet ont été trouvées en relation de macle composée avec le plan $\{112\}_T$ comme plan de maclage et la direction $<11\bar{1}>_T$ comme direction de maclage. Les interfaces inter-platelets sont proches du plan $\{112\}_T$, mais avec ~ 3 ° d'écart, tandis que les interfaces de deux paires de variantes fines sont en bon accord avec le plan de maclage $\{112\}_T$.

(4) L'alliage $Ni_{53}Mn_{22}Ga_{25}$:

A température ambiante, l'austénite et la martensite co-existent dans l'alliage $Ni_{53}Mn_{22}Ga_{25}$. La formation de microstructures caractéristiques de martensite en forme de « diamant » avec quatre variantes (A, B, C et D) au cours de la transformation de l'austénite en martensite modulée 7M a été mise en évidence. Comme révélé par des mesures EBSD, le « diamant » est constitué des variantes de martensite en relation de macle de type I (A: C et B: D) et de macles composées (A: D et B: C); la longue crête du « diamant » correspond à l'interface de macle de type I et la courte crête à l'interface de macle composée. Les diamants se transforment finalement en platelets de martensite. Des calculs cristallographiques montrent que les quatre variantes caractéristiques dans un groupe de diamant sont autour d'un plan $\{101\}_A$ et les déformations élastiques issues de la transformation ont été effectivement annulées par la formation du groupement. Les paires de variantes A: C (ou B: D) et A: B (ou C: D) sont toutes les deux auto-accommodées, tandis que les paires A: D (ou B: D) ne le sont pas.

La microstructure avec les trois phases (austénite, martensite modulé et martensite NM final) co-existantes a été observée dans certains grains d'austénite. Les trois phases sont situées avec une contiguïté fixe, c.-à-d. austénite - martensite modulé - martensite NM. La martensite 7M de période longue se produit lors du refroidissement en tant qu'une phase thermodynamiquement métastable qui est intermédiaire entre l'austénite parente et la martensite NM finale stable. La phase martensite modulée possède une structure cristalline indépendante, plutôt que la combinaison de nano-macles de martensite normale non-modulée comme proposée par la théorie de combinaison de nano-macles. La structure modulée de la martensite 7M offre un nombre de variantes locales réduit et la configuration favorable pour maclage et démaclage. Cela est essentiel pour réaliser le changement de forme induit par un champ magnétique.

Le rôle de la martensite 7M dans la transformation de l'austénite cubique en martensite tétragonale NM a été clarifié. Dans cette transformation, le désaccord de maille entre l'austénite cubique et la martensite NM tétragonale et la formation des interfaces inter-platelet NM incohérentes représentent une barrière d'énergie insurmontable pour une transformation directe de l'austénite en martensite NM. La

formation de martensite modulée 7M est mise en évidence comme une étape intermédiaire en introduisant une structure cristalline qui atténue grandement le désaccord large entre les mailles et en formant les interfaces inter-platelets cohérentes. Au cours de cette transformation en deux étapes, une variante de l'austénite donnera lieu à 4 variantes de martensite 7M qui sont en relation de macle l'une par rapport à l'autre. Une variante 7M se transforme en 2 variantes NM, de manière correspondante 8 variantes d'orientation de NM au total sont obtenues. La transformation de 7M en martensite NM est réalisée par une déformation du réseau suivant la relation d'orientation $(001)_{7M}$ // $(112)_T$ et $[100]_{7M}$ // $[11\bar{1}]_T$, qui est accompagnée par la dégradation de la cohérence des atomes au voisinage de l'interface des platelets NM et par le changement complet de la configuration de maclage.

Références

[1] A. Sozinov, A.A. Likhachev, N. Lanska, K. Ullakko, Applied Physics Letters, 80 (2002) 1746-1748.

[2] P. Müllner, V.A. Chernenko, G. Kostorz, Journal of Applied Physics, 95 (2004) 1531-1536.

[3] I. Glavatskyy, N. Glavatska, I. Urubkov, J.U. Hoffman, F. Bourdarot, Materials Science and Engineering: A, 481-482 (2008) 298-301.

[4] L. Righi, F. Albertini, E. Villa, A. Paoluzi, G. Calestani, V. Chernenko, S. Besseghini, C. Ritter, F. Passaretti, Acta Materialia, 56 (2008) 4529-4535.

[5] P.J. Brown, J. Crangle, T. Kanomata, M. Matsmuoto, K.U. Neumann, B. Ouladdiaf, K.R.A. Ziebeck, Journal of Physics: Condensed Matter, 14 (2002) 10159-10171.

[6] D.Y. Cong, Y.D. Wang, P. Zetterstrom, R.L. Peng, R. Delaplane, X. Zhao, L. Zuo, Materials Science and Technology, 21 (2005) 1412-1416.

[7] Y.D. Zhang, C. Esling, X. Zhao, L. Zuo, Journal of Applied Crystallography, 40 (2007) 436-440.

[8] M. Humbert, F. Wagner, H. Moustahfid, C. Esling, Journal of Applied Crystallography, 28 (1995) 571-576.

[9] Y. Zhang, Z. Li, C. Esling, J. Muller, X. Zhao, L. Zuo, Journal of Applied Crystallography, 43 (2010) 1426-1430.

[10] D.Y. Cong, P. Zetterstrom, Y.D. Wang, R. Delaplane, R.L. Peng, X. Zhao, L. Zuo, Applied Physics Letters, 87 (2005).

[11] M.S. Wechsler, D.S. Lieberman, T.A. Read, Transactions of the American Institute of Mining and Metallurgical Engineers, 197 (1953) 1503-1515.

[12] A.G. Khachaturyan, S.M. Shapiro, S. Semenovskaya, Physical Review B, 43 (1991) 10832.

[13] S. Kaufmann, U.K. Rößler, O. Heczko, M. Wuttig, J. Buschbeck, L. Schultz, S. Fähler, Physical Review Letters, 104 (2010) 145702.

[14] W. Kraus, G. Nolze, Journal of Applied Crystallography, 29 (1996) 301-303.